ABSTRACT

Title of Dissertation:	ELECTRICAL AND STRUCTURAL FORMATION OF TRANSIENT LIQUID PHASE SINTER (TLPS) MATERIALS DURING EARLY PROCESSING STAGE
	Gilad Nave, Doctor of Philosophy, 2023
Dissertation directed by:	Professor Patrick McCluskey, Department of Mechanical Engineering

The growing demands of electrification are driving research into new electronic materials. These electronic materials must have high electrical conductivity, withstand harsh environments and high temperatures and demonstrate reliable solutions as part of complete electronic packaging solutions. This dissertation focuses on characterizing the initial stage of the manufacturing process of Transient Liquid Phase Sinter (TLPS) alloys in a paste form as candidates for Pb-free high-temperature and high-power electronic materials.

The main objective of this dissertation work is to investigate the factors and decouple the multiple cross effects occurring during the first stage of TLPS processing in order to improve the understanding of material evolution. The work proposes, develops, and conducts in-situ electrical resistivity tests to directly measure material properties and analyze the dynamics at different stages of the material's evolution. The research explores various factors, including alloying elements, organic binders, and heating rates, to understand their effects on the development of electrical performance in electronic materials. More specifically, the work examines the performance of Ag-

In, Ag-Sn and Cu-Sn TLPS paste systems. Additionally, packing density and changes in cross-section are investigated using imaging techniques and image processing to gain insights into the early formation of the material's structural backbone. An Arrhenius relationship together with Linear Mixed Models (LMM) techniques are used to extract the activation energies involved with each of the processing stages. The study then develops procedures to model different states of the TLPS microstructures at different heating stages based on experimentally observed data. Using these models, the study uses Finite Element Method (FEM) analysis to verify the experimental results and gain a better understanding and visualization into the involved mechanisms. This investigation not only sheds light on the material's behavior but also has implications for robust additive manufacturing (AM) applications.

ELECTRICAL AND STRUCTURAL FORMATION OF TRANSIENT LIQUID PHASE SINTER (TLPS) MATERIALS DURING EARLY PROCESSING STAGE

by

Gilad Nave

Dissertation submitted to the Faculty of the Graduate School of the
University of Maryland, College Park, in partial fulfillment
of the requirements for the degree of
Doctor of Philosophy
2023

Advisory Committee:
Professor Patrick McCluskey, Chair
Professor Hugh Bruck
Professor Abhijit Dasgupta
Professor Peter Sandborn
Professor Mohamad Al-Sheikhly
Dr. Diganta Das

Dedication

To my parents Yuval and Tsafnat for their unconditional love and endless support, the countless hours of phone calls that helped me navigate through this emotional, physical, and mental challenge, and the other countless forms of help that I always appreciate and cherish.

To my love and dearest person in my life, Musirah. This journey could not be the same without you beside me. You made sure that I would be the best version of myself. I am thankful that even though sometimes you were mad at me for working probably too hard and too long, you always believed in and supported me.

To my Grandma Rina, who supported me from day one. You have a huge part in my ability to complete this journey.

To my friends: Dvir, Or, Assaf, Kang, Dani, and Natalie for always believing in me and encouraging me to be myself.

To my sister and her husband, Noa and Yonatan, and, most importantly, their son Tom, who made sure that I smiled through the last year of the Ph.D.

Acknowledgements

Firstly, I would like to acknowledge my advisor through this journey, Professor Patrick McCluskey, who sparked my curiosity towards material science, hired me for my first research position, and guided me through the Ph.D. process. I would especially also like to thank Professor Abhijit Dasgupta, who influenced and educated me the most while I was taking all his available undergraduate and graduate-level courses. I also like to acknowledge the rest of my dissertation and proposal committee for their comments and support of my research: Prof. Hugh Bruck, Prof. Peter Sandborn, Prof. Mark Fuge, Prof. Mohamad Al-Sheikhly, and Dr. Diganta Das.

From my coworkers, I would like to acknowledge Zhaoxi for his endless support and his horrific, yet unique and priceless, sense of humor. I want to thank Ibaad for his ever-desire to learn and help. I would like to thank Sriram, who taught me how to use the SEM at midnight over the phone; I will never forget it. I would also like to thank Kunal, Subramani, Aniket, Namkyoung, and Elizabeth for their support, friendship, and advice.

Special thanks to people who were like mentors to me during this journey: Dr. Bob, who always had time for my endless questions in the laboratory. Majid and David, the machine shop owners, who helped me in the development process and always provided supportive and helpful advice. I would also like to thank Mark and Steve from SLB, who elevated my engineering and research to another level and always showed curiosity in my work and effort.

Table of Contents

List of Tables

List of Figures

1 INTRODUCTION AND MOTIVATION

The electrification of various industries has become imperative due to the rising demand, stricter regulations, and global focus on renewable energy and decarbonization solutions [1]. Simultaneously, the classical perspective of Moore's Law based on geometrical scaling is nearing its limits in the field of electronics [2]. Figure 1-1 illustrates the progression towards the limit of Moore's Law, with Si-based transistors reaching a feature size of 3nm, which is approximately equivalent to the size of ten atoms. At such small feature sizes, physical constraints like quantum effects come into play [3]. Moreover, as shown in Figure 1-2, the cost associated with reducing the size of transistors is exponentially increasing. In order to address these challenges and enable further advancements, innovative approaches are being actively investigated.

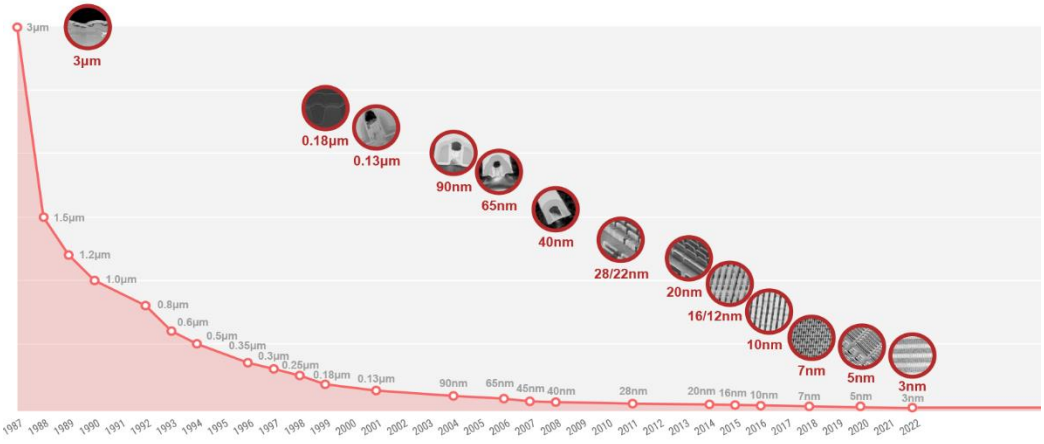

Figure 1-1: shows the decrease in the size of transistors over the years 1987 to 2022. The size of the transistors has decreased from single digit micrometers in the early nineties, to single digit nanometers in the recent years [4].

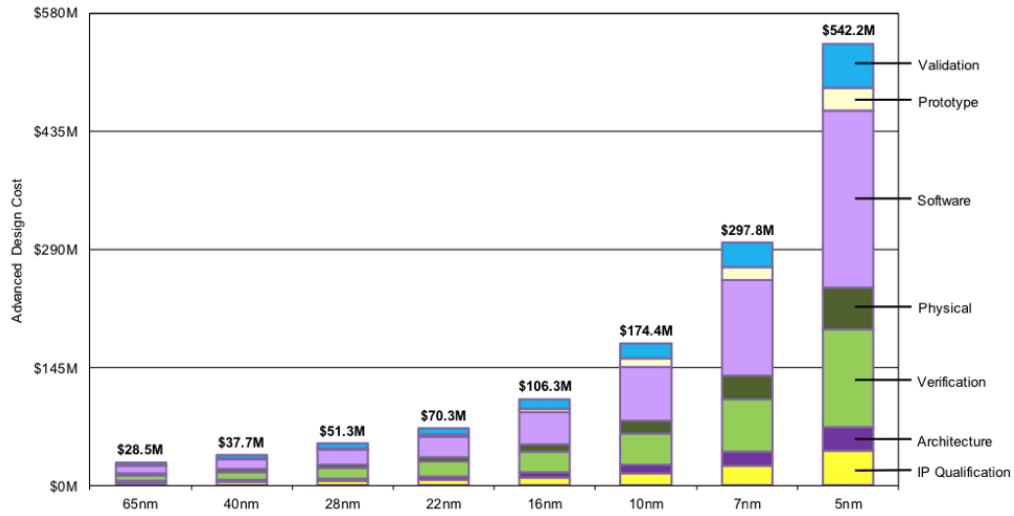

Figure 1-2: Design costs breakdown vs. transistor's size [5].

These approaches include the identification of new physical state variables to enhance information processing and computational performance [6], the investigation of alternative computing architectures and software optimization [7], the development of innovative algorithms [8], the implementation of advanced and high-precision manufacturing methods [9], and the exploration, development, and integration of new materials [10,11]. Wide Band Gap (WBG) semiconductors such as GaN and SiC show promising potential for the continuous evolution of the electronics industry, particularly in the domains of power electronics and harsh environment applications [12]. WBG semiconductors offer numerous advantages over Si-based semiconductors. These advantages include higher operating voltages and frequencies, elevated operating temperatures, increased blocking voltages, reduced parasitic resistances, and enhanced power density capabilities [13]. Figure 1-3 provides a

graphical representation that compares the performance of Si-based semiconductors with that of WBG semiconductors.

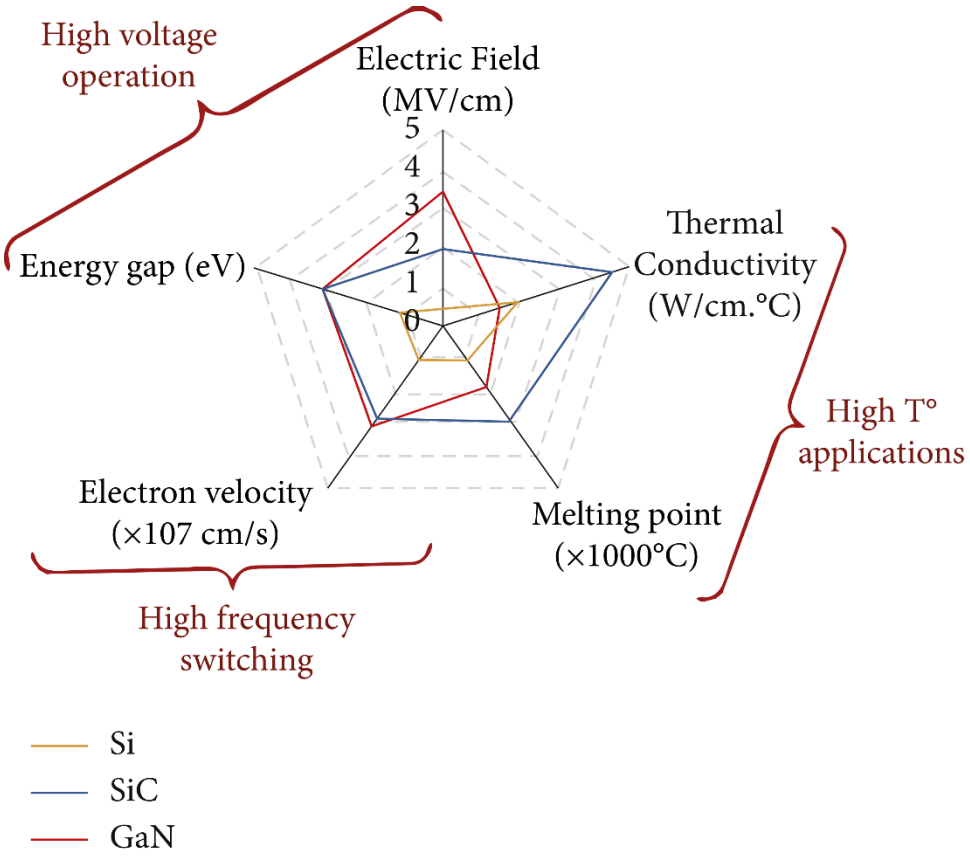

Figure 1-3: Comparison between Si, SiC, and GaN semiconductors in key performance characteristics [14].

As shown in Figure 1-3, SiC and GaN exhibit significant performance advantages over Si-based semiconductors in various aspects. SiC-based semiconductors possess improved thermal conductivity, resulting in reduced cooling requirements for high-power density applications. Furthermore, the higher melting points of WBG materials, compared to Si-based semiconductors, enhance the overall reliability of systems operating at high temperatures and power densities. The WBG

semiconductors' high saturation electron velocity is advantageous for high switching applications. In combination with higher breakdown voltages, lower on-resistance, and reduced leakage currents, WBG semiconductors vastly outperform conventional Si-based semiconductors [15]. For metal oxide semiconductor field effect transistor (MOSFET), the on-resistance losses depend on the relative permeability ε_r and the breakdown electrical field E_c, and increasing E_c as shown in Figure 1-3 translates to lower on-resistance as shown in eq. **1.1**:

$$r_{on} \propto \frac{1}{\varepsilon_r E_c} \tag{1.1}$$

Unlike microelectronics and regular electronics which are designed to carry information and commands through digital signals, power electronics are designed to convert, transfer, and manipulate electrical power. In the United States for example, the integration of WBG into the power electronics industry has the potential to significantly reduce CO_2 emissions with estimates of up to 65.3 million-tons by 2025 [16]. In general, the best applications for SiC and GaN today are applications that require weight reduction, fast response times, high robustness, high temperature, and high magnetic field [17]. Some power electronics applications that are increasingly adopting the use of WBG are:

- **Photovoltaics:** WBG circuits enable operations at higher voltages, simplifying the circuits, enabling DC systems with fewer DC/DC converters, and potentially eliminating the need for on-site AC transmission lines [18].

- **Wind Energy:** figure 1-4 shows a common use of power electronics convertors in wind turbine circuit design as a way of providing better control of variable output of the wind turbine. Implementing WBG semiconductors in these regulation devices can help reduce their size, increase their reliability, and improve the overall performance [19].
- **Power Distribution:** power distribution in smart grids together with WBG semiconductors improve the efficiency, reliability, and performance of the ever-growing electrical demands of urbanization. The implementation of WBG semiconductors in smart grids and power distribution improves grid stabilization during peak demands and due to irregular fluctuations of renewable energy sources. In addition, the implementation of WBG semiconductors in smart grids and power distribution solutions contributes to higher grid efficiency, and energy saving can be achieved due to more efficient power conversions and reduced power losses [20].

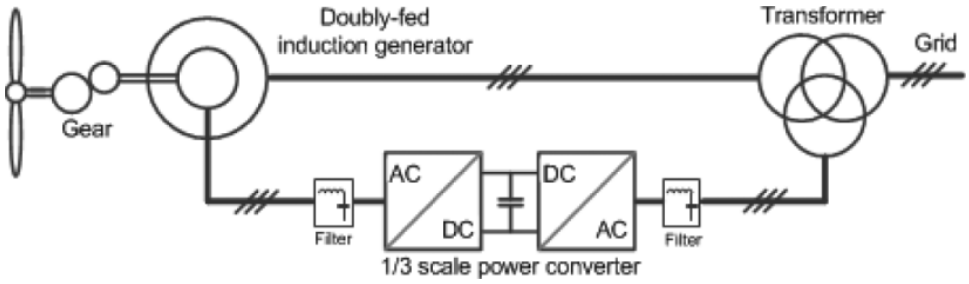

Figure 1-4: Variable-speed wind turbine with partial-scale power converter and Double-fed induction generator [19]**.**

- **Electric and hybrid automotive:** electric and hybrid automotive applications can benefit from WBG semiconductors implementation in multiple systems such as the motor drive, onboard convertors, and charges. The improvement is manifested by potential improvement of systems size which is linked to reduce volume and mass to up 46%, 76%, and 53% for the motor drive, onboard converters, and chargers respectively. For the same systems, the improvement in power densities in kW/Liter increase by hundreds of percent [21].
- **Electric and hybrid aircrafts:** in the context of aircraft, particularly during the takeoff phase as shown in Figure 1-5, extreme mission profiles necessitate enhanced power and efficiency characteristics, as well as reduced weight and size of electronic systems. WBG semiconductors have emerged as crucial components for achieving these objectives. The implementation of WBG semiconductors in aircraft electronics facilitates the transition towards electric and hybrid aircraft, owing to their improved power capabilities, higher efficiency, and compact form factor [22,23].
- **Uninterrupted power supplies (UPSs) and Data Centers:** UPS systems are essential for modern high-power regulation and use of batteries. The use of batteries that are connected to the grid require power conversion solutions with minimal losses. SiC-MOSFET offer solutions with efficiency levels of up to 98% and improved power densities for UPS applications [24]. The use of UPS is common in data center applications, as well as in multiple voltage converters.

With 13% of the world's total electricity demand by 2030, the improved efficiency and performance in data centers is highly important [25].

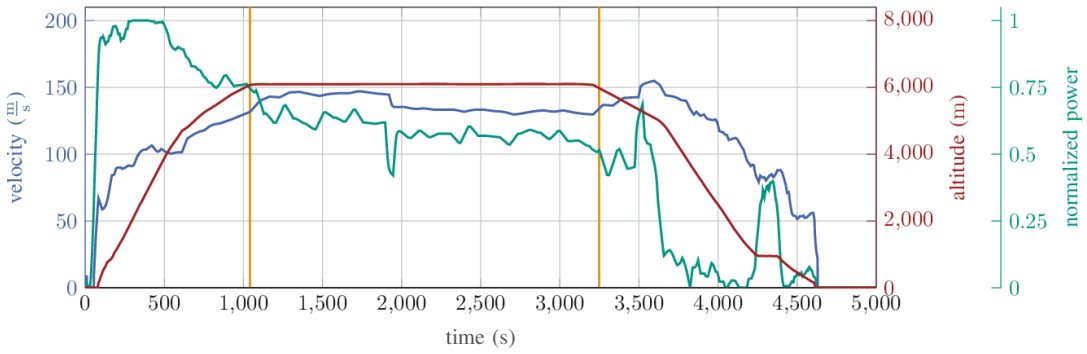

Figure 1-5: Common mission profile of aircraft. Majority of power demand is during the lift-off operation [26]**.**

- **Consumer electronics:** consumer electronics can greatly benefit from the implementation of WBG semiconductors with advantages such as faster charging rates, better performance for high computing applications, and higher power for LED lighting applications [27].

Figure 1-6 shows some of the applications discussed above that benefit and require the increased demand for power electronics.

1.1 Challenges in Integrating WBG Semiconductors Materials and Reliability Concerns

Despite the apparent advantages of WBG semiconductor materials, the comprehensive integration of these materials presents significant challenges. These challenges encompass the need to enhance standardization, promoting collaborations

among diverse research and development disciplines [28], and address the demand for advanced interconnect materials [29]. Moreover, successful implementation of WBG semiconductor materials requires interconnect and attach materials capable of withstanding extreme conditions. These conditions include temperatures surpassing 300 °C, severe mechanical and vibrational stresses, as well as corrosive and humid environments [23,30–32].

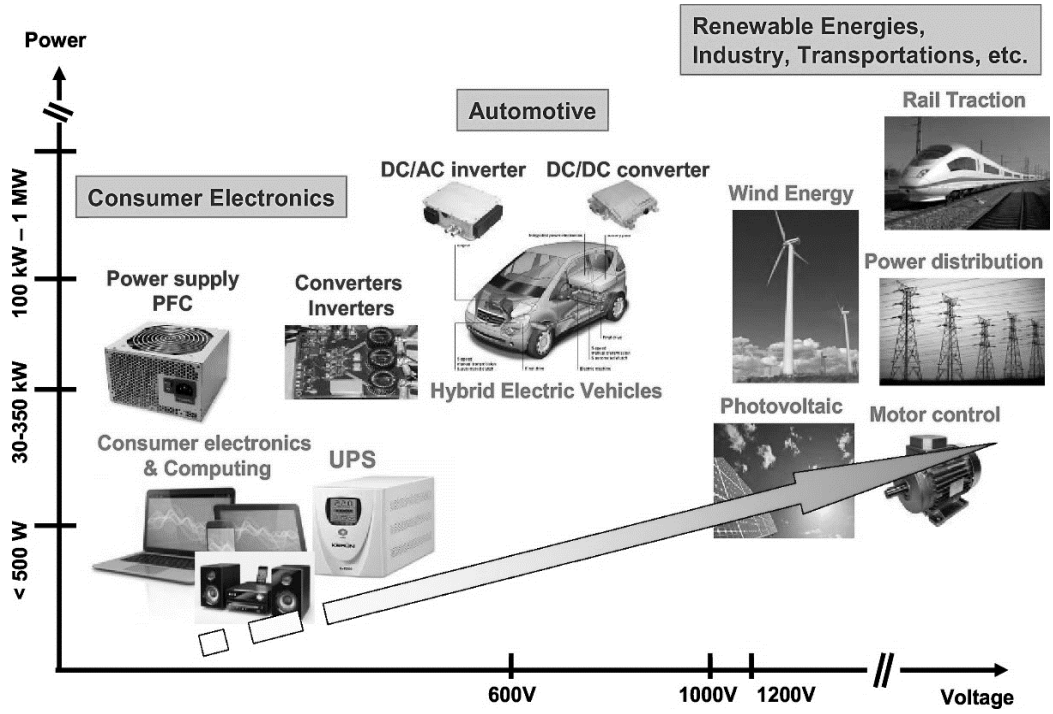

Figure 1-6: Different applications for power electronics, and their respective voltage and power demands [33].

Additionally, these materials must adhere to stringent thermomechanical and chemical requirements while avoiding the use of Pb-based products, aligning with the growing environmental consciousness and updated regulations such as the Restriction of Hazardous Substances (RoHS) directive [34].

As mention above, the natural size limit and growing costs to decrease the transistors' size, push the industry to find new solutions to keep the demand of more powerful and fast electronics. Among these solutions, the industry is looking to transition from 2D Integrated Circuit (IC) architectures, to 3D IC and general circuit architectures. The transition to 3D electronics requires the ability to pack multiple chips on top of each other. These chips must be able to communicate between themselves and with the rest of the electronic circuit. The vertical connections that connect these stacked chips and other electronic components, are responsible for mechanical support, electrical current paths, and heat exchange [35]. These currents are responsible for the joule heating effect. The effect grows with a squared factor of the electrical current as shown in eq. **1.2**:

$$P = I^2 R \qquad 1.2$$

Where P is power in joules per second, I is the electrical applied current in amperes, and R is the resistance to current flow in ohms. For most conducting materials, the rise of temperature due to the joule heating effect, will inevitably cause a parasitic effect of increased resistivity of the conductor material. The resistivity of the conductor, ρ, is an intrinsic property of the conductor material which linearly increases in proportion to the increased temperature. The need to dissipate large amounts of power and heat, and the reduced size of the electronics, leads to situations where solder bumps can experience temperature gradients of 1000°C/cm [36]. These extremely high temperature gradients are enough to generate significant thermomigration effect across

the solder joints and interconnects to pose a reliability concern to the industry. The joule heating effect is also responsible for several other reliability concerns such as accelerated formation of brittle Intermetallic Compounds (IMC), acceleration of the electromigration effect, and stress gradients across the solder joints.

1.2 High-Temperature Pb-free Electronic Interconnects Materials

The transition from Pb-based solder to Pb-free solders poses an ongoing challenge in applications requiring high operating temperatures. Concerns about the reliability of Pb-free solder and interconnect materials have led some applications to continue utilizing Pb-based solders with high lead content [37,38]. In the pursuit of Pb-free alternatives, compositions for high-temperature interconnect and attach materials ($T_{operation} > 350\ ^{\circ}C$) often incorporate elements such as Cu, Ag, Au, Sn, Ni, In, Zn, Al, and Ge. As shown in Figure 1-1Figure 1-7, among these candidates, sintered Ag, sintered Cu, Ag-based materials, and Transient Liquid Phase Sinter (TLPS) exhibit the highest operational temperature capabilities [39–41].

The materials available for electronic interconnect and attach application are usually split between solder and sintered materials. As shown in Figure 1-8, the fundamental difference between solders and sintered materials is that solders experience full melting during its processing, while sintered materials never cross their corresponding melting temperature. Solders and sintered interconnect materials must have high thermal and electrical conductivities. To avoid excessive creep, and creep-fatigue, which is known to be the main failure mode in electronics [42,43], the

operational temperature of the solder and sintered materials must not exceed 80% of their melting temperatures.

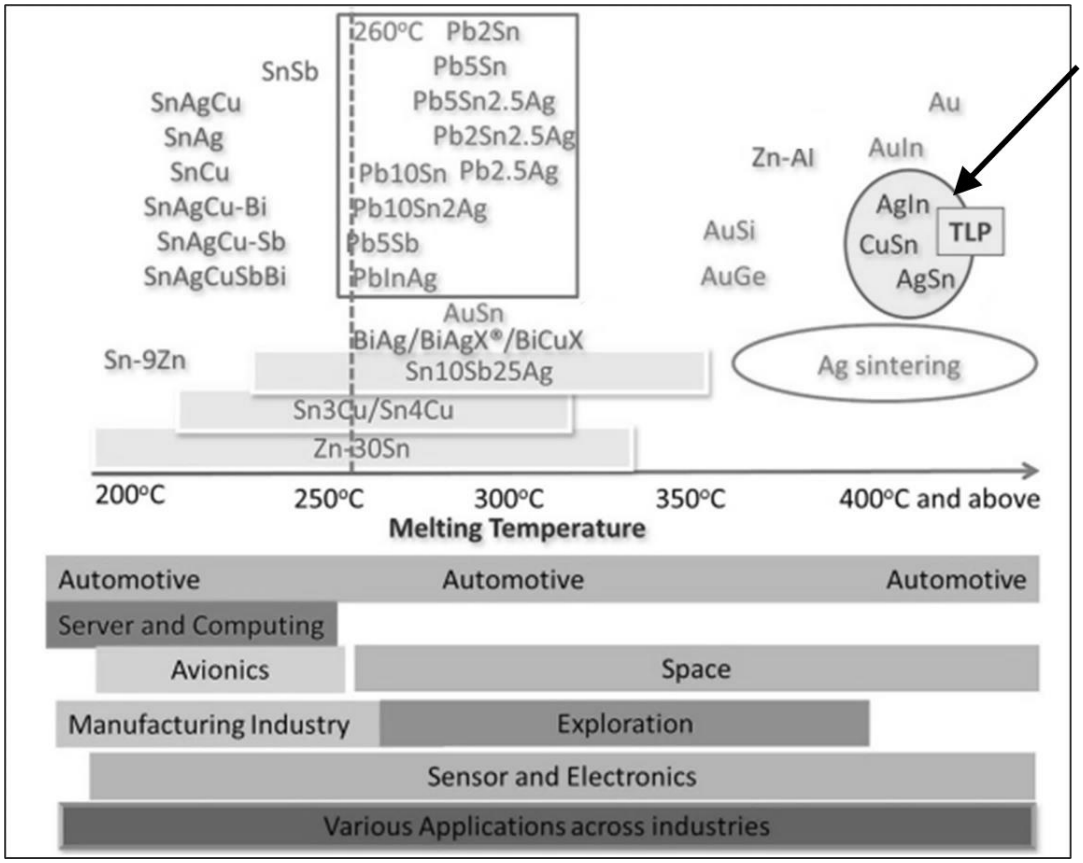

Figure 1-7: High-temperature Pb-free and Pb-based solders for different range of operational temperatures, and their corresponding applicational use [39]**.**

One of the main reliability concerns of solder and sintered interconnect materials is voiding, which are usually originating during the processing stage [44–47]. The voids are a source for stress concentration which combined with the brittle nature of most of the solders and sintered materials can initiate and exacerbate crack formations. Thus, multiple efforts are invested in designing novel temperature profiles [48,49], unique processing atmospheres such as inert and vacuum

atmospheres, advanced manufacturing methods that utilize lasers [50], ultrasonic equipment [51–53], flash-sintering [54], and field assisted sintering [55]. Because void generation is usually due to the presence of flux and organic binders, the use of reducing atmospheres, inert atmospheres, and vacuum-assisted solutions are sued. Figure 1-9 shows the advantages of using controlled atmospheres when processing electronic materials. However, due to complexity, hazardous molecules and elements, cost, energy demanding, and processing-time, it is desirable to find solutions that simplify the solder and sintered materials processing.

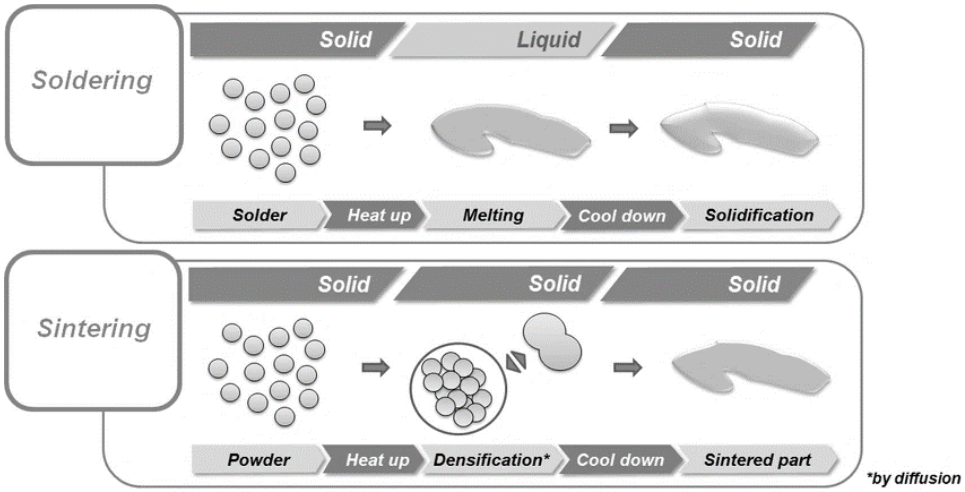

Figure 1-8: Main difference between soldering and sintering processing [56]**.**

Wetting performance of solder is another important factor to consider to achieve good attachment strength, formation control of IMC [57], and diffusion facilitation in the case of diffusion-based interconnect materials. Sn is a popular element in solder and electronic materials design as it offers the ability to improve the ductility and the wetting of the joint [58].

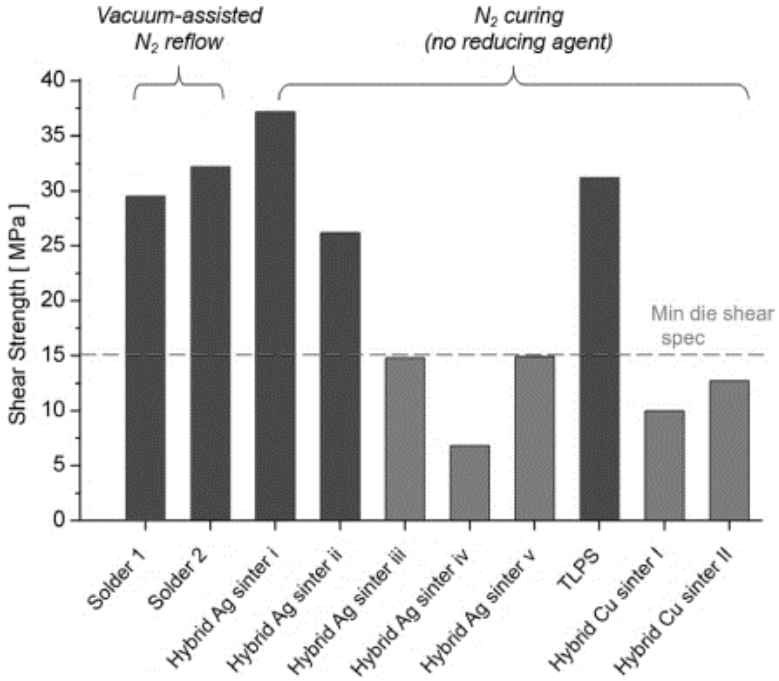

Figure 1-9: Effect of inert and vacuum-assisted atmospheres on shear strength of different solder alloys and compositions [59]**.**

The homologous temperature is defined as follows:

$$T_{homologous} = \frac{T_{operation}}{T_{melting}} \qquad 1.3$$

For $T_{homologous}$>0.4 there is a significant concern of creep phenomena in which the solder experiences mechanical relaxation and irreversible excessive deformations. These deformations are transferred to other parts of the electronic systems. At relatively low homologous temperatures the dominant creep mechanisms are dislocation creep, in which the material experiences plastic deformation through movement of dislocations in the crystal structure. This form of creep mechanisms is usually hindered by grain boundaries, or precipitation of foreign particles. At higher homologous temperatures the hindered dislocations can overcome the blocking elements by means

of changing the slip planes, detachments, and climbing above the crystal obstacles [60]. In such operational thermal conditions, pure-sintered Ag and Cu, as well as the TLPS system excel as their melting point can reach above 450˚C [61,62] as shown in Table 1-1.

Table 1-1: Pb-free electronic materials and their relevant properties.

Electronic Material / Solder	*Melting Temperature* [1] *[°C]*	*Electrical Resistivity* [2] *[μΩ − cm]*	*Cost* [3]	*Reliability and Processing Considerations*
Au	1064	2.21	High	-
Ag	962	1.63	High	-
Cu	1083	1.72	Low	-
Sn	232	12.4	Low	-
In	157	8.37	Moderate	-
Pb	327	21.8	Low	-
Bi	271	129	Low	-
Au-based solders	>280		High	IMC Embrittlement [63]
Sintered Ag	962	2-8	High	Oxidation, Electromigration, Use of nanoparticles [64,65]
Sintered Cu	1083	6.81	Low	Requires low ppm of O_2 during processing [66] and other invert/reducing atmospheres, Use of nanoparticles
Sn-based solders	221-227	10-16	Low	IMC growth, Brittle formation of IMC [67–69]
Pb-based solders	~183	14-16	Low	Contains Pb, Low melting temperature
TLP systems	>415	>11	Low-High	Brittle IMC phases, Long and complex processing [70,71]

[1] [72] [73] [74] [75]
[2] [72] [73] [75] [76] [77] [78]
[3] Normalized to Silver [USD/kg]: Low<.25, .25<Moderate<.75, High>.75 [79]

1.3 Robust Additive Manufacturing Solutions

Recent advancements in Additive Manufacturing (AM) technologies offer potential solutions to overcome some of the manufacturing and design challenges faced by the power electronic and electronic industries. AM enables the production of complex geometries that can accommodate various design requirements, including enhanced cooling configurations, embedded electronics in multi-material assemblies, and electromagnetic-optimized designs for radio frequency (RF) applications, among others [80–83]. In particular, robust AM becomes a viable method for overcoming manufacturing limitations in certain applications, such as far field manufacturing where costly and complex machinery is scarce, and controlled environments are inaccessible [84]. However, one of the main tradeoffs associated with implementing and fully integrating AM into the industrial landscape is the inherent limitation in production time and volume [85]. Consequently, there is a pressing need for faster manufacturing times in open atmospheres without the requirement of complex manufacturing equipment, which serves as a primary motivation for this thesis work.

The available AM methods are diverse and use different technologies such as lasers, light-sensitive materials, and direct printing. The known and popular AM methods are discussed below:

- **Stereolithography (SLA):** SLA utilizes a vat of liquid light-reactive thermoset resin that is cured layer by layer using an ultraviolet (UV) laser or light projector. This process results in high-resolution parts with excellent surface

finish. SLA is often used for creating intricate and detailed models [86,87]. While SLA is predominantly used for polymers, researchers have also explored the feasibility of incorporating heavily metal-reinforced polymer suspensions [88]. This investigation was using a three-stage processing approach in which a green part of heavily metal-reinforced polymer suspension was photo-fabricated by light exposure, followed by debinding and sintering stages to eliminate the residual resin residue and achieve the final metal part.

- **Fused Deposition Modeling (FDM) or Fused Filament Fabrication (FFF):** FDM/FFF is one of the most common and accessible AM methods. It involves extruding a thermoplastic filament through a heated nozzle, layer by layer, to create the final object. It is particularly suitable for rapid prototyping and can accommodate various geometries and material options [89,90]. FDM and FFF are part of the Extrusion-based manufacturing (EAM) and some research was attempted to use FDM for 3D metal printing by mixing metal power and binders to form printable feedstock and filament [91].
- **Semi-Solid Metal Extrusion and Deposition (SSMED):** While FDM/FFF are mostly restricted to polymers, SSMED is working on the same working principle of FDM/FFF, but using semi-solid metal to facilitate the extrusion process. SSMED was shown to successfully 3D AM Sn-Pb alloy with controlled microstructure [92].

- **Selective Laser Sintering (SLS) or Selective Laser Melting (SLM):** SLS and SLM employ a high-power laser beam to selectively fuse and melt powdered materials, such as plastics, metals, or ceramics, layer by layer. The unused powder acts as support during printing, allowing for complex geometries and the creation of functional end-use parts. The flexibility in adjusting various processing parameters, such as laser power, hatching space (spacing between adjacent scanning lines), scan velocity, scanning strategy, powder selection, chemical composition, and atmospheric control, grants these methods precise control over microstructure design, including grain orientation, porosity levels, and phase compositions. Furthermore, these parameters also enable the tuning of bulk properties such as mechanical and electrical properties [93]. Numerical simulations play a crucial role in predicting the resulting micro and bulk structure, as well as the behavior of melt pools and locally heating effects in SLS and SLM [94]. For instance, Figure 1-10 illustrates the simulated effects of different scanning speeds (in mm/s) and applied laser power on the porosity levels of Cu nanoparticles (NP) [95]. The findings reveal that higher laser power and slower scanning velocities lead to lower porosity levels, offering valuable insights for optimizing the manufacturing process. When SLS and SLM are employed with metal powder, careful consideration must be given to selecting compatible lasers and metal powder, ensuring efficient power absorption characteristics [96]. This compatibility is essential to achieve precise

and successful metal 3D printing, facilitating the production of high-quality components for a wide range of industrial applications.

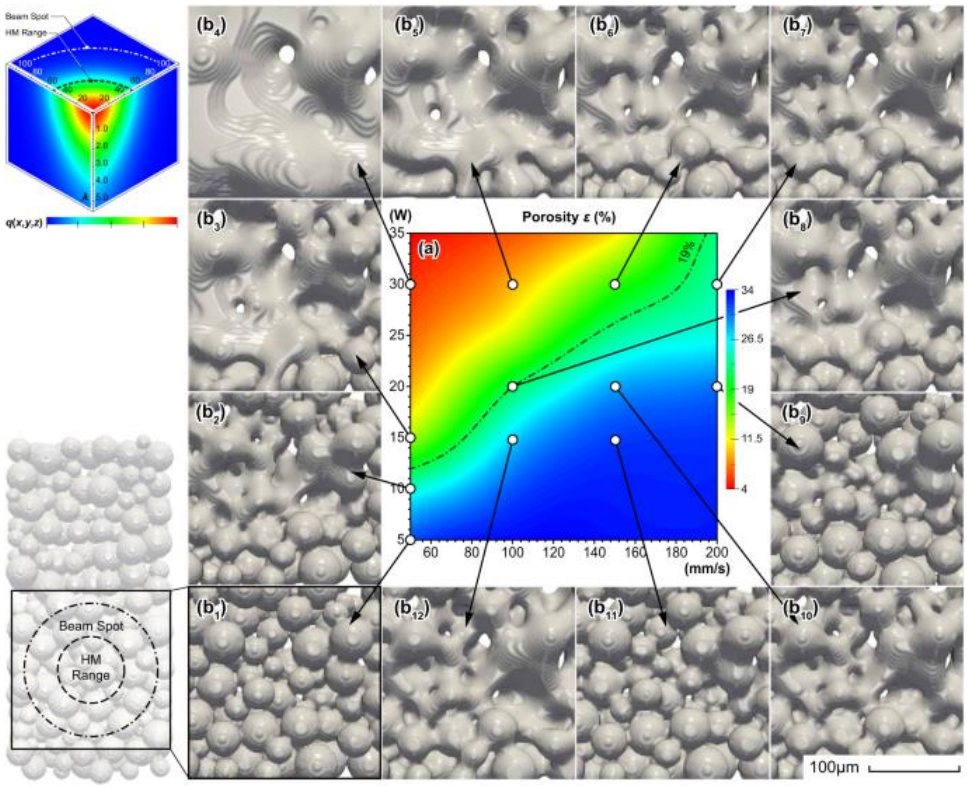

Figure 1-10: simulated SLS process that shows the porosity level (high=blue, red=low) as a function of laser power [W] and scan peed [mm/s]. The simulation shows that lower scanning speeds with higher applied power results in lower porosities levels [95]**.**

In general, SLS and SLM stand out as two promising methods for metal AM. These methods do not necessarily rely on the use of organic binders; however, they do present certain challenges related to robust AM. One notable challenge is the requirement for complex, large, and expensive equipment capable of handling and processing loose powder materials. The handling of loose powder can introduce additional complexities during the printing process, potentially leading to higher manufacturing costs and increased setup times.

Therefore, addressing these equipment-related issues becomes crucial in achieving efficient and cost-effective metal AM using SLS and SLM techniques.

- **Electron Beam Melting (EBM):** EBM is a metal AM process similar to SLM that uses an electron beam instead of the laser beam to selectively melt metal powder, layer by layer. It is particularly suitable for producing high-quality, fully dense metal parts used in aerospace and medical However, EBM AM is considered a more complex and expensive technique compared to SLM. One of the primary reasons for this complexity is the necessity to maintain the metal powder at high temperatures throughout the processing, leading to additional challenges and longer curing times [97]. Consequently, EBM AM is not typically employed for fabricating electronic materials; instead, it finds widespread use in processing titanium and steel alloys, where it demonstrates exceptional performance and material properties [98].
- **Binder Jetting:** This method is similar to SLS, SLM, and EBM which involves powder material, but unlike these methods, binder jetting depositing a liquid binding agent selectively onto layers of the powder material, such as metals, ceramics, or sand, to bind them together and form the desired object [99]. While binder jetting is highly used for metal AM, it is yet to be shown a promising potential for AM of electronic materials due to its relatively complex equipment involved [100].

- **Direct Ink Writing (DIW)**: DIW is a 3D printing technique that involves the extrusion of a paste-like ink through a nozzle, allowing precise deposition of material in a layer-by-layer fashion. The ink is typically composed of a mixture of functional materials (such as polymers, ceramics, or metals) combined with a liquid medium, which provides the necessary viscosity for extrusion. DIW enables the fabrication of complex structures with fine control over material placement, making it suitable for various applications, including soft robotics, tissue engineering, optical devices, functional materials, and advanced electronic devices [101]. Figure 1-11 showcases the three primary DIW material extrusion methods: the screw-driven (Archimedes screw) method, the mechanical piston-driven method, and the pneumatic-based method.

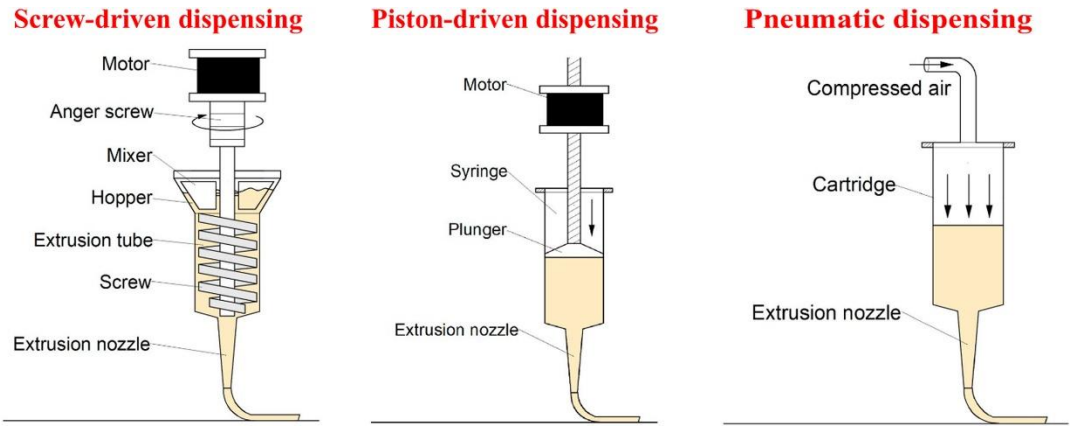

Figure 1-11: the three main DIW material extrusion methods [102]**.**

DIW stands out as a relatively straightforward method with a wide array of matured printers and equipment solutions for AM. While powder-bed methods often yield exceptional material properties, DIW offers a distinct

advantage in fabricating multi-material structures. This advantage stems from its ease of stacking multiple syringes and extrusion devices containing different materials, enabling their seamless utilization either sequentially or in parallel. This unique capability empowers DIW to produce complex and functional designs, integrating diverse materials in a single fabrication process, a feat that may be challenging for other AM techniques [103,104]. However, unlike the self-support of powder bed methods, DIW usually require some sort of support structure, that can later be removed during the post-processing process [105].

1.3.1 AM of Electronics Materials and Electronic Devices

Among the discussed additive manufacturing (AM) methods, SLS, SLM, and DIW stand out as the most promising techniques for manufacturing electronic components. Their versatility lies in their capability to work with a vast variety of materials, handle different temperatures, and accommodate diverse post-processing techniques. Unlike the challenge of AM to manufacture large-scale parts [106], electronics production demands micro-scale and nano-scale precision and capabilities.

To address these stringent requirements, significant efforts have been directed towards developing micro-scale capabilities for manufacturing electronic materials using SLS and SLM technologies [107–109]. The inherent small spot size of the laser beam in these methods allows for fine feature resolution and intricate electronic component fabrication. Additionally, as shown in Figure 1-12, numerous studies have explored the application of AM in producing conductive traces on various substrates,

including flexible substrates [110], using different inks [111], pastes and materials [112–114].

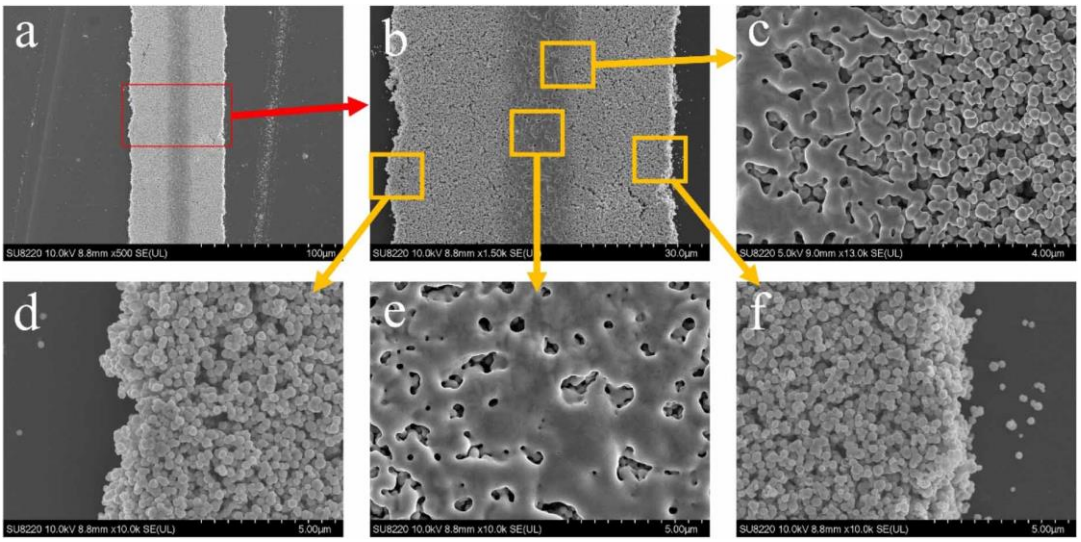

Figure 1-12: Use of SLS to manufacture conductive traces using Cu nanoparticles [110]**.**

Numerous studies have explored the integration of interconnect materials with additive manufacturing (AM), particularly for applications in harsh environments. These investigations demonstrated the successful printing of conductive Ag and Cu inks onto poly-ether-ether-ketone (PEEK) substrates, which were then subjected to rigorous tests, including wire pull and drop-shock tests, highlighting their robustness and reliability [115]. Furthermore, other notable research endeavors showcased varying integration levels of AM for electronic devices, featuring conductive traces capable of operating at high temperatures exceeding 285˚C [116].

2 TRANSIENT LIQUID PHASE SINTER (TLPS)

Among the potential solutions for material selection, TLPS emerges as a promising candidate for interconnects and die attach materials. TLPS is a metallurgical process that involves controlled melting and subsequent solidification of a transient liquid phase. This process is utilized to achieve desired material properties, including enhanced creep resistance, high electrical and thermal conductivities, and corrosion resistance. During TLPS, various IMC phases or solid solutions are formed, leading to a thermodynamically stable material structure. One distinctive feature of TLPS materials is their ability to be processed at relatively low temperatures (<350 ˚C), while offering high operational temperatures exceeding 800 ˚C [117].

2.1 Working Principles of TLPS

2.1.1 Eutectic Binary Metal System

In basic solders, two metal constituents, A and B, are commonly alloyed together. The behavior of these solder alloys can be understood through a binary phase diagram, as shown in Figure 2-1.a, which represents a generic eutectic system. The phase diagram illustrates the relationship between the composition of the alloy and its temperature. The eutectic system is of particular interest in solder alloy design due to its unique characteristic, which allows for efficient melting at lower processing temperatures. The eutectic composition, denoted as $C_{Eutectic}$, is the point at which the alloy has the lowest melting temperature, $T_{Eutectic}$. At this specific composition, the

phases α and β coexist in equilibrium during solidification and melting. Consequently, the solder alloy exhibits a sharp melting and solidification point at $T_{Eutectic}$.

T_A and T_B indicate the melting points of the pure metal constituents A and B, respectively. Phases α and β in the diagram are referred to as solid solution phases. Below the eutectic temperature $T_{Eutectic}$, these phases have their corresponding solvus limits. The solvus limits represent the maximum solubility of one constituent in the crystal lattice of the other. In other words, it defines the composition range within which the phases α and β can coexist as individual solid solutions. If the alloy composition falls within the solvus limits, the microstructure will consist of either phase α or phase β, depending on the composition. However, when the alloy composition lies outside the solvus limits, any addition of opposing constituent particles will lead to a change in the microstructure, resulting in a mixed phase region denoted as $\alpha + \beta$.

During solidification, as the temperature decreases, the alloy will pass through various phase regions on the phase diagram, leading to the formation of specific and mixed microstructures. As shown in Figure 2-1.b, the liquidus line represents the boundary between the liquid phase and the mixed solid and liquid phase regions $\alpha + L$ and $\beta + L$, indicating the temperature $T_{Liquidus}$ at which solidification begins during cooling. On the other hand, the solidus line represents the boundary between the solid solution phases α and β, and the mixed regions $\alpha + L$ and $\beta + L$, indicating the temperature at which solidification is complete during cooling.

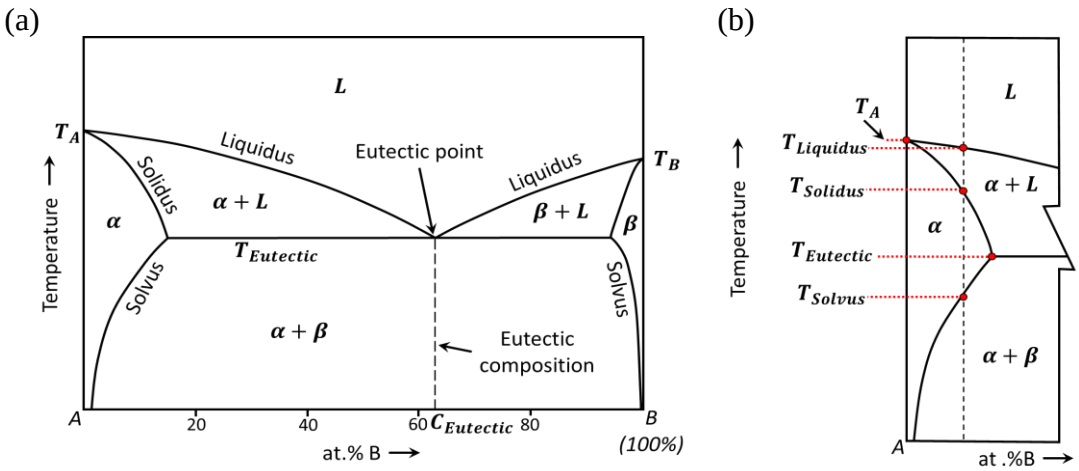

Figure 2-1: Generic binary phase diagram with pure elements A and B (a). Indication of key temperatures (b).

Eutectic solders have the advantage of a sharp melting point at the eutectic composition, which allows for efficient processing at lower temperatures. However, in high-temperature environments, this becomes a drawback as the solder may start to melt or soften at temperatures much lower than those experienced in the application, leading to potential failure or loss of mechanical integrity.

2.1.2 Stages of TLPS processing

To address the challenges of operating at high temperatures, TLPS binary system will often feature a more distinct difference between the melting temperature of the metal constituents A, and B as shown in Figure 2-2. Typically, constituent A is referred to as the High Melting Point (HMP) element, while constituent B is identified as the Low Melting Point (LMP) element. The distinct difference between the constituents' melting points allow to process the electronic material at the processing temperature, T_P, without damaging the rest of circuit. Figure 2-2 shows a TLPS system

where the solid-solution phase, α, is the target phase as it features high melting temperatures.

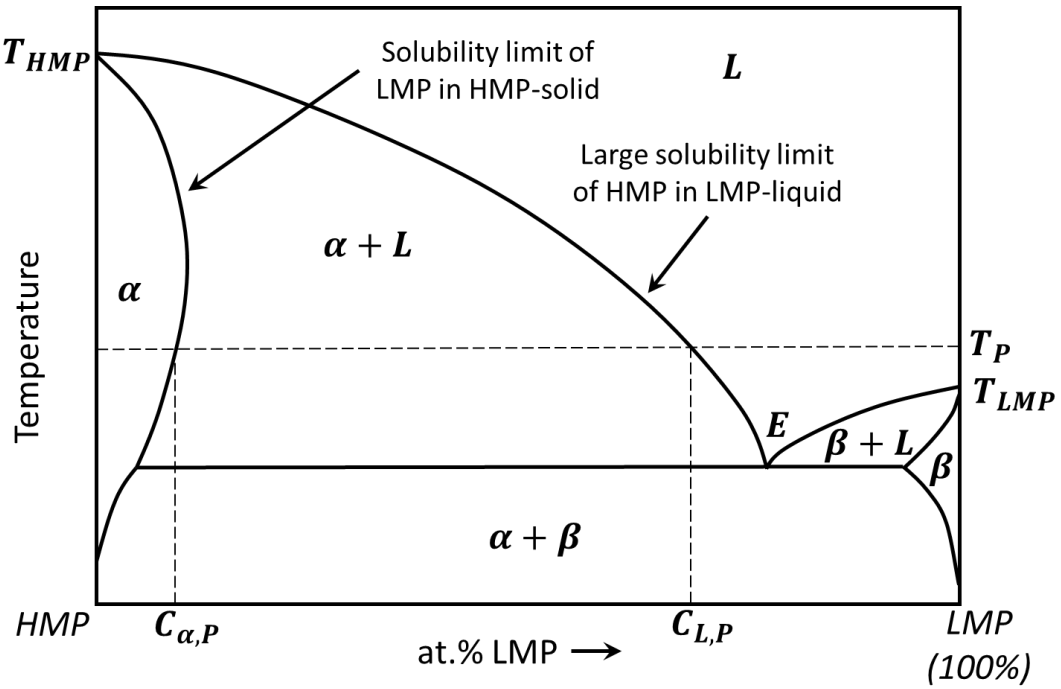

Figure 2-2: Characteristic binary phase diagram of a eutectic TLPS system without IMCs.

The TLPS process is a diffusion-controlled moving interface boundary system which involves four main stages [118–120], illustrated in Figure 2-3.

I. **Heating Stage:** Heating the components from room temperature to the LMP metal melting temperature. Interdiffusion occurs between the LMP metal and the HMP material, leading to changes in solute (LMP) concentration at the HMP/LMP metal interface following the solvus line in the binary phase diagram. This stage usually prompts the mixture to reach the eutectic point at $C_{Eutectic}$ where the metal melts more easily and rapidly.

II. **Dissolution Stage:** Dissolution Stage: Subdivided into two sub-stages: II-1 and II-2.

II-1: Temperature increases from the melting point to the process temperature T_P as shown in Figure 2-2, and solute concentrations at the solid/liquid interfaces change with temperature according to the solidus and liquidus lines in the binary phase diagram.

II-2: Isothermal dissolution occurs at the bonding temperature. The liquid zone width increases, and metallurgical phases (α, β, and liquid) are present. The rate of isothermal dissolution of the HMP particles is influenced by factors such as heating rate and the composition of the LMP metal. At the beginning, liquid phase is inhomogeneous and in a state of super saturation with an average concentration of LMP greater than the eutectic concentration $C_{Eutectic}$. The dissolution stage is lasting few seconds and it is controlled by liquid interdiffusion coefficient D_L [121]. The processes require additional time to homogenized the liquid metal by dissolving additional HMP particles to dilute the liquid before the start of the isothermal solidification.

III. **Isothermal Solidification Stage:** The liquid zone solidifies due to LMP diffusion into the HMP metal at the processing temperature. LMP concentrations at the solid/liquid interface remain unchanged during this stage. The width of the liquid zone continuously decreases until the joint completely solidifies. Isothermal solidification is considered the most important stage, as

the time required for the entire TLP bonding process is largely determined by the time needed for completion of isothermal solidification. The longer time to complete this stage is due to the solid-state diffusion and is controlled by the solid-interdiffusion coefficient D_S which is few orders of magnitudes greater than D_L. At this stage, the liquid is starting to lose LMP particles that diffuse in to the solid HMP matrix, and the direction of diffusion is reversed, which lead to the shrinkage of the liquid phase.

IV. **Homogenization Stage:** Solid-state solute redistribution occurs, leading to homogenization. The temperature for homogenization need not be the same as used in Stages II and III. The process is terminated when the maximum solute concentration at the joint centerline reaches a preselected value. The successful TLPS process requires that the completed resulted alloy has a chemical composition located in the single-phase region of the binary equilibrium phase diagram, and the process approaches this end point through solute or LMP diffusion.

In contrast to the binary eutectic TLPS system illustrated in Figure 2-2 and explained in Figure 2-3, where a homogenized solid solution phase is observed, most TLPS systems exhibit the formation of IMCs due to specific chemical reactions, leading to narrow homogeneity ranges. As illustrated in Figure 2-4, the IMC in the system is denoted as HMP_mLMP_n and possesses a melting temperature represented as $T_{HMP_m\,LMP_n}$. The formation of the HMP_mLMP_n phase arises from a chemical reaction

occurring between the High Melting Point (HMP) and Low Melting Point (LMP) phases, with a concentration denoted as $C_{HMP_m\,LMP_n}$ and the ratio of $\frac{n}{n+m}$. Similar to the process observed in the solid-solution TLPS system, the process outlined in the figure involves a gradual temperature increase from room temperature to above the melting temperature of the solute atoms, T_{LMP}. Upon reaching a temperature where the LMP particles melt, they undergo diffusion and subsequently react with the HMP particles, leading to the formation of the specific IMC phase, HMP_mLMP_n. This reaction continues until all of the molten metal is consumed or until no further HMP particles are available to react with the molten metal. At this stage, the process reaches equilibrium.

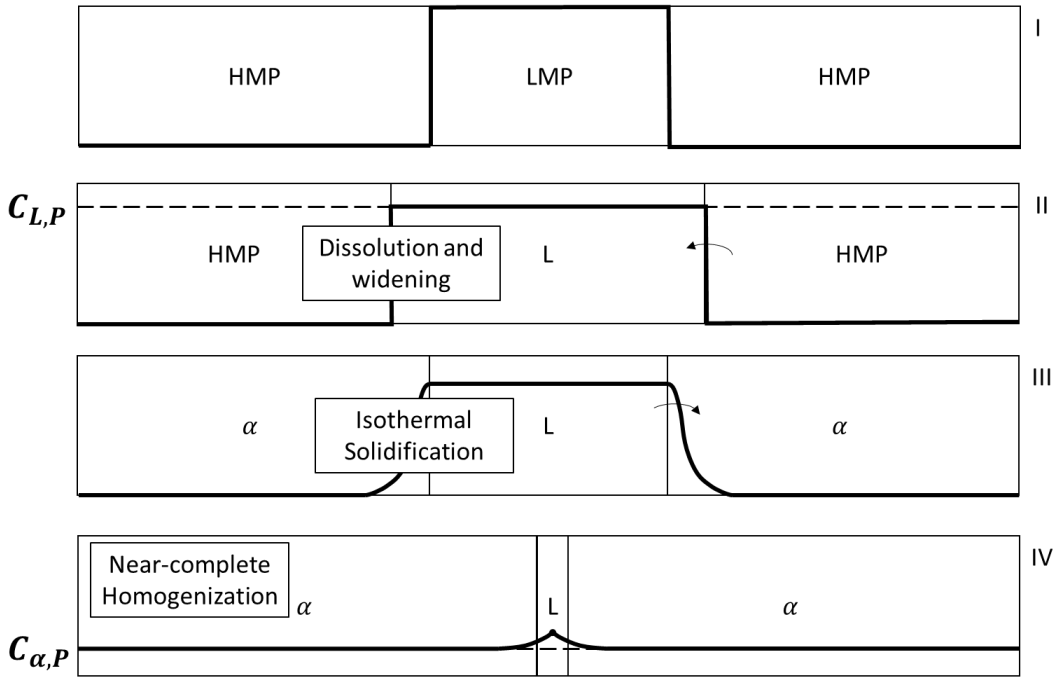

Figure 2-3: Illustration of the four stages of the binary eutectic TLPS system without formation of IMCs.

Many binary metal systems have more than one IMC as shown in Figure 2-5. The system in Figure 2-5 shows two IMCs HMP_mLMP_n and HMP_oLMP_p at compositions $C_{HMP_mLMP_n}$ and $C_{HMP_oLMP_p}$ respectively. These two IMCs feature respective melting temperatures at $T_{HMP_mLMP_n}$ and $T_{HMP_oLMP_p}$. Due to their narrow homogeneity range and high stability, these IMCs tend to be transition to one another through a chemical reaction rather than interdiffusion and the coexistence of both phases as the LMP composition is between $C_{HMP_mLMP_n}$ and $C_{HMP_oLMP_p}$.

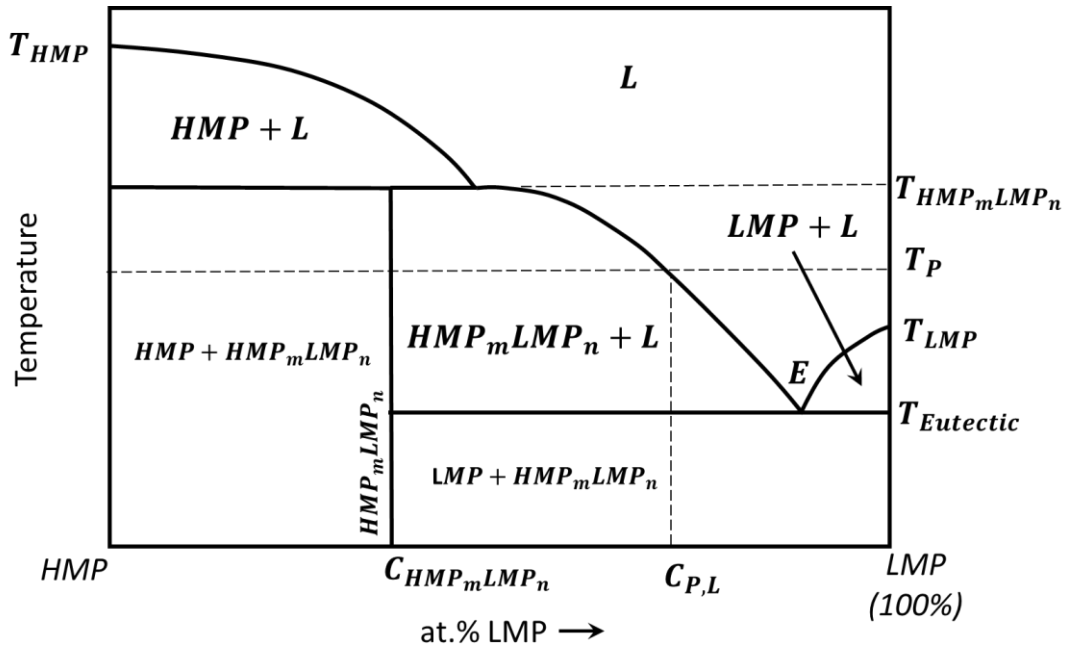

Figure 2-4: TLPS binary system without solubility limits, and one IMC phase HMP_mLMP_n.

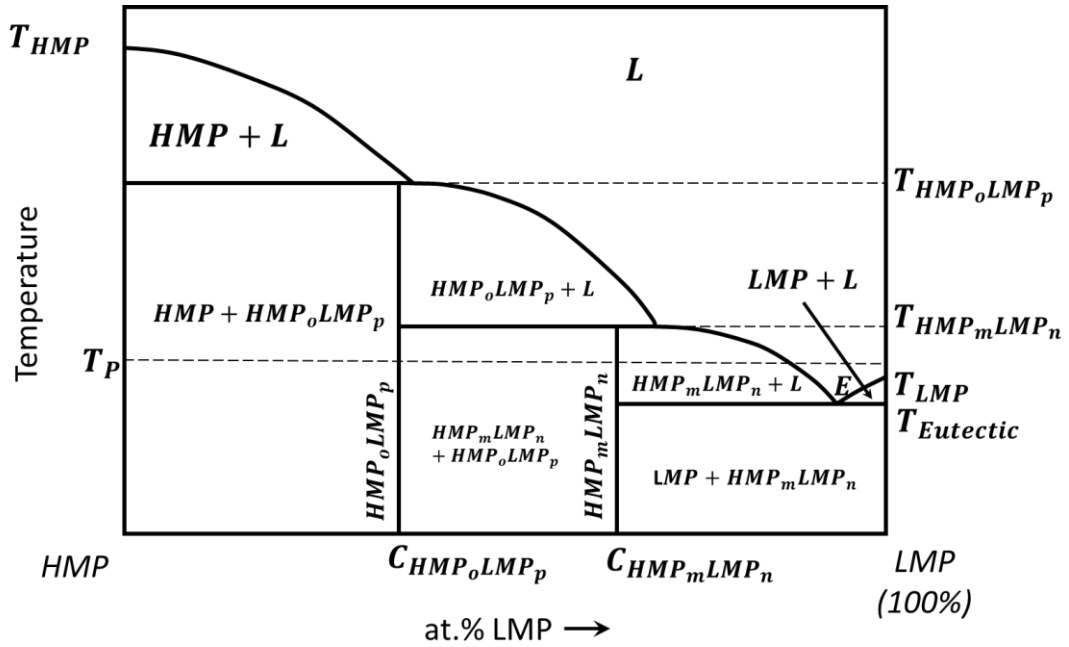

Figure 2-5: TLPS binary system without solubility limits, and two IMC phases HMP_mLMP_n, and HMP_oLMP_p.

2.2 Relevant TLPS Systems

Among the different TLPS systems, various binary systems have been explored, each exhibiting unique characteristics and applications. Among the options of TLPS systems, this work will primarily concentrate on the Cu-Sn, Ag-In, and Ag-Sn systems. These systems have garnered significant attention due to their promising electrical and thermal properties, rendering them well-suited for operation in harsh environments. Furthermore, their reasonable price and availability make them attractive choices for a variety of practical applications. Table 2-1 provides an overview of some of the IMCs that are associated with these different TLPS systems.

Table 2-1: Summery of main IMCs in different TLPS systems.

Interconnect materials	*Intermetallic phases*	*Melting point (°C)*
Au-Sn	$Au_5Sn, AuSn_2$	> 278
Au-In	$AuIn, AuIn_2$	> 495
Cu-In	$CuIn, Cu_{11}In_9$	> 307
Ag-Sn	ε (Ag_3Sn), ζ $(Ag_{85}Sn_{15})$	> 600
Ag-In	Ag_2In, Ag_3In	> 880
Cu-Sn	Cu_6Sn_5, Cu_3Sn	> 415

2.2.1 Cu-Sn System

The Cu-Sn system is one of the most extensively studied and utilized binary metal systems, dating back to the Bronze Age (2000-700 BC [122], with Bronze typically consists of a Cu to Sn ratio ranging from 88-12 to 96-4 [123]. Nowadays however, the Cu-Sn system has gained remarkable popularity in the world of electronic and packaging materials. This system has been extensively studied, primarily because of the widespread adoption of the SAC305 (96.5% Sn, 3% Ag, 0.5% Cu) solder, which serves as the primary alternative to Pb-based solders [124].

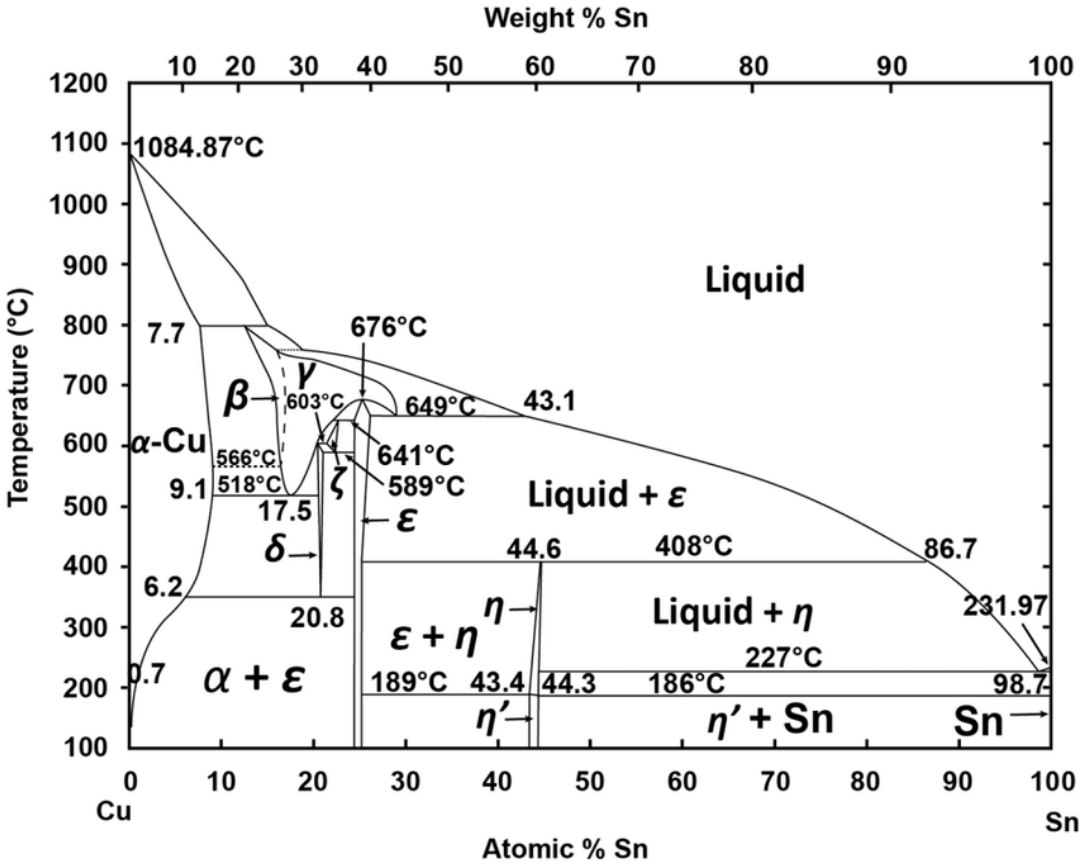

Figure 2-6: Cu-Sn phase diagram [125]**.**

The two main IMCs of the Cu-Sn systems are the Cu_6Sn_5 and the Cu_3Sn which are formed by the following chemical reaction:

$$6Cu + 5Sn \rightarrow Cu_6Sn_5 \quad 2.1$$

$$3Cu + Sn \rightarrow Cu_3Sn \quad 2.2$$

Based on these chemical reactions, when the Cu, as the HMP component, comes into contact with molten Sn, the LMP component, Cu_6Sn_5 is the first IMC phase that forms. With sufficient heat or energy, along with existing chemical potential, the Cu and Sn atoms will continue to diffuse through the Cu_6Sn_5 crystal leading to the

formation of the Cu_3Sn IMC phase. Depending on the temperature, the formation of the Cu_3Sn will proceed until the molten Sn is completely consumed, followed by the complete consumption of the Cu_6Sn_5 phase.

In fact, the chemical reaction and the formation of the Cu-Sn system can be further analyzed based on specific reactions that take place at the interfaces themselves as shown in Table 2-2.

Table 2-2: Summery of chemical interface reaction in Cu-Sn system [126]**.**

Layer	***Interface***	***Chemical Reaction***
Cu_3Sn	Cu/Cu_3Sn	$3Cu + Sn_{diff} \rightarrow Cu_3Sn$
	Cu_3Sn/Cu_6Sn_5 interface on the Cu_3Sn side	$Cu_6Sn_5 + 9Cu_{diff} \rightarrow 5Cu_3Sn$
		$Cu_6Sn_5 \rightarrow 3Sn_{diff} + 2Cu_3Sn$
Cu_6Sn_5	Cu_3Sn/Cu_6Sn_5 interface on the Cu_6Sn_5 side	$5Cu_3Sn \rightarrow 9Cu_{diff} + Cu_6Sn_5$
		$2Cu_3Sn + 3Sn_{diff} \rightarrow Cu_6Sn_5$
	$Solder/Cu_6Sn_5$	$5Sn + 6Cu_{diff} \rightarrow Cu_6Sn_5$
	During cooling	$L + Cu_3Sn \rightarrow Cu_6Sn_5$

As mentioned earlier, due to the chemical reaction that is involved in the formation of the IMCs, the systems often show a sharp transition from one IMC phase to another [127]. Such example of lack in interdiffusion between two IMCs and their parent metal is shown in Figure 2-7. Figure shows X-ray line-scan of the Cu-Sn system which features two favorable IMCs, Cu_6Sn_5 and Cu_3Sn.

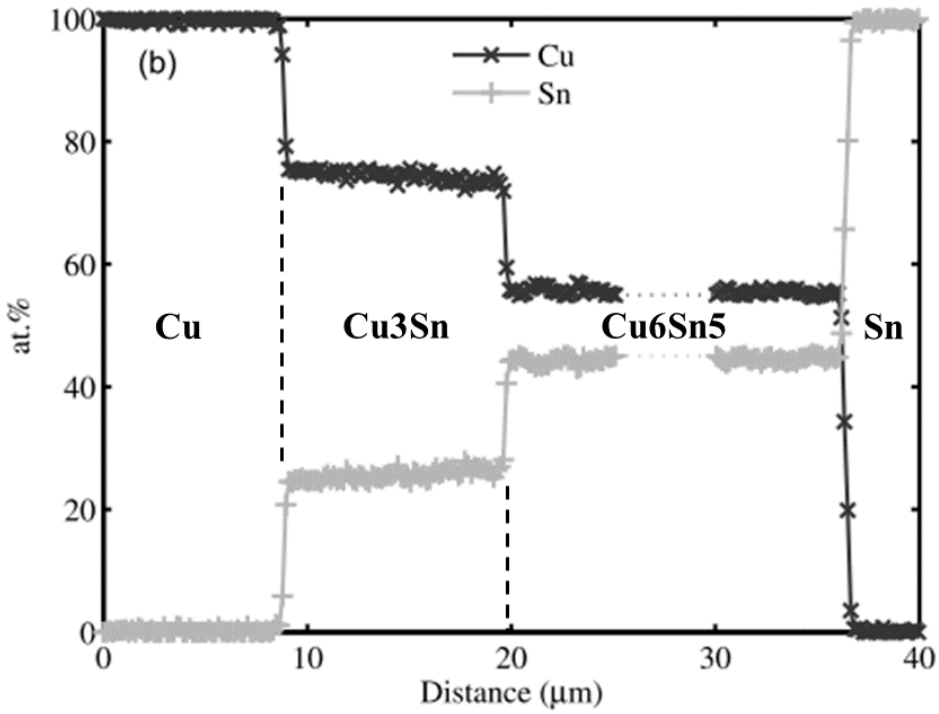

Figure 2-7: Elemental X-ray readings of coupled Sn-Cu system with two resultant IMCs (modified [128]**).**

The formation of Cu-Sn-Ni IMC during TLPS was visualized through in-situ X-ray radiographic imaging, as presented in reference [129]. The paper shows the dynamic nature of the transient process including the solidification of the solder material, initiations and coalescence of micro-voids, and growth of IMC phases and pores. Furthermore, the thermal characteristics of a paste-based Cu-Sn TLPS system were investigated and discussed in [130]. The research demonstrated the practical application of TLPS paste as an attaching material for power diodes and Direct Bond Copper (DBC) substrates.

2.2.2 Ag-In System

The phase diagram of the Ag-In eutectic binary system is shown in Figure 2-8. The figure illustrates that Ag can up take up to 20 at. % In in its α-fcc solid-solution phase and exhibits melting points in which the solidus temperature goes from 961.9˚C for pure Ag, down to 670 ˚C for the maximum uptake of indium in silver. The Ag_3In-bcc IMC is located at around 25 at. % with a peritectoid reaction of $\alpha + \zeta \rightarrow Ag_3In$ upon cooling to 187˚C [131]. The ζ-hcp phase has a narrow homogeneity range at temperatures below 187˚C with indium content between ~25-26%, which increasingly widen above this temperature [132].

The solidus temperature for the ζ phase goes from temperatures of 670˚C down to 205˚C at ~43 at. % of indium. At room temperature and between 31-33 at. % indium, Ag_9In_4 IMC is formed [133]. At 33 at.% indium, the Ag_9In_4 transforms to the $\gamma(Ag_2In)$ IMC phase [134]. The γ phase transform back to ζ at 312˚C making it another potential IMC for high temperature electronic applications. At 205˚C the ζ phase decomposes into mixture of γ and liquid through metatectic reaction [135]. $AgIn_2$ is the last IMC phase of the Ag-In system at 66.7 at. % indium. Between 66.7 at. % and less than 1 at. % of indium, the system is a mixture of indium and $AgIn_2$, and at 96.7 at. % the system experiences a eutectic reaction at 144˚C.

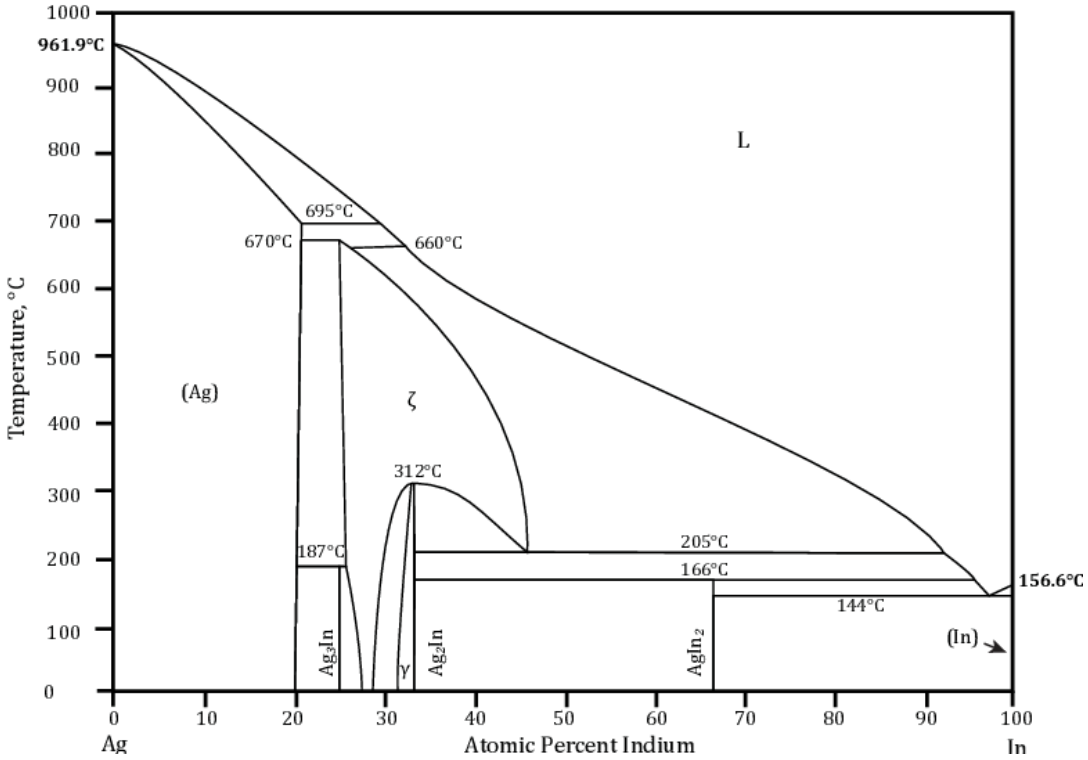

Figure 2-8: Phase diagram of eutectic Ag-In system [136]**.**

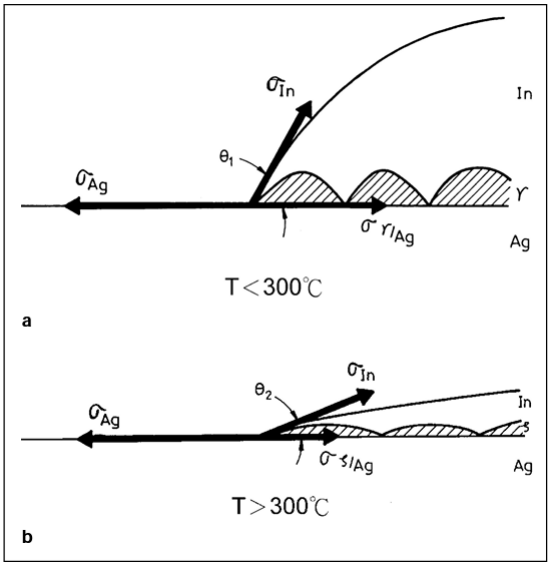

Figure 2-9: Schematics diagrams that show the Ag-In wettability dependence on temperature [137]**.**

According to [138], when pure Indium is available, there are two distinct growth regimes of IMCs. The growth of $AgIn_2$ is controlled by both diffusional processes as well as interfacial reactions, leading to a mixed growth mode. The first, faster, growth mode of Ag_2In at room temperature indicates either at least partial interface control of the reaction, or a relatively high contribution of grain-boundary diffusion. The second, slower growth mode of Ag_2In is diffusion-controlled and is observed at temperatures below 100˚C. An interdiffusion coefficient of $D = 1.16 \pm 3.9\ x\ 10^{-4}\ cm^2\ s^{-1}\ exp(-60.56 \pm 9.2\ kJ\ mol^{-1} R^{-1} T^{-1})$ was derived from the Ag_2In IMC growth-constant data, suggesting rate control by interstitial diffusion in Ag_2In. During the second (slower) stage of Ag_2In growth at room temperature and during the growth of Ag_2In at elevated temperatures, a parabolic growth of Ag_2In persists, which is compatible with diffusion-controlled growth.

The selection of Ag-In TLPS for this study was particularly intriguing due to its exceptional potential previously shown as an electronic material [78,139]. The interface of $\zeta - fcc$ phase and Ag produces superior wettability results over the interface of γ and Ag due to smaller lattice mismatch, and the wettability of the molten indium is significantly enhanced at temperatures above 300˚C as shown in Figure 2-9 [137]. The introduction of 19 at.% In into the Ag-In system has been found to enhance the ductility of silver, and increase the ultimate tensile strength of pure silver by 3.3 fold [140]. Ag-In TLPS systems have also demonstrated remarkable reliability, with die shear stress values exhibit a notable rise during isothermal aging at 300˚C,

reaching up to 59.9 MPa after 2000 hours [141]. In addition, the incorporation of indium into silver alloys leads to a significant improvement in their anti-tarnishing properties. The Ag-19In alloy exhibit a sulfurization reaction rate approximately 22.8 times slower than pure silver, contributing to enhanced tarnish resistance [142]. Addition of In to Ag-based joints for high temperature applications was also showed improvement to oxidation resistance of the joints [143].

2.2.3 Ag-Sn System

The phase diagram of the Ag-Sn eutectic binary system is shown in Figure 2-10. The composition of the α-fcc solid solution ranges from pure silver to about 12 at. % Sn at room temperature with a solidus line that goes from 961.93˚C down to 724˚C at ~12 at. % Sn. At room temperature, Ag can dissolve up to 10 at. % Sn through substitutional diffusion of Sn in Ag, whereas Sn has practically no solubility of Ag at room temperature, and the diffusion mechanisms of Ag in Sn is interstitial [144]. The crystal structure of the solid-solution is changing from face center cubic to hexagonal close pack (hcp) at near 13 at. % Sn. The ζ-hcp (Ag_4Sn) phase has a liquidous line that goes from 724˚C down to 480˚C making it highly attractive phase for high temperature applications [145]. Between 24-25 at. % Sn, and upon cooling the temperature below 480˚C, the system goes from $\zeta + liquid \rightarrow Ag_3Sn$. The Ag_3Sn IMC phase has a diffusion coefficient of $6.6e^{-16} cm^2 s^{-1}$ which is significantly larger compared to the diffusion coefficient for substitutional Sn in Ag, as well as the interstitial Ag diffusion in Sn, and therefore the IMC might develop even in room temperature conditions.

When the nucleation sites of the ζ-hcp (Ag_4Sn) and the Ag_3Sn are at the interface of the two metals, the chemical reactions that take place are as follows:

$$3Ag + Sn \rightarrow Ag_3Sn \quad 2.3$$

$$4Ag + Sn \rightarrow Ag_4Sn \quad 2.4$$

With corresponding Gibbs free energy of $-89.3kJmol^{-1}$ and $-113.3kJmol^{-1}$ at 150˚C [146], which favors the formation of the ζ phase. In contrast, if the nucleation is formed inside the Ag particles, where the Sn particles are diffused in the Ag lattice as the solute atoms, the reaction will follow as follows:

$$\frac{10}{3}Ag + \frac{2}{3}Sn \rightarrow Ag_3Sn \quad 2.5$$

$$\frac{40}{9}Ag + \frac{5}{9}Sn \rightarrow Ag_4Sn \quad 2.6$$

With corresponding Gibbs free energy of $41.79kJmol^{-1}$ and $-69.8kJmol^{-1}$ at 150˚C, which also favors the formation of the ζ phase. Last, when the nucleation of the Ag-Sn IMCs originates inside the Sn-β phase, the change in Gibbs free energy can be calculated based on the reactions as follows:

$$Ag + \frac{1}{3}Sn \rightarrow \frac{1}{3}Ag_3Sn \quad 2.7$$

$$Ag + \frac{1}{4}Sn \rightarrow \frac{1}{4}Ag_4Sn \quad 2.8$$

With corresponding Gibbs free energy of $-20.8kJmol^{-1}$ and $-25.1kJmol^{-1}$ at 150˚C, which in this case, favors the formation of the Ag_3Sn IMC phase.

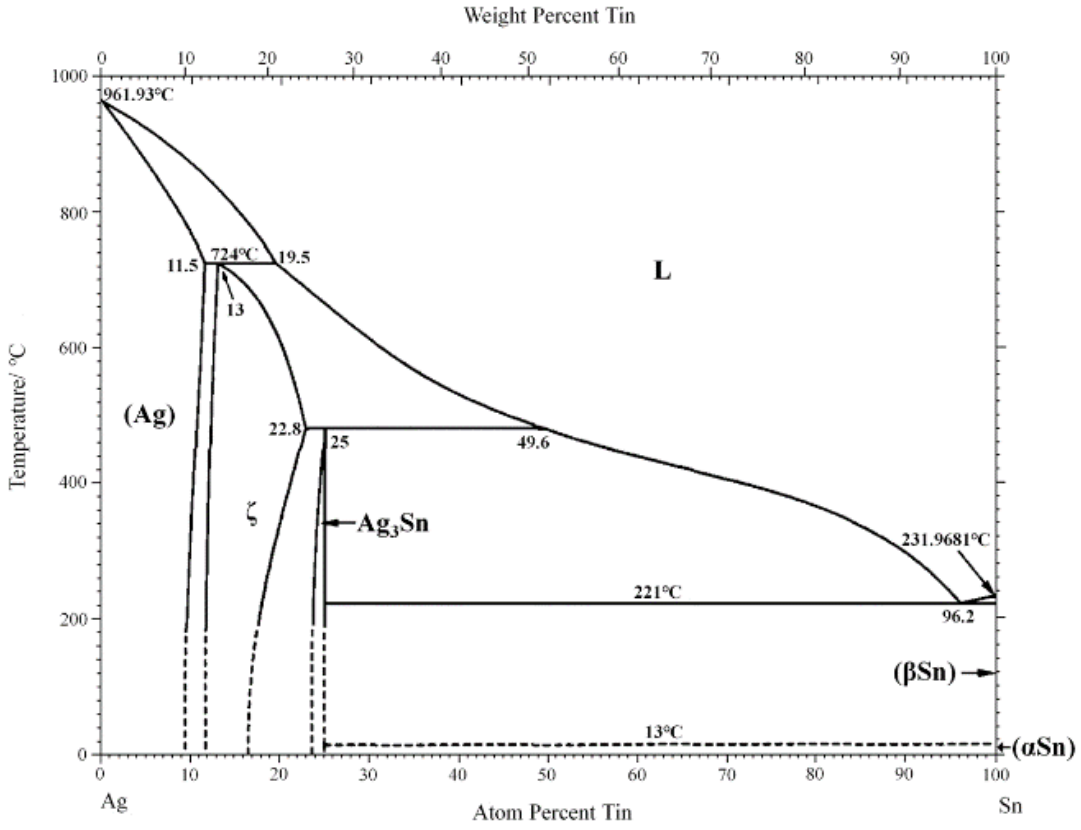

Figure 2-10: Phase diagram of eutectic Ag-Sn system [147]**.**

In both the binary metal systems, with the LMP maintained below 20 at.%, the Ag phase effectively absorbs the LMP, forming a solid-solution matrix. Particularly in the Ag-Sn system, at processing temperatures below 300 ˚C, the formation of the stable Ag_3Sn phase predominates. This specific phase exhibits a melting temperature of 480 ˚C [148] and possesses desirable thermal and mechanical properties [147,149]. Additionally, Ag_3Sn demonstrates low electrical resistivity, reaching values as low as 11.42 $\mu\Omega \cdot cm$ when formed in sheet configuration [77].

2.3 TLPS in a Paste Form

As discussed above, TLPS joints and interconnects are formed by a liquid-solid type of sintering process that involves two metals, one with low melting point, and the second with high melting point. During the sintering stage, the low melting point metal melts and diffuses into the solid-state high melting point metal. There are two main methods in which this process happens, either by pressing the two or more layers of metal against each other, or by mixing the two metal powders and binding them together to form a paste. Both methods are shown in Figure 2-11.

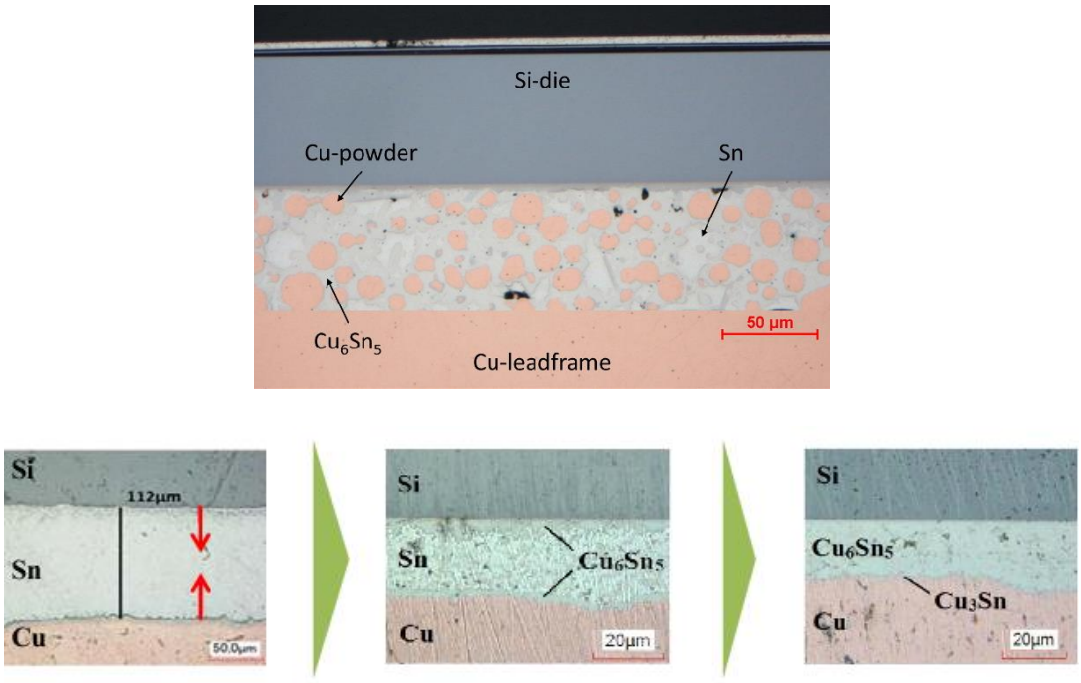

Figure 2-11: Formation of TLPS die attach in a paste configuration (top) [150]**, and sheet configuration (bottom)** [151]**.**

The kinetics of the diffusion reactions in the sheet method are relatively slow due to the small surface to volume ratio [152]. The small surface to volume ratio

effectively decreases the potential energy that helps drive the sintering process [153]. On the other hand, the paste method introduces the use of micrometer and nanometer sized particles to increase the surface to volume ratio, and thereby supply more driving force to the sintering process [154] An equation that summarizes the influence of the multiple factors that governs the driving force of the sintering process can be written as [155]:

$$DF = P_a\phi + \gamma_{SV}K \quad 2.9$$

Where P_a is the applied pressure, ϕ is the stress intensification factor, γ_{SV} is the surface energy, and K is 1/r where r is the particles radius. In addition, the paste can be screen printed or syringe printed on the substrate and can accommodate surface roughness. In the paste form, when the low melting temperature metal melts, the liquid phase coats the solid-state particles and contributes to the densification process through van der Waals and capillary forces [156]. During TLPS sintering, the diffusion process happens at the solid-liquid interfaces. The aim of the TLPS material is to achieve an intermetallic phase that has high melting temperature. Based on a phase diagram of a given metal system, the goal-ratio of the two metals can be determined.

In a paste form, the powders require a binder in the form of flux. The flux has two main goals: First, the organic flux serves as a binder to the powders to form a pasty mixture. Second, the organic flux carries acids that react to remove metal oxides when the temperature rises and the organic binder evaporates, thus exposing fresh surface on

the solid powder and reducing dross in the liquid, promoting intermetallic diffusion [157].

2.3.1 Organic Binders

While TLPS solutions can be implemented through metal-sheet bonding, integrating them with AM requires the utilization of printable materials. A vital step in the integration process involves combining metal powder with organic binders (flux) to form a printable paste-like material. Dispensing this paste efficiently using syringes while preserving its structural integrity until the application of heat is crucial to facilitate the integration of TLPS materials into diverse AM applications.

The organic binders are complex organic systems composed of various ingredients such as activators, vehicles, solvents, and other additives [158]. Activators play a crucial role in facilitating the removal of metal oxides from surfaces, and their effectiveness increases with temperature. Vehicles, which can be solids or non-volatile liquids, form a coating on the surfaces of HMP materials. These vehicles dissolve the metal salts generated during the acid-base reaction between the activators and the oxides and ideally act as heat transfer mediums. Solvents, typically consisting of alcohols, glycols, or glycol ethers, are responsible for dissolving the vehicles and activators. Multiple studies have examined the residue levels of different organic binder compositions [159], as well as their compatibility with Pb-free solders for electrical joining applications [160].

3 OBJECTIVES AND STATEMENT OF WORK

While exhibiting exaptational and reliable thermal properties, to become a fully reliably, competitive, and a consistent holistic-technology, TLPS materials still require additional research and development. The processing of TLPS often results with high porosity levels. The porosity often leads to inferior mechanical, and electrical properties. Moreover, as mentioned in the previous chapter, porous materials are more susceptible to experience destructive-state of oxidation. In addition, the thermally-stable IMC phases and alloys, often prove to be brittle, which limit their ability to sustain stresses, and strains. Thus, fully controlling or eliminating the porosity levels, or the brittle inter-metallic phases, are the current research gaps and challenges associated with the TLPS materials. This study will attempt to address mainly the control and elimination of early staged porosity.

In terms of additive manufacturing, for a given successful AM technique, its processing speed, and general throughput capabilities are crucial. Among different AM processing methods of metallic powders, printing metal in a paste-form offers multiple processing advantages such as: dynamic, robust, low-budget, fast, scalable, and user-friendly processing. However, printing metal powders in a paste form means that the metal powder is mixed with organic materials, i.e. flux. In a perfect and ideal metallic crystal, there is no room for these organic molecules. Thus, these ideal crystals often exhibit optimal mechanical, electrical, and other material properties. In the paste-form however, the presence of organic molecules between the metal powder causing micro,

and macro-scale imperfections in the resultant material. Thus, enhanced research that addresses the efficient removal of the flux content from the final metallic structure, is required.

This research proposes that the first stage of the TLPS processing requires greater focus. Thus, an initial study was conducted to qualitatively identify and observe the problems and research gaps that were discussed above. Figure 3-1 shows a generic temperature profile of a TLPS material that requires to reach to a specific thermally-stable IMC phase. As seen in Figure 3-1, the first stage of the TLPS processing is often in the order of seconds to minutes. In this stage, three main events take place: flux related activity, phase transition, and transient liquid-state diffusion. This stage usually happens during the initial ramping of the temperature, and the beginning of the isothermal holding. In comparison to the isothermal holding and homogenization stages of the TLPS processing, the liquid-state diffusion is dominant in the first stage, and it is at least one order of magnitude faster than the following two steps individually. During the transient process of liquid-state diffusion, flux evaporates, the structure solidifies, and gains enough structural stability. From AM point of view, the fast solidification is crucial for the successful printing of additional layers in the vertical direction. Because short solidification times are not enough for a full metallurgical thermally-stable phase completion, once the 3D structure has reached its final shape, the far-from-equilibrium structure can go through the full and final sintering process. As seen in Figure 3-1, the isothermal holding stage should continue until full

consumption of LMP-rich phases, and the formation of the thermodynamically-, and thermally-stable alloy.

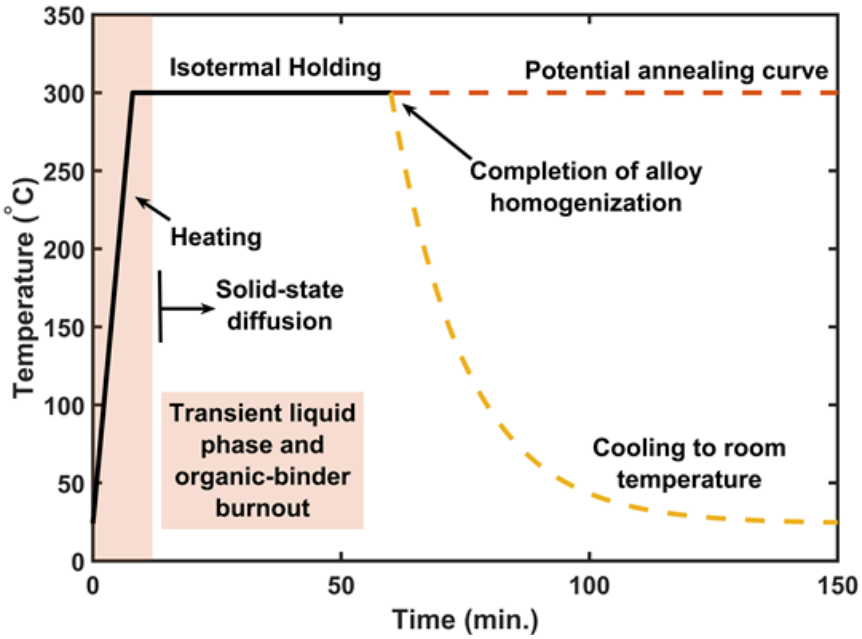

Figure 3-1: Standard TLPS processing temperature profile and its main components.

To make TLPS technology accessible for AM applications, it is imperative to investigate the transient heating stage in detail. Figure 3-2 identifies and maps the key considerations for temperature profile design, material selection, particle size selection, and paste formulation necessary to develop paste-based TLPS materials suitable for AM applications in an open atmosphere. These considerations fall into three main categories: flux performance, liquid phase performance of the LMP material, and diffusion characteristics during the transient phase.

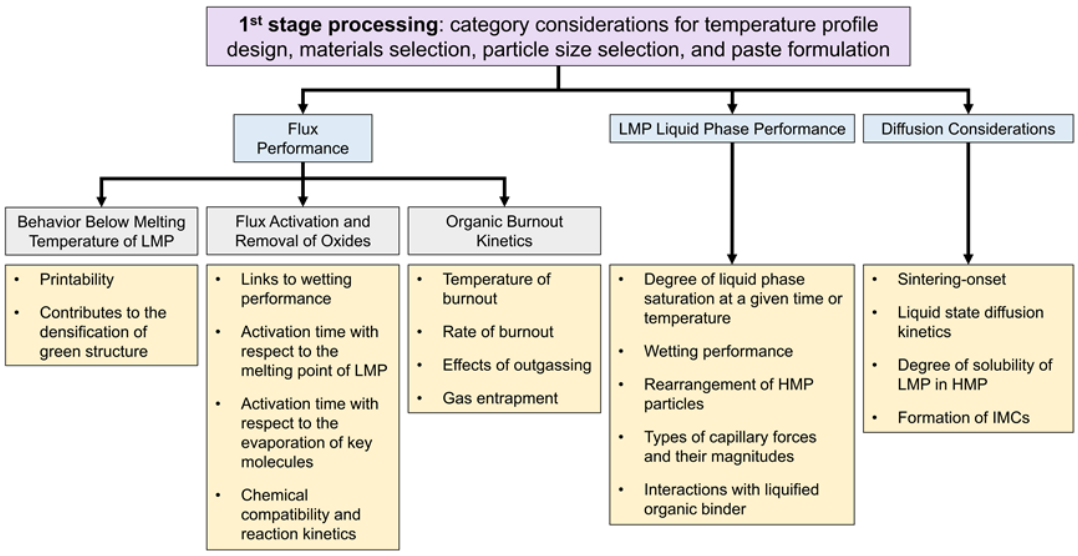

Figure 3-2: Block diagram of the 1st stage processing considerations of TLPS for AM applications.

3.1 Flux Performance

The flux performance can be further divided into three sub-categories: behavior below the melting temperature of the LMP, activation and removal of oxides from the metal particles, and organic burnout kinetics.

3.1.1 Behavior Below Melting Temperature of LMP

The behavior below the melting temperature of the LMP influences paste printability, structural stability between printing rounds, and green structure densification.

3.1.2 Flux Activation and Removal of Oxides

Effective removal of the oxide layer by the flux is critical to achieving intimate contact between metals, enabling diffusion. Inadequate oxide removal results in poor

wetting performance of the LMP liquid phase over the HMP material, leading to incomplete system densification and diffusion. Additionally, considerations such as timing, temperatures for flux removal and activation, and kinetics of chemical reactions play essential roles.

3.1.3 Organic Burnout Kinetics

The final sub-flux category concern with organic burnout and outgassing of the flux, which can introduce gas entrapment and undesired porosity in the final metal structure. Addressing these aspects is crucial to ensure the production of high-quality TLPS-based AM components.

3.2 LMP Liquid Phase Performance

From the perspective of the liquid phase performance of the LMP material, several factors come into play. These include the wetting behavior of the LMP over the HMP material and the extent of metal liquid-phase saturation at a given time or temperature. These factors determine the type of capillary forces acting on the HMP and the effective rearrangement of the HMP. Furthermore, as demonstrated in this work, the presence of the liquified organic binder during LMP melting gives rise to dual liquid phase interactions that influence the final structural integrity of the TLPS material.

3.3 Diffusion Considerations

In addition, TLPS represents a sequential diffusion problem from solid-liquid diffusion, to solid-solid diffusion. The diffusion problem requires consideration of various aspects during the first stage of processing. These aspects include the sintering onset, kinetics of metal liquid-phase diffusion, degree of LMP solubility in the HMP, and the formation of IMCs.

3.4 Preliminary Work

3.4.1 Transitioning to 3D Structures: Selection of Nozzle Size, and Slump Resistance

The transition to full-scale, efficient, and reliable additive manufacturing of 3D printed structures involves multiple challenges that requires exploring various processing solutions and mitigation methods. These challenges included reducing the relatively long time of the conventional TLPS sintering cycle; resisting slump when multiple layers are stacked vertically; achieving uniform adhesion between vertical adjacent layers; maintaining print feature size; facilitating efficient removal of the organic binder; developing 3D printing support structures; and controlling surface finish; all while maintaining the good mechanical, thermal, and electrical properties of the TLPS material.

While reduction in the sintering time between vertical adjacent layers reduces the overall manufacturing time, insufficient sintering time may result in slump and poor stability of the 3D structure. Thus, the sintering time must be optimized between the

time objective and the limiting physical constraints. The process needed to produce a stable 3D structure by permitting the printing of subsequent layers is one in which sufficient flux has evaporated to reduce fluidity and partial reaction has occurred between the two metals in the binary metal TLPS system. In addition, the use of a smaller nozzle size correlates with improved structure definition, stability, and slump-resistance. Figure 3-3 shows the correlation between the combination of heating time and nozzle size, on the slump resistance of the printed TLPS structure.

Ag80In20 alloy consisting of 4-7μm Ag powder mixed with 500 mesh In powder in TACFlux008 (Indium Corp.), with 75% metal loading, was chosen as the material for constructing the 3D structures. The choice of working with Ag particles with a mean diameter of only a few micrometers was designed to improve the sinterability of the paste. Choosing small size particles increases the effective driving force for the sintering process, which is especially important in cases such as this which lack external driving forces, such as are provided by pressure-assisted sintering. The choice of 75% metal loading was designed to achieve viscosity low enough to prevent clogging and pressure build-up during the nozzle-based deposition. The choice of using Ag to In ratio of 80:20 was based on previous research [78] that showed an optimized mechanical and electrical performance for this specific ratio. The choice of TACFlux008 was based on the successful tape tests that verified the adhesion to alumina substrates.

Figure 3-3 shows that a sintering time of eight minutes, together with a nozzle size of 0.51 mm achieved the best-defined structure and a stable result for a sixteen-layer structure. In terms of nozzle size, any nozzle size larger than the 0.51mm nozzle resulted in excessive slump, and the structures were terminated at five printed layers. Care was taken in conducting the multiple sintering/curing cycles to avoid the accumulation of mechanical stresses and deformations, which can pose a threat to the reliability of the overall structure.

While the appropriate nozzle size was identified, it was still necessary to further reduce the intermediate sintering times. To achieve this, the following process sequence was developed. When each individual layer is deposited, enough heat is applied to effectively promote sufficient intermetallic diffusion between particles to stabilize the green structure. Since silver and indium interdiffusion even at room temperature, a relatively short heating period is sufficient to partially evaporate the organic flux, permit interdiffusion, and stabilize the freshly deposited layer. In addition, when depositing the paste on still-hot structures, the residual low melting point material in the previously deposited layer melts, allowing the two layers to mix and bond. Capillary forces contribute to the penetration of the liquified fresh paste into the green structure. This helps to reduce the porosity, and contributes to the overall stability of the 3D printed structure. Furthermore, this method allows the structure to be coated with a uniform surface finish.

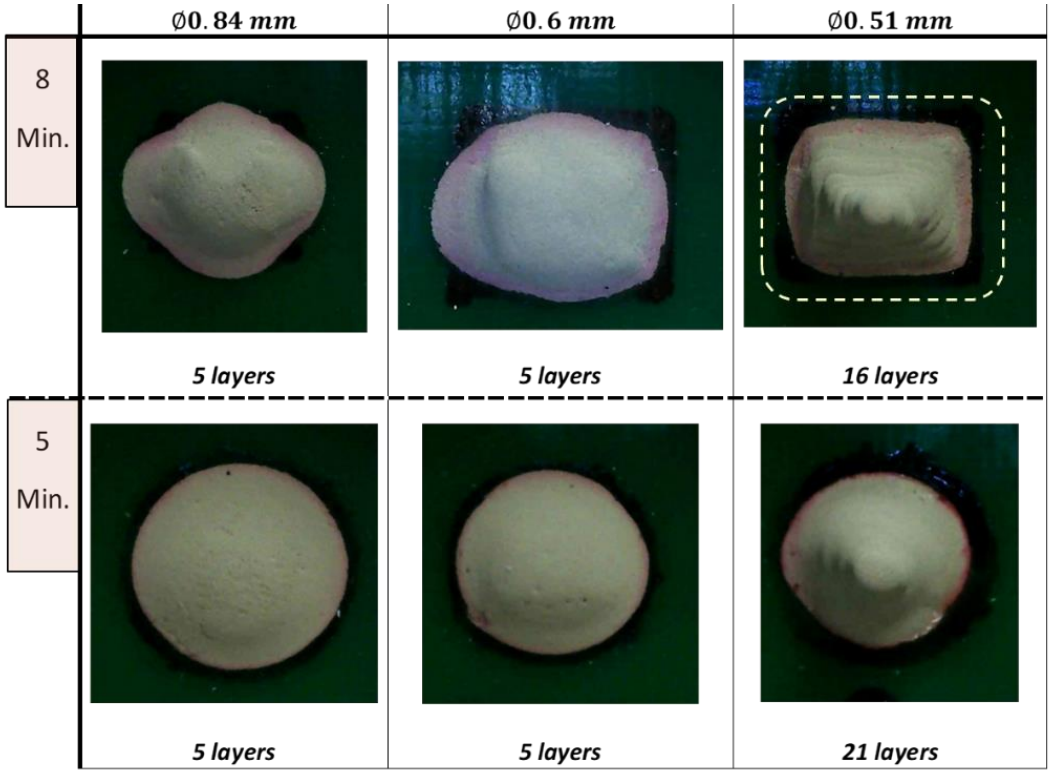

Figure 3-3: The effect of heating time and nozzle size on the stability of 3D printed TLPS structure. The figure indicates the structure will achieve its best stability with an increased heating time, and smaller nozzle diameter.

To allow sharp angles to be printed, an additional step to the process involved creating some support structures in the form of aluminum foils and copper wires. Each layer of the 3D print was deposited and then heated for a duration of three to four minutes at 130°C without a subsequent cooling time. This approach also allows for the creation of denser, more uniform structures. Since the fresh paste was printed on the still-hot structures, the fresh paste penetrated the lower layers and created more uniform and cohesive new layers. The fully printed 3D structures underwent a final post-deposition sintering step for two hours at 300 °C with ramp rate of 40°C/min.

Figure 3-4 shows a printed cantilever beam emerging from a pillar and an unsupported bridge between two pillars. Both the cantilever and the bridge designs reached an approximate height of 6-7 mm. The cantilever reached a length of 3 mm, and the bridge spanned over 15 mm. None-of the designs exhibited a reaction with the aluminum foil support.

Figure 3-4: Self-supporting 3d bridges and cantilever beams were printed with a series of 3-4 min heating cycles at 130°C followed by 2 hr. sintering at 300 °C using a support structure of Al foil on Cu wire.

The cantilever structure was printed on a Cu-plated polyimide board and its pillar remained attached to the substrate after the final sintering. It should be noted that the apparent lifting of the pillars seen in the unsupported bridge is due to their being deposited on an unmetallized, bare polyimide board to allow removal of the bridge as a free-standing structure. If a Cu-metallized polyimide board or a ceramic board had been used, the pillars likely would have remained adhered to the substrate. The free-standing bridge structure was able to act as a cantilever sustaining its own weight

without fracturing. Both the printed cantilever and the bridge demonstrated the ability to 3D print at 90-degree angles despite this maximizing the moment on the printed structures.

3.4.2 Post Sintering Hot Isostatic Press (HIP) Treatment

Another preliminary test was conducted to test the electrical resistivity of different TLPS pastes. The two pastes, samples of Ag80In20 with either TACFlux007 (EP1), or TACFlux008 (EP2) were sent for Hot Isostatic Pressing (HIP) as a post-processing measure. The objective was to investigate the effect on electrical properties, porosity, and microstructure of the sintered material. Both formulations consisted of 91% metal loading with silver maximum particle size of 45μm (-325 mesh), and indium maximum particle size of 27μm (-500 mesh). Both EP1 and EP2 were subject to a sinter profile of 40°C/min ramping rate, followed by isothermal holding at 300°C for one hour, and cooling to room temperature. While exhibiting improved electrical performance, EP1 showed poor adhesion to the alumina substrate, and required a thin layer of bonding paste (BP) in order to adhere to the alumina. The formulation of the BP that was used to attach the EP1 samples consisted of a eutectic phase of Ag and In. The Ag-In eutectic phase is a ratio of 3% Ag with 97% In, and the paste itself consisted of 85% metal loading in TACFlux008. The use of the eutectic phase, with liquidus melting temperature of 143°C, was designed to achieve good wettability with the alumina board, together with minimal cross section, and low electrical conductivity. The bonding paste was heated in the furnace for 15 minutes at 350°C with a ramping

rate of 40°C/min. Both the electrical pastes and the bonding paste were deposited using a stencil with a cross sectional area of 0.1 mm^2. All the pastes were mixed thoroughly to ensure homogenous composition, and fresh paste was scooped randomly with each use of the stencil. The 4"x4" alumina boards were cut to fit a HIP chamber with a diameter of 4 inches. The boards were then cleaned with isopropanol, and fired for 15 minutes at 600°C to ensure a clean surface prior to the deposition of pastes. A total of six boards were sent to the HIP treatment in which each electrical paste (EP1 and EP2) was subject to one of three levels of pressure (5 MPa, 10 MPa, and 40 MPa), and an isothermal hold of 4 hours at 300°C in an inert Argon atmosphere. Before the HIP process, Differential Scanning Colometry (DSC) was performed on a selected EP1 sample. The scan showed that the bonding paste experiences some re-melting during repeating heating cycles. Using an optical microscope, cross-sectional imaging of the same sample showed no significant change in the geometry of the bonding paste or the electrical paste, at which point the samples were determined to be ready for HIP treatment.

The samples subjected to the HIP treatment returned with no observable damage, having survived the four-hour exposure at 300°C and various levels of hydrostatic pressure. Figure 3-5 shows the nominal resistance, measured across 3 cm, before and after the HIP process at various pressure levels. Figure 3-5 on the right shows the data for the samples containing TACFlux008 (Set008). The figure shows that the 5MPa and 10MPa treatment resulted in a decrease in the sample-to-sample

variability of the electrical conductivity. Furthermore, both pressure values achieved more or less the same electrical peak performance. The 40MPa treatment did show an improvement in the overall electrical performance, but to a lesser extent than the 5MPa and 10MPa treatments. Overall, Set008 exhibited improved electrical performance at all pressure values.

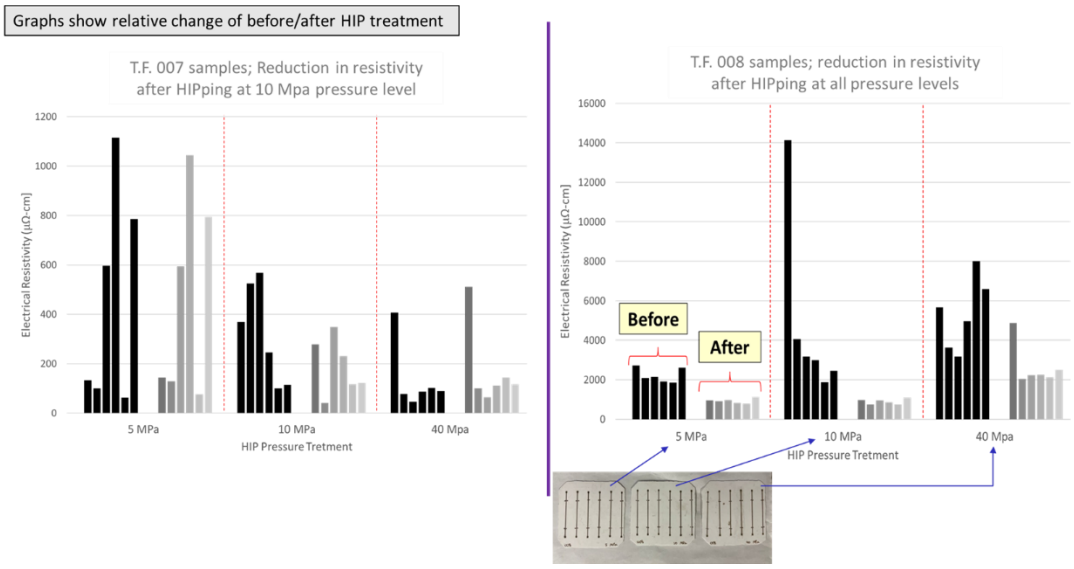

Figure 3-5: Electrical results of the TLPS samples that were went through a HIP treatment. The figure shows that while set008 (right) managed to achieve a consistent reduction in electrical resistance, set007 was showing some electrical improvement, but not a consistent one. A significant electrical improvement can be measured in some of the set007 samples and linked to pore closure due to mechanical yielding of the samples.

Figure 3-5 on the left shows the data for the samples containing TACFlux007 (Set007). The figure shows that samples exposed to 10MPa pressure exhibited a 2-5-fold reduction in electrical resistance. There is minimal to no significant change in electrical performance for the samples exposed to 5MPa and 40MPa. Based on the

results shown in Figure 3-5, it seems that the 10MPa treatment has the best effect on the TLPS sintered material.

Figure 3-6 shows the cross sections of Set007 at the various amount of applied hot isostatic pressure, ranging from the no-pressure reference sample (top left), to the 40MPa sample (bottom right). The cross sections for Set007 also show the adhesion layer that was needed to attach the conductive paste to the alumina substrate. Based on the cross section of the reference sample, it can be seen that the last stage of the TLPS sintering process, the homogenization stage, was not complete. In this micrograph, phase gradients can be seen. In addition, it can be observed that the shape of the pores is irregular, and that the pores are open. These two observations suggest that pore generation is a consequence of improper removal of the flux binder. The large size of the pores can effectively eliminate the possibility that the pores were formed by diffusion. It is also noted that the silver solid solution (lighter) particles are well wetted, and sintering process successfully took place. Unlike in Set007, the ability to wet the Ag particle surface, and particle bridging was not seen in any of the Set008 samples, regardless of the HIPping pressure level. This is an important difference between the two sets, as it has the potential to shed light upon the compatible chemistry that works with the Ag-In TLPS system. The rest of the micrographs of Set007, with HIPping pressure of 5MPa, 10MPa, and 40MPa, show that some mechanical yielding has occurred, and some of the large pores were either diminished, or became isolated to the outer surface due to the HIP treatment. However, while the pore elimination did not

directly translate to a reduction in electrical resistance, some samples, both from Set007 and Set008, showed significant improvement in the electrical conductivity. One possible reason for this is the original irregular pore shapes that might have remained along some of the samples, even after collapsing. Energy-Dispersive X-ray spectrometry (EDS) was conducted on the cross-sections, and verified that the samples that underwent a HIP treatment, have completed their diffusion transformation and achieved full homogenization.

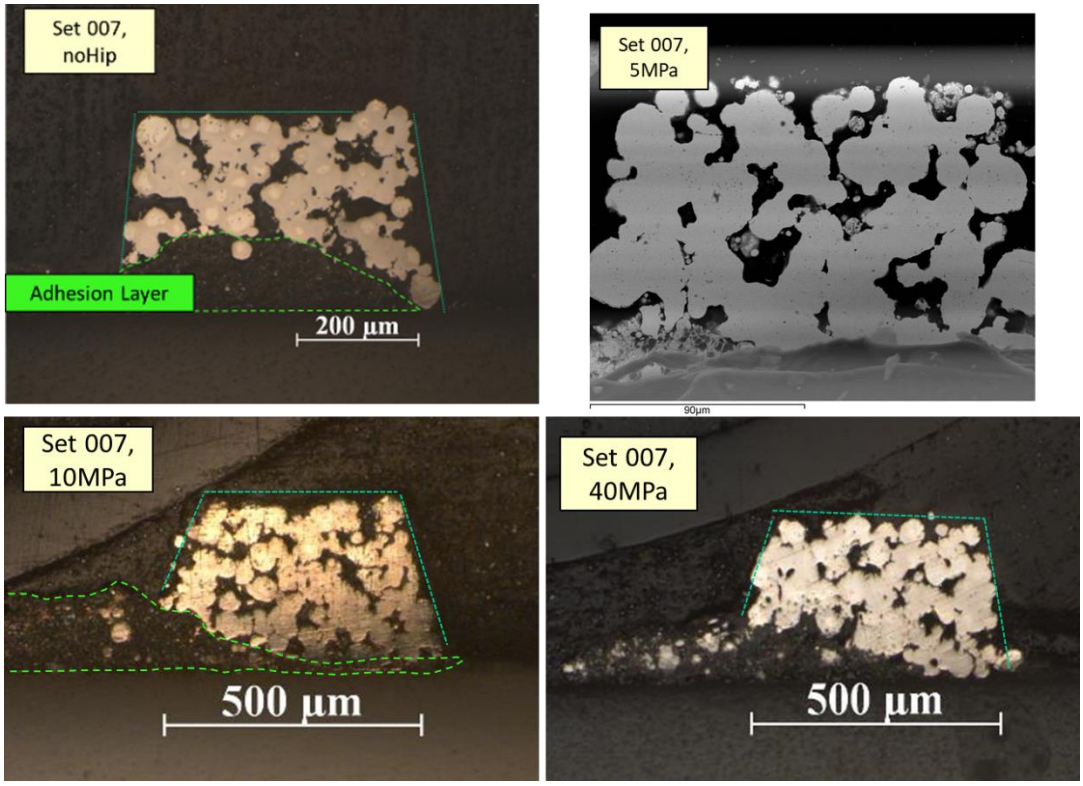

Figure 3-6: The figure shows the effect of HIPping on the structure of the printed samples of set007. Although not clearly observed in the electrical data, the figure shows that some pore elimination was present due to HIP treatment. Since the samples that were sent to the HIP treatment were fully sintered, the pore closure can be attribute to mechanical yielding of the structure.

3.4.3 Weight Loss Kinetics

To design better temperature profiles for the first stage of the TLPS processing, the behavior of the flux must be isolated to gain further understanding of its action. In the initial study, the choice to focus on TACFlux007 was based on previous knowledge of its compatibility with the Ag-In system in terms of electrical conductivity. The flux study measured the mass loss of the flux for a set of temperatures and holding times. Each sample consisted of a small amount of flux, deposited on a thin aluminum tray made from 4 cm x 4 cm aluminum foil. The amount of flux was kept small with an average weight of 0.0317 grams to eliminate thermal mass effects. The aluminum foil was folded into a tray to eliminate thermal conductivity effects and to prevent flux leakage. Each sample was placed on a pre-heated hot plate to eliminate the effect of temperature ramp rate. The samples were measured with a micro-balance before and after heating.

Figure 3-7 shows the results of the weight loss study. Each data point is an average of three samples with ninety-nine samples tested overall. The error bars in Figure 3-7 represent the maximum and minimum of test temperature at a given holding time. Fit lines were plotted for each temperature set. Below the melting temperature of indium, mass loss of TACFlux007 had a linear fit, while for all temperatures above the melting point of indium, the data showed a logarithmic behavior. In terms of additive manufacturing, this graph is significant in designing the temperature profile of the

early-stage sintering as it shows that the early-stage evaporation performance of the flux is highly sensitive to temperatures over the first minute. Thus, removal of more than 70% percent of flux can potentially be achieved within one minute of processing at 300˚C. In addition, if the 300˚C processing temperature is too high for this early sintering stage, it gives a good design criterion for flux formulation in which volatile additives are required to lower the evaporation temperature while keeping the same evaporation kinetics.

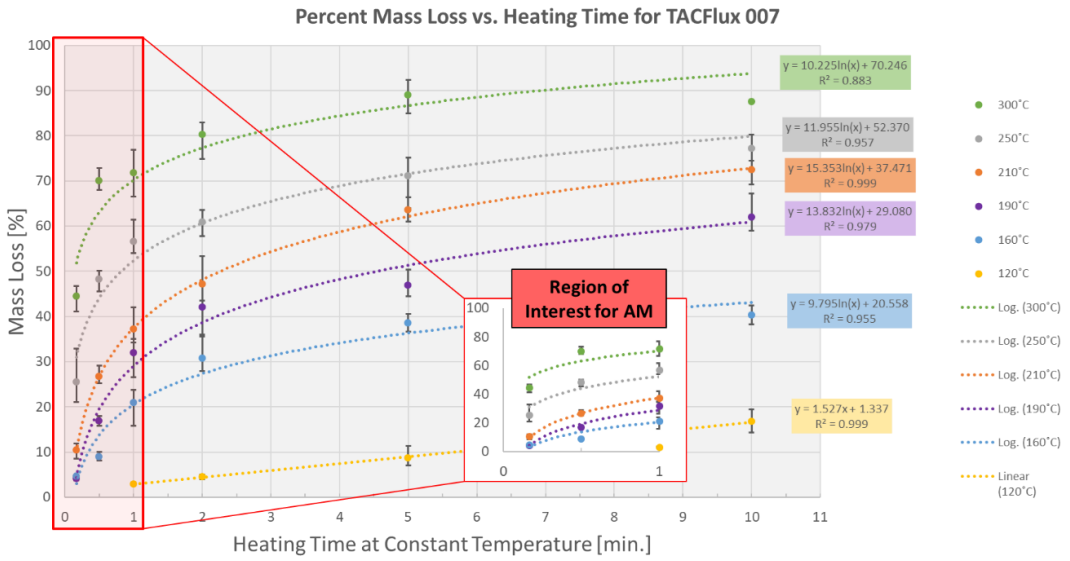

Figure 3-7: Mass loss kinetics of TACFlux 007 at different temperatures at different holding times. The red area shows the region of interest for additive manufacturing capabilities.

3.4.4 FTIR Observations and Analysis

Following the weight loss study, the samples were taken and analyzed using the Agilent Cary 670 FTIR Spectrometer. The FTIR readings were then plotted and analyzed for both constant heating temperature versus variable heating times, and for

constant heating times versus variable heating temperatures. Figure 3-8 shows four stacked-graphs with constant temperatures versus variable heating times. In Figure 3-8, each individual stacked-graph represents a constant heating temperature. In each individual stacked-graph, the outer y-axis shows an increasing heating time, and each individual y-axis shows the absorption amplitude of the IR radiation incoming signal. The x-axis in each of these individual FTIR spectra are the frequencies of the IR spectrum. Peaks in the FTIR absorption spectrum indicate specific frequencies of the incoming IR radiation that were absorbed by certain molecules and functional groups. The absorption of the radiation is translated into different vibrational modes of the absorbing molecules. The corresponding absorption amplitude of these peaks correlates with the molecular concentration of the absorbing species. Figure 3-8 shows that with increased temperature, several peaks transform faster. In addition, during the FTIR sample dismounting, it was clear that the samples viscosities, stickiness, and crystallinities have different levels.

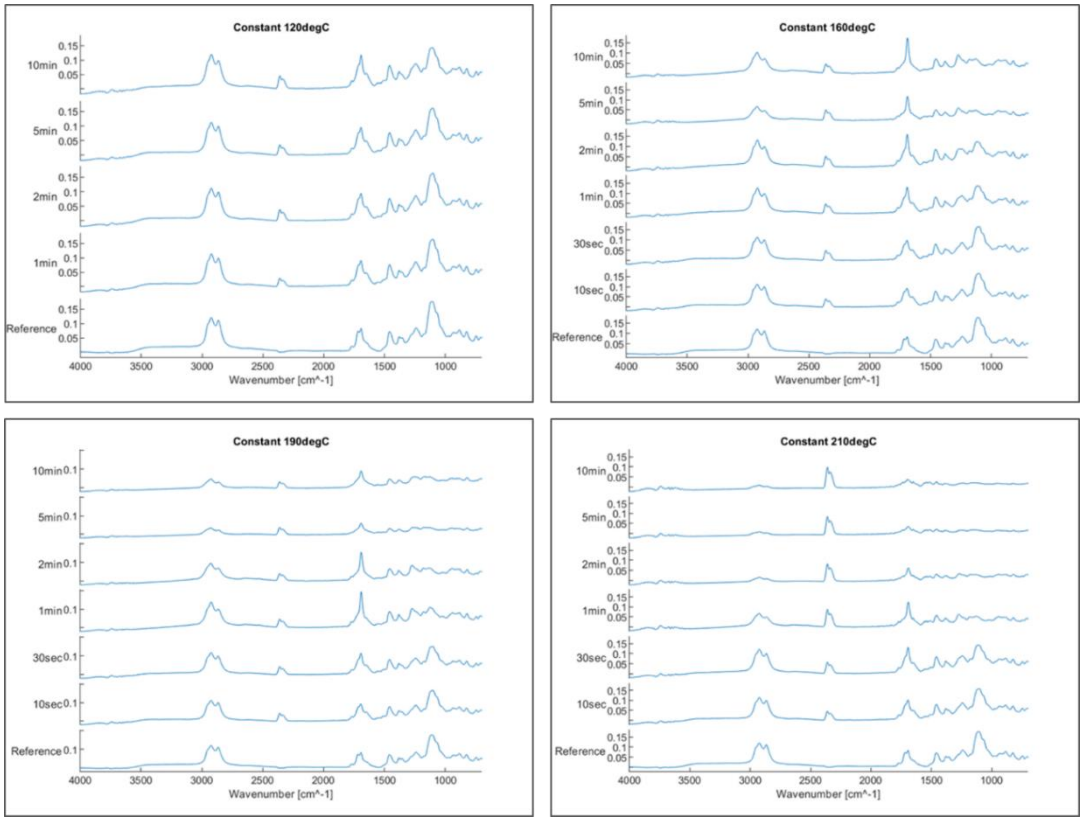

Figure 3-8: FTIR spectrum graphs of the samples from the mass loss study of TACFlux 007.

Figure 3-8 shows a gradual formation of peaks in the spectrum bandwidth of wavenumbers between 2200 cm^{-1} and 2500 cm^{-1}. Peaks in this area are correlated with carbon contamination, and characteristic CO_2 bandwidth and peak shapes. This implies an evolving amount of flux burn-out is present as a function of temperature at each holding time. In addition, with increased observed crystallinity and stickiness of the samples, the peaks around 1692 cm^{-1} exhibited increasing and narrowing absorbance magnitude, while the two peaks around 2900 cm^{-1} exhibited decreasing magnitude. In addition, the signal magnitude decreased in the alcohol frequency band

between 3100-3550 cm^{-1} with both heating temperature and heating time. Reduction of the total signal for the higher temperatures and longer holding time is correlated to an overall reduction in organic material. This implies that only flux residue is present at these temperatures and times.

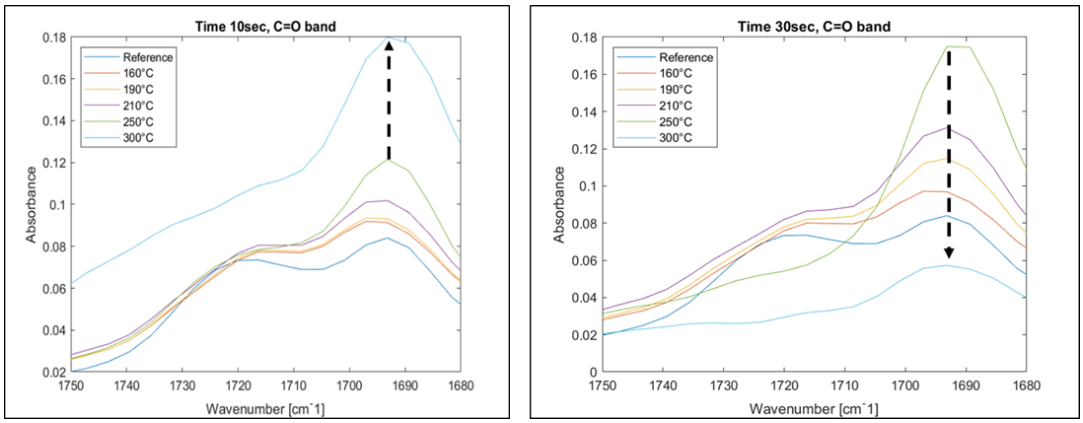

Figure 3-9: Superimposed FTIR spectrums (C=O band) of multiple heating temperatures at constant heating times of 10 seconds (left), and 30 seconds (right).

Figure 3-9 provides more information on the peak dynamics within the specific IR spectra of the C=O region. The figure superimposes the FTIR curves of multiple samples that were subject to different heating temperatures at constant times of ten seconds (left), and 30 seconds (right). These two constant heating times were chosen based on their significance to additive manufacturing capabilities. The peak growth between 1690-1700 cm^{-1}, in the first 10 seconds of each heating temperature has several possible explanations. First, the 1690-1700 cm^{-1} peak is a characteristic peak for aldehyde functional groups. Aldehyde functional groups often form when alcohols lose their hydrogen, contributing it to a carbonyl group to form a -CHO structure. As mentioned earlier, the signal decreases with heating temperature or heating time in the

alcohol frequency band between 3100-3550 cm^{-1}. A second contribution to the rise in the peak amplitude within the C=O region in the first 10 seconds in Figure 3-9 (left) is increased cross linking of the molecules in this region, which was also identified qualitatively as samples that exhibited an increased perceived crystallinity. An additional reason for the rise in peak amplitude could be the increased activity of the activator components at higher temperatures within the multi-component flux system. However, due to the unknown specific chemical composition of the flux, support for this contribution requires further analysis. In Figure 3-9 (right), after the flux is heated for 30 seconds at 250˚C, the peak in 1692 cm^{-1} starts to flatten, and at 300˚C, the signal is almost entirely gone. This is a strong indication that at elevated temperatures above 250˚C, the flux is degrading in very short times. Thus, this degradation must be matched to the activation temperature and activation kinetics to ensure that the activators do not degrade prior to completing their intended function, and to ensure that enough flux is evaporated in a timely manner. Another identification that rises from the band between 1680-1720 cm^{-1} is the presence of conjugated carboxylic acids. While the samples were tested without the metal system, the rise of peaks around this frequency might also imply activity of the activators that are present in the flux multi-component system.

3.4.5 SEM and EDS Initial Observations

Following the weight loss analysis of the flux, a study of paste microstructural evolution was conducted at the same temperatures and holding times used in the weight

loss study. Ag80In20 paste formulated with 500 mesh indium, and 325 mesh silver in TACFlux007 at 91% metal loading was deposited on copper sheets for in-situ evaluation. The use of thin copper sheets was to reduce the effect of heat transfer times, and to achieve an instantaneous heating effect. The samples were placed on a hot plate that was pre-heated for the same reason. Polyimide tape was attached to the samples to achieve fast and clean removal of the samples from the hot plate. This allowed for accurate heating times. After heating the samples, the samples were observed under the optical microscope, ESEM, and EDX.

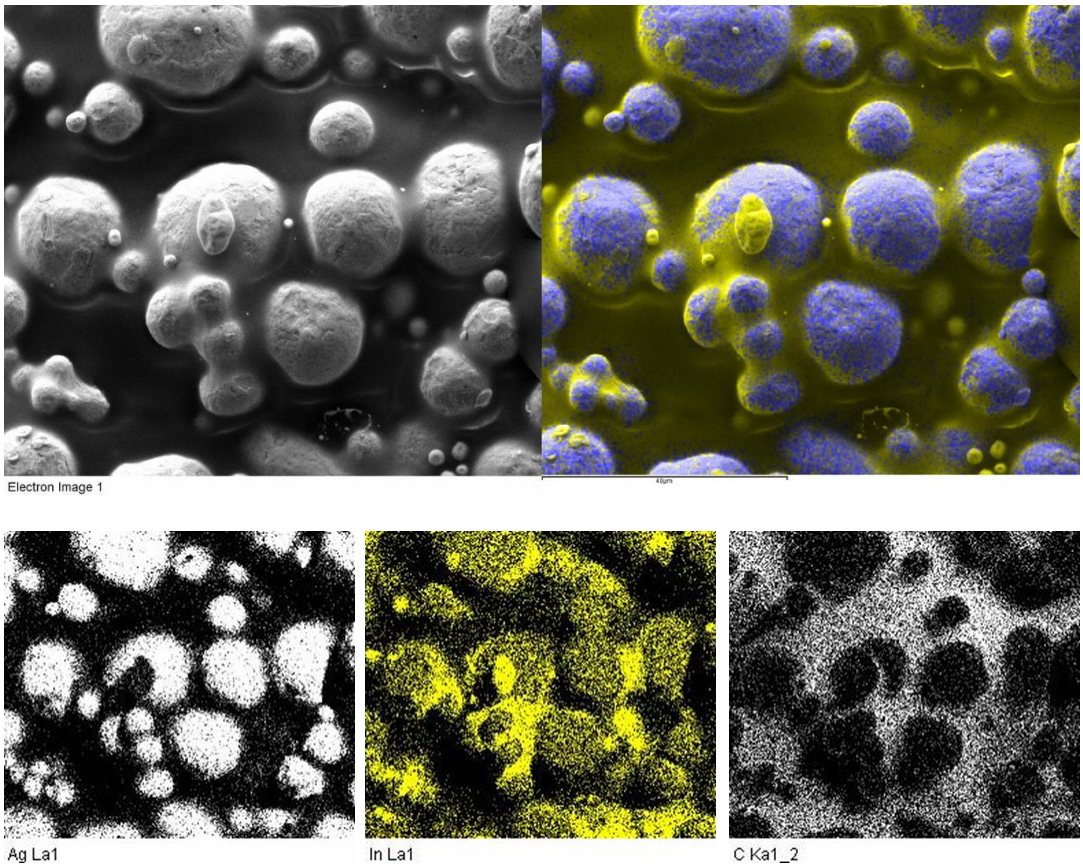

Figure 3-10: EDX monitoring of the top surface of a printed surface that was subject to 160˚C heating for 10 seconds.

Figure 3-10 shows the top surface of a printed sample that was heated at 160˚C for 10 seconds. The figure shows that indium-melt liquid bridges (yellow) between the solid-state Ag particles (purple) are present in multiple locations despite the short heating time, the relatively low heating temperature, and the presence of the metal particles within the flux binder. The figure also shows that while some indium melted and wetted the Ag particles, some indium particles were still present in their sphere configuration. It is highly important to monitor the wetting angle of the indium on the Ag spheres, as well as the amount of liquid-melt present at a given time, as it determines the ability of the structure to further densify after the flux removal. In addition, the individual X-ray dot maps in Figure 3-10 shows that the liquid metal bridge is forming when carbon is still covering the liquid metal. This suggests that the formation of a structure is initiating prior to sufficient removal of the flux binder, which may hinder the ability of the liquid-base capillary force to attract the silver particles towards each other.

Figure 3-11 shows the effect of heating a sample that went through an initial low-temperature densification, and then was subject to 300˚C heating for one minute on a pre-heated hot plate. The low temperature densification was achieved at temperatures below 100˚C to ensure that the indium does not melt or react with other particles. The figure shows that even though the sample had a good initial densified structure, the sample still suffers from relatively large pores. These pores are most likely due to the evaporation of the left-over flux. In addition, the printed structure is

beginning to “freeze” only one minute into the sintering process. Based on previous cross sections analysis, this structure “freeze” has a direct impact on the final sintered structure. This figure supplies further evidence of the importance of controlling and optimizing the early stages of the TLPS process.

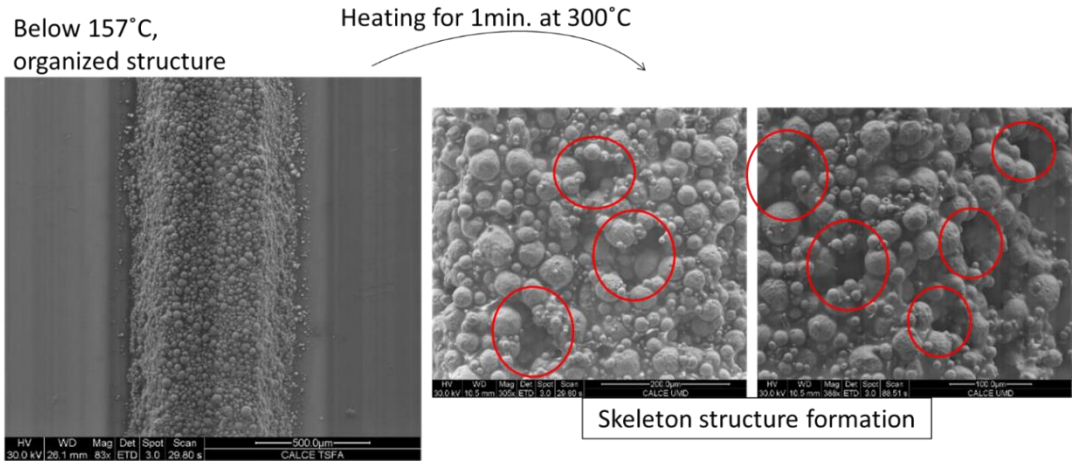

Figure 3-11: Shows the sample that went through an initial low-temperature densification, and then was subject to one-minute heating at 300˚C.

3.5 Statement of Work

Based on the preliminary work, the research and development of the TLPS material for robust additive manufacturing should prioritize the first stage of processing. This stage necessitates the decoupling of multiple cross-effects and a deeper understanding of the mechanisms occurring at short times and across a wide range of temperatures.

One major concern in this study was the electrical conductivity of the TLPS material. To address this, it was crucial to comprehend the development path of the material's electrical characteristics, their occurrence temperatures, and the rate at which

they develop. Achieving clarity on these aspects could pave the way for standardizing the manufacturing of TLPS materials for robust and rapid additive manufacturing.

To examine the formation of the TLPS material during different processing stages, in-situ electrical measurements were proposed. Up to this point, electrical measurements were only taken after more than one hour of sintering procedure, leaving little evidence of early-stage processing. Conducting in-situ electrical tests became necessary to fill this gap.

However, conducting in-situ electrical conductivity experiments required appropriate equipment. Thus, chapter 4 focuses on developing the necessary test equipment. In chapter 5, the results of the in-situ electrical testing are presented along with other complementary tests and measurements, and the chapter further analyzes the obtained results. In chapter 6, a simulation framework is established to further investigate and analyze the experimental findings. Finally, chapter 7 concludes the work and provides suggestions for future research directions.

4 APPARATUS AND TESTING EQUIPMENT

The previous chapters have highlighted the significance of understanding the early-stage processing of TLPS material and its electrical conductivity behavior. Traditional electrical measurements, conducted only after full processing procedure of sintering, provided limited insights into the critical initial stages of processing. To gain a comprehensive understanding of the material's electrical characteristics and their development, it became evident that in-situ electrical measurements were necessary.

The motivation behind conducting in-situ electrical tests was twofold. Firstly, to capture real-time data during the early stages of processing, enabling the observation of the dynamic changes in electrical properties as the TLPS material evolves. Secondly, the introduction of in-situ measurements aims to identify the specific factors influencing the electrical behavior of the TLPS material during the initial stages of processing. These factors may include change in heating rates, chemical reactions, phase changes, and microstructural transformations, which play a crucial role in determining the material's final properties. By understanding these influential factors, this work hope to tailor the manufacturing process for optimized performance and consistency.

4.1 In-situ Electrical Testing Apparatus

In the in-situ electrical conductivity experiment, there are three main components: the heating medium, the tested samples, and the probing set-up. The combination of these three components determines the feasibility, and the quality of

the experiment, the measurements, and the final results. The following sections will discuss the design choices, material selection, objectives, constraints, integration techniques, and software and hardware development.

4.1.1 Hot Plate Design, Objectives, and Manufacturing

The choice to use a hot plate as the heating medium for in-situ resistivity measurements was driven by the need for straightforward and accessible probe access. Conducting the resistivity tests outside of an oven or a muffle furnace was selected to maintain the independence of multiple material types from the experiment's heating conditions. This flexibility in material selection is essential for rapidly designing the fixture for the probe, ensuring its success and efficiency.

Once the heating medium, the hot plate, was selected, the focus was on rapid progress. Before manufacturing a custom-made hot plate, multiple hot plates available in the labs were tested. Among these, passive ceramic-based hot plates were limited to selecting temperature set points, hindering the experiment's design capabilities. Basic IR-gun measurements of the ceramic hot plates revealed uneven heating, especially when dealing with large specimens compared to the hot plate's dimensions. Consequently, this uneven heating introduced higher noise levels in the measurements of the desired design variable, impacting data accuracy. In addition to the ceramic-based hot plates, the labs had an aluminum-based hot plate with a control unit for designing a temperature profile. The first stencil was designed with consideration of this hot plate's dimensions. However, during testing, the hot plate's temperature

feedback proved unreliable, failing to meet the required levels of reliability for the electrical in-situ experiment. As a result, alternative solutions were explored to ensure precise and dependable measurements.

Upon rejecting all the available options of hot plates already exist in the laboratories, the next step was to design a custom-made hot plate. The first step in designing the custom-made hot plate was to define a list of requirements and objectives. There were three main requirements: first, the hot plate must have reliable temperature feedbacks. These temperature feedbacks are crucial to the hot plate's control performance, the synchronization of the test signals, and the quality of the experiment itself. Second, the hot plate dimensions must match, or at least fit the dimensions of the testing ceramic boards. This requirement is crucial when trying to heat and cool the ceramic boards without generating any uneven stresses in these boards. These uneven stresses can crack the boards and terminate the experiment unsuccessfully. Third, the heating and the cooling system of the samples must be uniform. Non-uniform heating and cooling can lead in diffusion variabilities that can affect the results of the measurement. In addition, similar to the ceramic boards, when non-uniformly cooled, the TLPS samples can also cracked and snap, which can lead to a falsified cross-section analysis.

After considering and rejecting all available options of hot plates already present in the laboratories, the subsequent course of action involved designing a

custom-made hot plate. Defining a set of requirements and objectives marked the initial step in this process. Three primary requirements were identified:

- **Reliable Temperature Feedback:** The hot plate must incorporate dependable temperature feedback signals. The feedback loop is critical for ensuring precise control performance of the hot plate, synchronizing the test signals accurately, and maintaining the overall experimental quality.
- **Matching Dimensions:** The hot plate's dimensions must align with, or at least fit, the dimensions of the testing ceramic boards. This alignment is essential to ensure even heating and cooling of the ceramic boards, thereby preventing the generation of uneven stresses. Uneven stresses can lead to cracking of the boards, which could result in a premature termination of the experiment.
- **Uniform Heating and Cooling:** The heating and cooling system for the samples must exhibit uniformity. Non-uniform heating and cooling can introduce diffusion variabilities that may impact the accuracy of the measurement results. Additionally, similar to the ceramic boards themselves, non-uniform cooling of the TLPS samples can lead to their cracking and snapping, potentially leading to a distorted cross-section analysis.

By adhering to these requirements, the design of the custom-made hot plate aimed to overcome the limitations encountered with existing options and facilitate accurate and reliable in-situ resistivity measurements during the TLPS material processing.

In terms of the design objective of a hot plate, the design must encompass several essential features. The hot plate must be well-insulated to prevent thermal leakages and ensure efficient heating and cooling processes. Additionally, the design should facilitate easy and numerically efficient calculations, streamlining the development process. Rapid heating and cooling capabilities are crucial to achieve time-efficient experiments. The hot plate's modular design must be adaptable to fit within the glove box setup (Figure 4-1), ensuring seamless integration into the experimental environment. Cost-effectiveness is also a key consideration, aiming to achieve the desired functionality without exceeding the allocated budget. Furthermore, the hot plate should offer flexible control options for both heating and cooling processes, allowing precise adjustments as needed. Finally, incorporating safety features in both software and hardware is paramount to ensure the protection of the equipment and researchers during experimentation.

Figure 4-2 displays the proposed schematics of the hot plate's design which is inspired by Hanes's hot plate design [152]. Both designs utilize aluminum as the base material and implement heating elements below the cooling level. However, the proposed design includes an additional close-to-surface temperature measurement level. The need for this extra sensing level arises from the requirement to calibrate experiments based on specific temperature choices and obtain the most reliable temperature readings of the samples during the experiments.

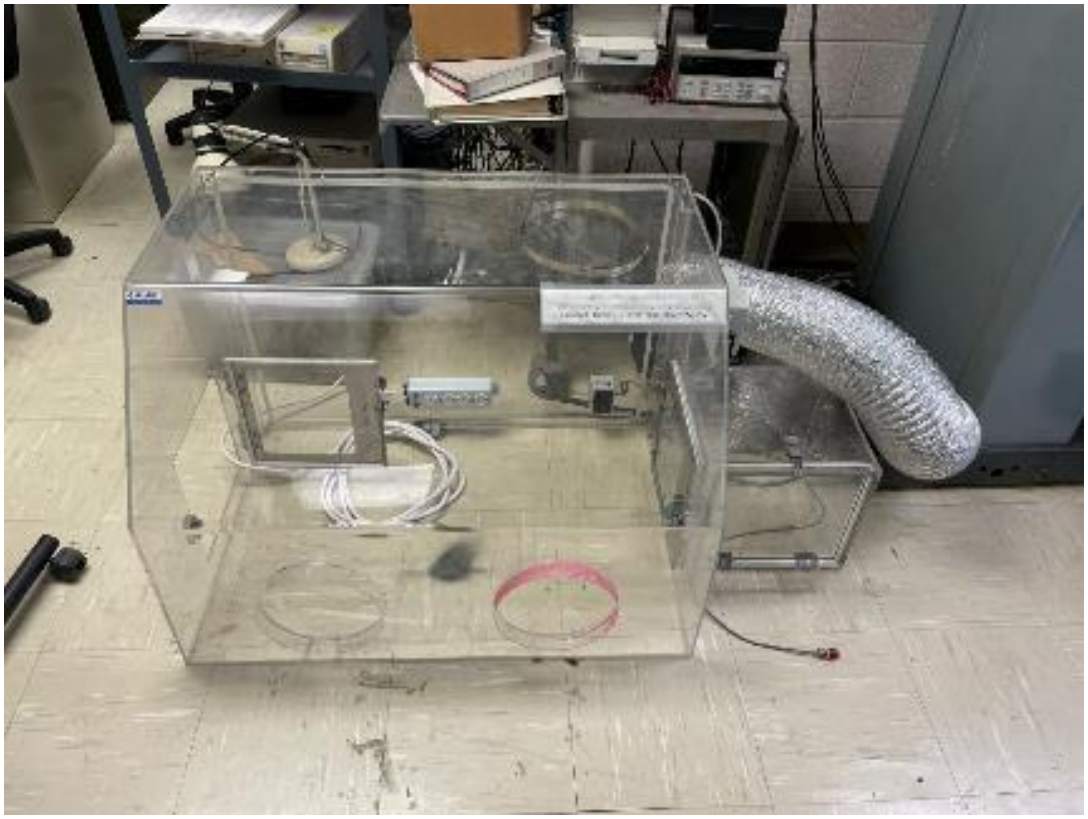

Figure 4-1: Glove box for humidity-controlled in-situ electrical experiments and PML experiments.

The calibration temperature choice at the start of an experiment should be sufficiently above the cooling water temperature and low enough to minimize chemical interactions, such as the diffusion of indium particles at low temperatures [78]. Although embedding the temperature sensors inside the hot plate does not provide direct measurements of the samples during the experiment, it ensures highly reliable and consistent temperature readings. This, in turn, confirms the uniformity of the surface temperature and increases confidence in the final measured design variables.

In future experiments, the surface temperature will also be verified using an IR temperature sensor directed at the ceramic test boards from above. This additional

independent IR device's measurement should work efficiently with the ceramic boards and assist in calculating the consistent temperature bias between the sample's temperature and the sensing level within the hot plate.

Furthermore, unlike Hanes's design, which features a single pair of input/output holes and an internal manifold for cooling, the proposed hot plate design incorporates multiple input/output holes. This design allows for even cooling and facilitates straightforward and efficient numerical calculations.

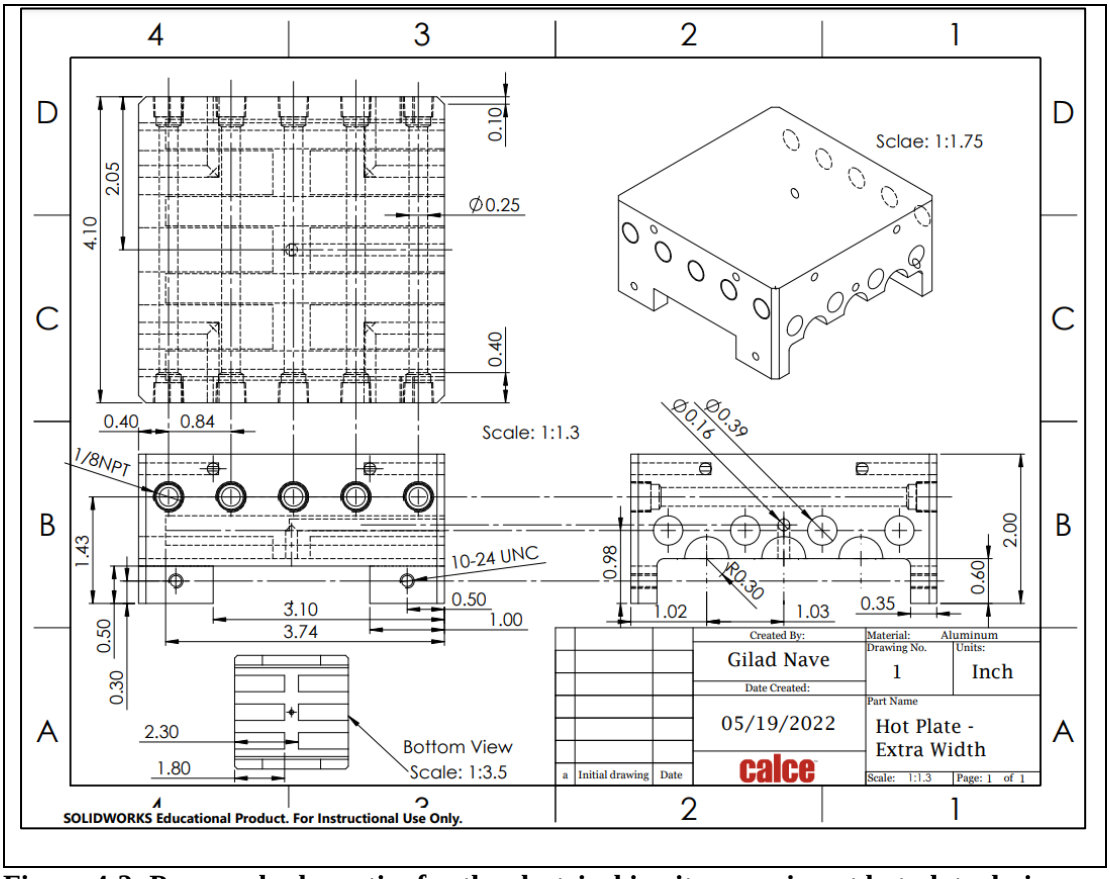

Figure 4-2: Proposed schematics for the electrical in-situ experiment hot plate design.

`

Figure 4-3 presents a detailed depiction of the locations of the thermocouples, their securing screws, and the heating elements within the hot plate design. The close-to-surface thermocouples are positioned one inch away from each surface's edge, allowing for quarterly measurements near the surface. These close-to-surface measurement locations serve to verify the temperature uniformity of the test samples during an experiment.

At the front of the hot plate, there are three thermocouple access locations that extend all the way to the middle of the hot plate. These embedded thermocouple locations provide highly reliable and consistent temperature measurements close to the heaters. Such measurements are crucial for the control design and quality of the experiment. Close-to-heater temperature feedback is essential to minimize signal delays in the control design and operation, ensuring efficient and accurate temperature regulation.

The hot plate is equipped with four 500W-AC heaters, strategically positioned to achieve uniform heating of the experiment's hot surface area. The uniform heating of the hot surface area has been confirmed through numerical simulations, ensuring reliable and consistent experimental conditions.

Figure 4-4 illustrates the main cooling and plumbing design configurations of the proposed hot plate. The hot plate is equipped with five cooling channels, with each channel having one pair of entrance and exit holes. The cooling fluid, typically water,

enters the hot plate from alternating directions. This cross-flow cooling configuration enhances both the uniform cooling of the hot plate and its cooling efficiency.

To ensure durability and efficiency, the input/output pipes are made of either stainless steel or copper. These pipes are also bent at ninety degrees to minimize space requirements and are connected to the hot plate using stainless steel NPT connections. This robust cooling and plumbing system is designed to effectively dissipate heat from the hot plate, maintaining its stable and controlled temperature during the experiments.

Figure 4-5 depicts the main integration schematics of the hot plate, encompassing the PC-based control block, the Arduino MEGA control board configuration, the electrical configuration, and the plumbing configuration. This schematic illustrates the interactions and interconnections between these configurations, facilitating a comprehensive understanding of the integrated system.

Additionally, the measured power requirement during full-power operation of the heaters and the pump is indicated in the integration schematics. Objects labeled as F1-F3 represent electrical trippers that have been implemented as safety features and serve as protection layers for other components within the hot plate. Ensuring user safety, the entire hardware assembly and the hot plate are electrically grounded. This integration design, as presented in Figure 4-5, demonstrates a well-organized and safety-conscious approach to harmonizing various components and controls within the hot plate, enabling precise and reliable temperature regulation during experiments.

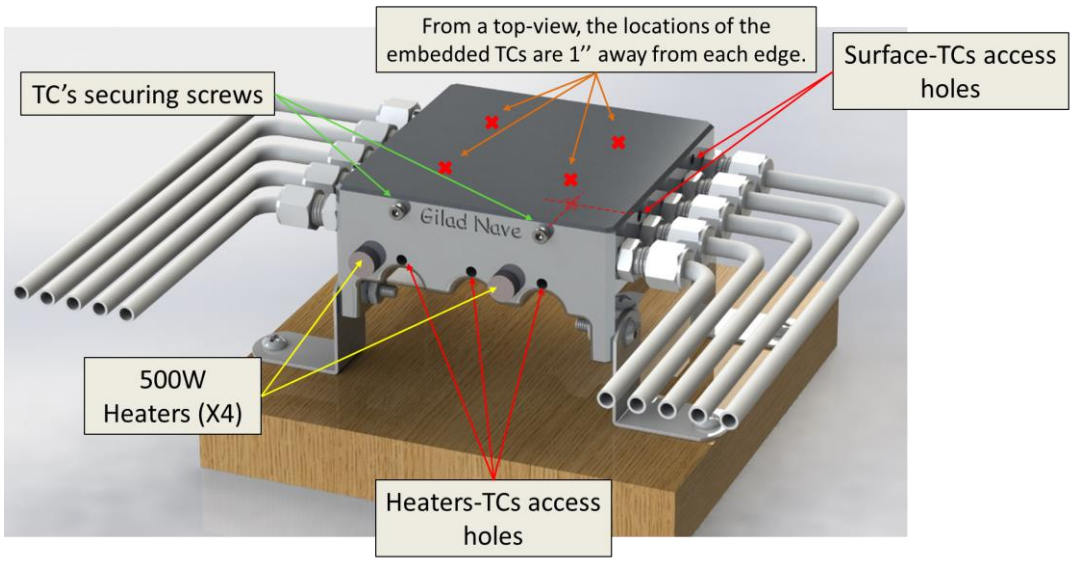

Figure 4-3: Locations of embedded thermocouples, heaters, and securing screws in the proposed hot plate design.

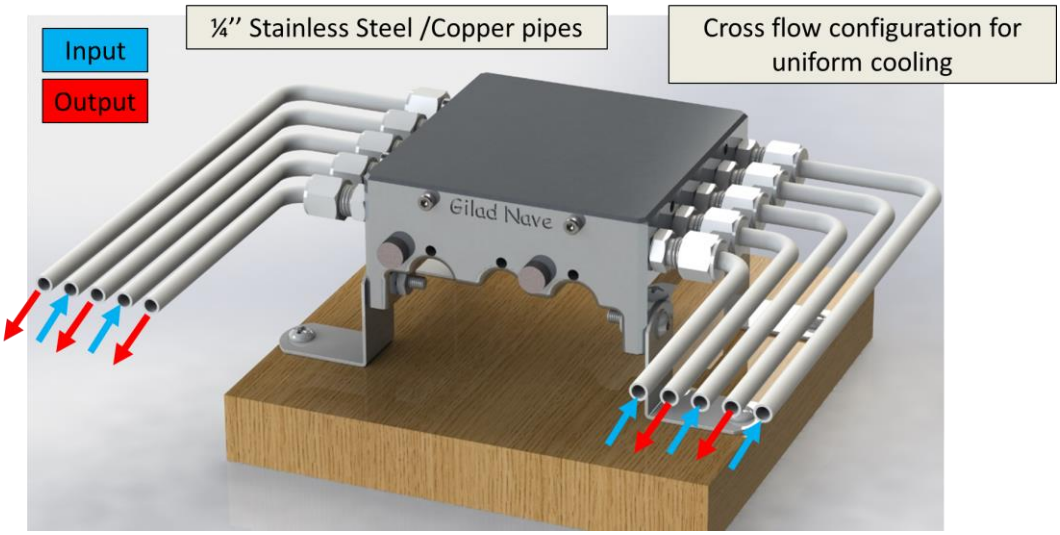

Figure 4-4: Liquid cooling channels and flow direction in the proposed hot plate design.

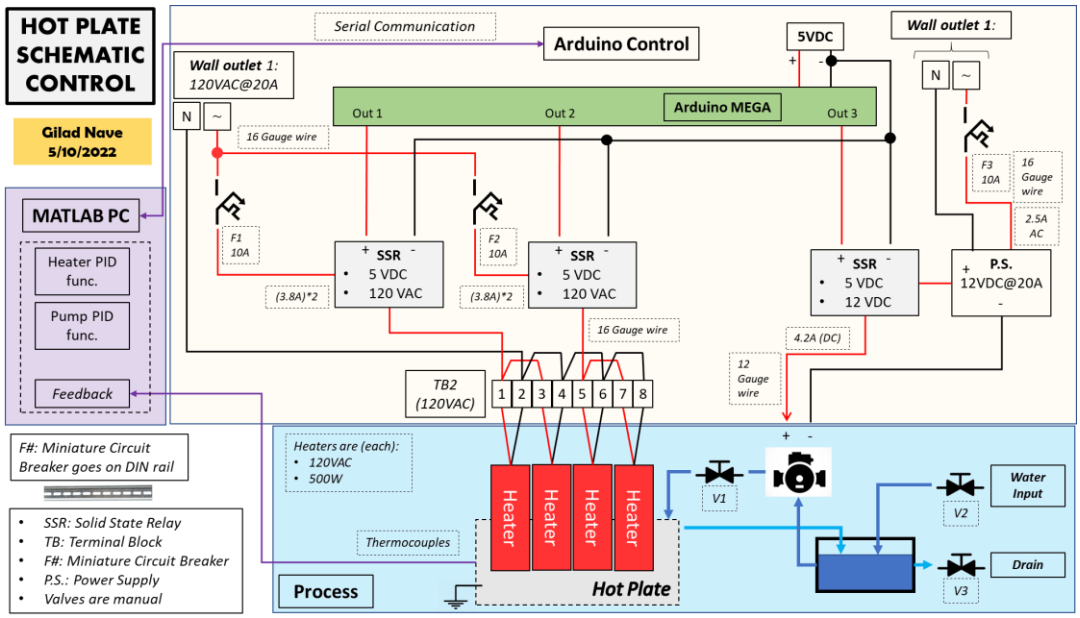

Figure 4-5: Control, electrical, and general schematics of the proposed hot plate design.

4.1.2 Stencil Design

The stencil and its design play crucial roles in conducting the in-situ electrical resistivity experiments efficiently. Firstly, the stencil determines both the sample's length and cross-sectional area, which are essential for resistivity calculations. Longer paste traces enhance measurement accuracy while reducing noise magnitude. Secondly, the quality of the stencil is vital for consistent paste deposition on ceramic boards. A well-designed stencil ensures successful and uniform paste application. Thirdly, the stencil's design should align with the available "real-estate" area during the experiment, determined by the ceramic board size and maximum heating area. Using this space optimally is crucial for experiment efficiency, as more paste traces per board lead to faster statistical data acquisition. Fourthly, the stencil should feature adequately sized pads that comfortably accommodate the testing probes. Lastly, for ease of

operation and to minimize potential damage to the soft printed paste, the stencil should incorporate a holding leaf. This leaf assists the user in carefully removing the stencil and efficiently bending it.

Figure 4-6 presents the initial iteration of the stencil prototype designed for in-situ electrical resistivity experiments. The stencil's outer perimeter aligns with the dimensions of the ceramic Alumina boards used in the study, measuring 4 inches by 4 inches. To optimize the paste application, the stencil incorporates six slots within the inner square (indicated by the dot-dashed square). This inner square matches the size of the pre-existing hot plate in the laboratory. The stencil design includes a bending leaf, facilitating ease of operation and efficient removal after paste deposition. Additionally, the pads for the probes measure 3mm by 3mm and maintain a distance of 10mm between each trace.

Figure 4-7 illustrates the second prototype of the stencil design employed in the in-situ electrical resistivity experiments. It is an extension of the original prototype, featuring larger pads to accommodate bigger probes. However, this design necessitated a different hot plate, with a larger heating area capable of accommodating the entire size of the printed paste traces, as the original lab's hot plate was not suitable for this purpose.

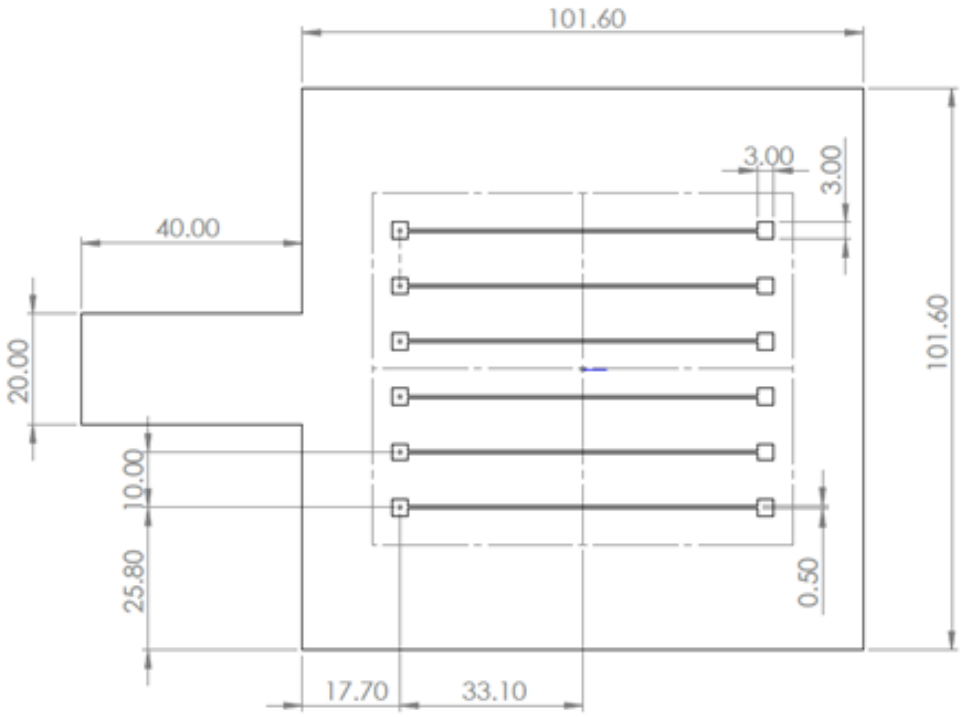

Figure 4-6: Initial prototype of the in-situ electrical resistivity experiment stencil's design.

Figure 4-8 displays the third and current prototype of the stencil design. The primary modification in this iteration pertains to the pads, which were adjusted to accommodate a recent prototype of the probes. Furthermore, the present stencil design incorporates two bending leaves, assisting the user in determining the optimal direction for stencil removal. The stencil possesses a thickness of 8 mil (0.008 inches) and is constructed using laser-cut stainless steel. The stencil's edges align precisely with those of the testing ceramic boards, enabling accurate and consistent positioning from one test to another.

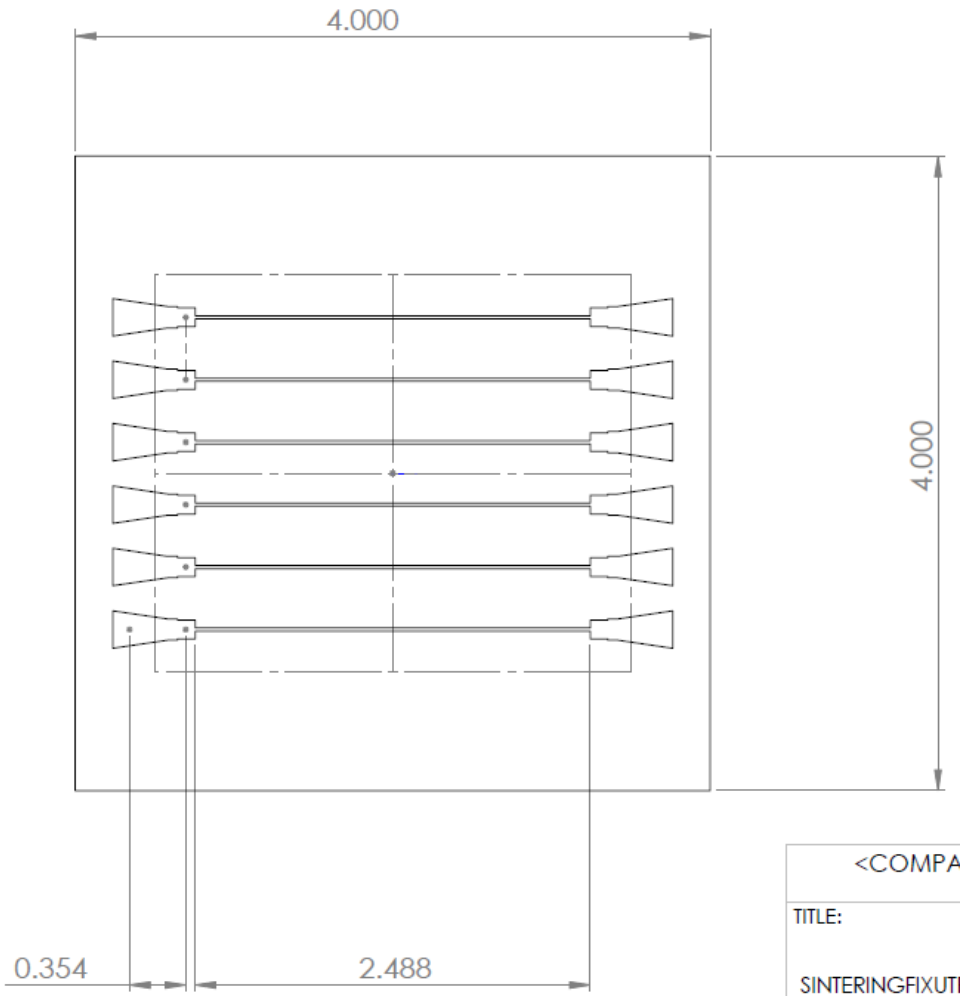

Figure 4-7: Second prototype of the in-situ electrical resistivity experiment stencil's design. The main change from the first prototype is in the pads design and size, that were enlarged to fit the different set of the 4-point probes.

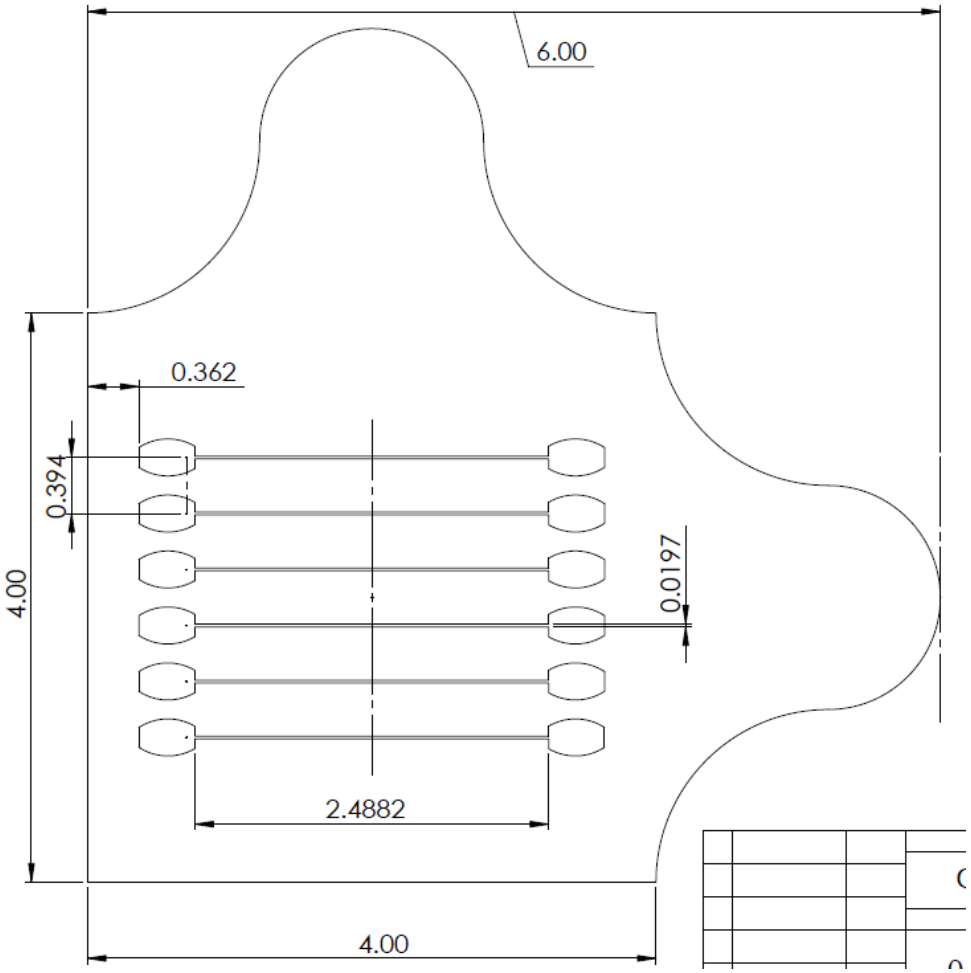

Figure 4-8: Third and current version of the in-situ electrical resistivity experiment stencil's design.

Figure 4-9 exhibits the set of test samples created using the third stencil prototype. The stencil removal process resulted in clean, repeatable, and accurately positioned test traces of the paste. For this experiment, recycled alumina boards from previous trials were employed. The recycling procedure involved cleaning the boards with isopropanol, followed by heating a stack of plates on a hot plate to a temperature of 540˚C for at least 15 minutes. This step ensured that previous marks were significantly evaporated and degraded.

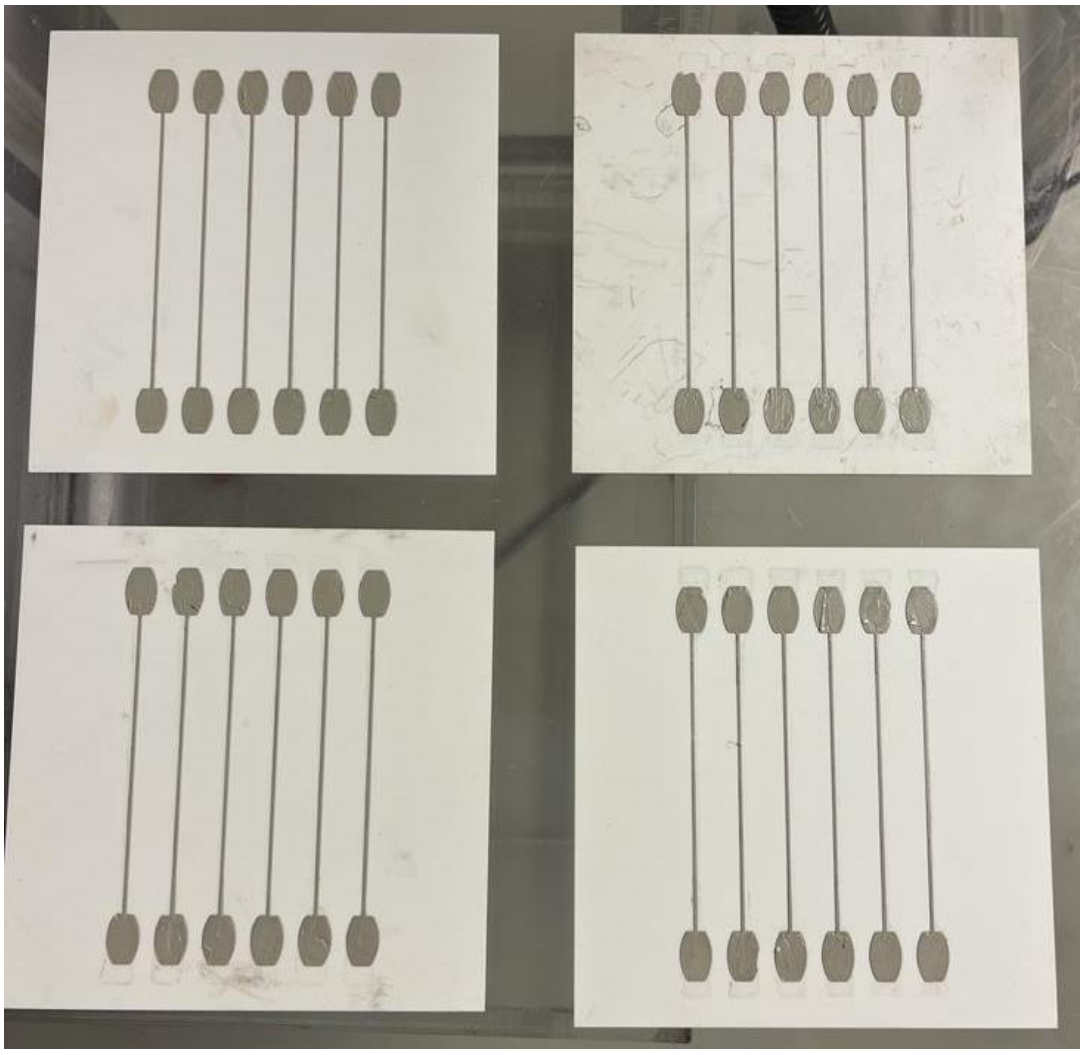

Figure 4-9: Stencil printed samples for the in-situ electrical experiment. Each alumina board features six TLPS samples. The samples feature constant length for resistivity calculations.

4.1.3 Probe Design

Resistance can be assessed using two primary configurations: the 2-wire and 4-wire setups. In the 2-wire configuration, the measurement involves recording the voltage drop across two points of materials or resistors. However, the use of a voltmeter in this method introduces theoretical infinite internal resistance, which ensures that the

test current stays on its intended path. Nonetheless, the 2-wire method is susceptible to parasitic noise caused by the internal resistance of the probing wires and multiple contact resistances involved in the measurement.

On the other hand, the 4-wire configuration offers a more accurate approach to measure resistance across two points. Figure 4-10 illustrates the 4-wire probing configuration. In this setup, the two outer probes act as the current source, while the two inner probes measure and sense the voltage drop. As previously explained, the voltmeter's measurement consumes an insignificant amount of current, resulting in the voltage drop between the two sensing probes being solely attributed to the material itself, without interference from probing resistance or other parasitic resistances like contact resistance. [161].

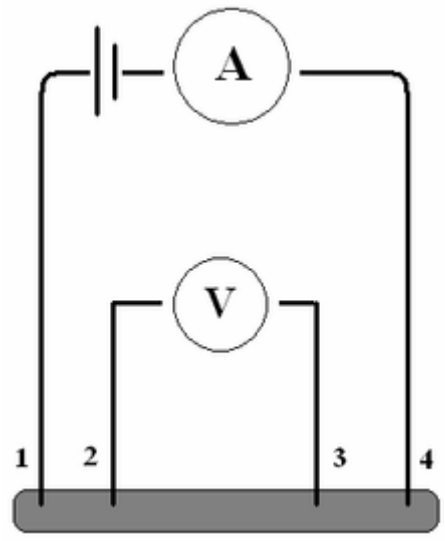

Figure 4-10: Schematics of 4-point probe resistance test. Probes #1 and #4 supply the test current, and proves #2 and #3 sense the voltage drop. This 4-point design eliminates contact, and wire resistances.

Before conducting each in-situ electrical measurement for all probing configurations and prototypes, the probes underwent logarithmic calibration against known resistors. The initial prototype of the 4-wire probing design is depicted in Figure 4-11. Each probe is constructed using 30-gauge copper wire, which is then enveloped with Kepton (Polyimide) tape to provide both electrical and thermal insulation. Copper was chosen for its exceptional electrical properties. To form each pair of Source-Sense probes, they were wrapped together with an additional layer of Kepton tape and connected at the tip area.

It is important to note that the contact between the two individual probes can introduce resistance errors. The magnitude of this error increases with the length of the contact point between the probes. However, thanks to the outstanding electrical properties of the copper wires, this error was effectively minimized and proved to be insignificant even at resistance levels as low as milliohms.

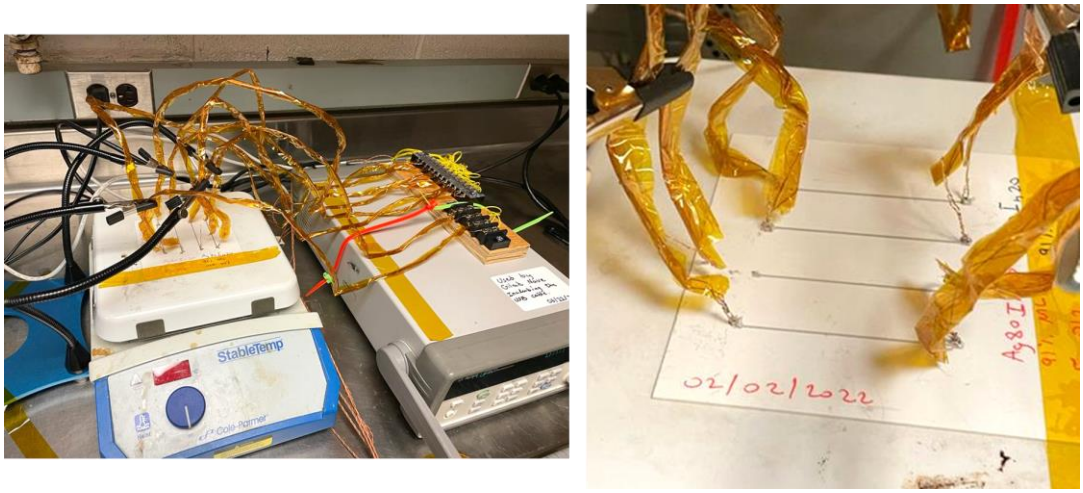

Figure 4-11: Initial prototype of in-situ electrical test probe design and configuration.

The probing design shown in Figure 4-11 demonstrated satisfactory and consistent readings. However, the limited size of the paste-pads posed a challenge in establishing reliable contact between the probes and the paste-pads. Moreover, the process of changing testing boards was relatively slow, as each pair of Source-Sense probes needed individual positioning.

During the initial probe prototype usage, a laboratory hot plate was employed, which could only be set to a specific temperature and lacked cooling capabilities. This absence of cooling prolonged the time between experiments and prevented timely termination of a given in-situ electrical resistivity experiment.

Furthermore, the copper probes exhibited reactivity with the TLPS paste, leading to the adhesion of solid paste fragments onto the probes. Given the small and delicate nature of the 30-gauge probes, it proved challenging, and sometimes impossible, to completely clean the probes between successive test runs.

Following the first prototype of the in-situ electrical test probes, it became evident that the next generation of prototypes must possess higher levels of structural rigidity. This enhanced rigidity is intended to improve testing throughput and eliminate the need for individual adjustments of the probes against the paste-pads. Figure 4-12 illustrates a proposed method and design to achieve this additional structural rigidity.

The proposed design introduces an insulating set of probe plates (indicated in red) that firmly hold the testing probes in a rigid and fixed position. These probe plates are connected via four rods to a thermal and electrical insulating top-plate. The top-

plate, in turn, is linked to an adjustable rigid crane, capable of vertical translation. The crane arms also serve as a base for the electrical wire terminals.

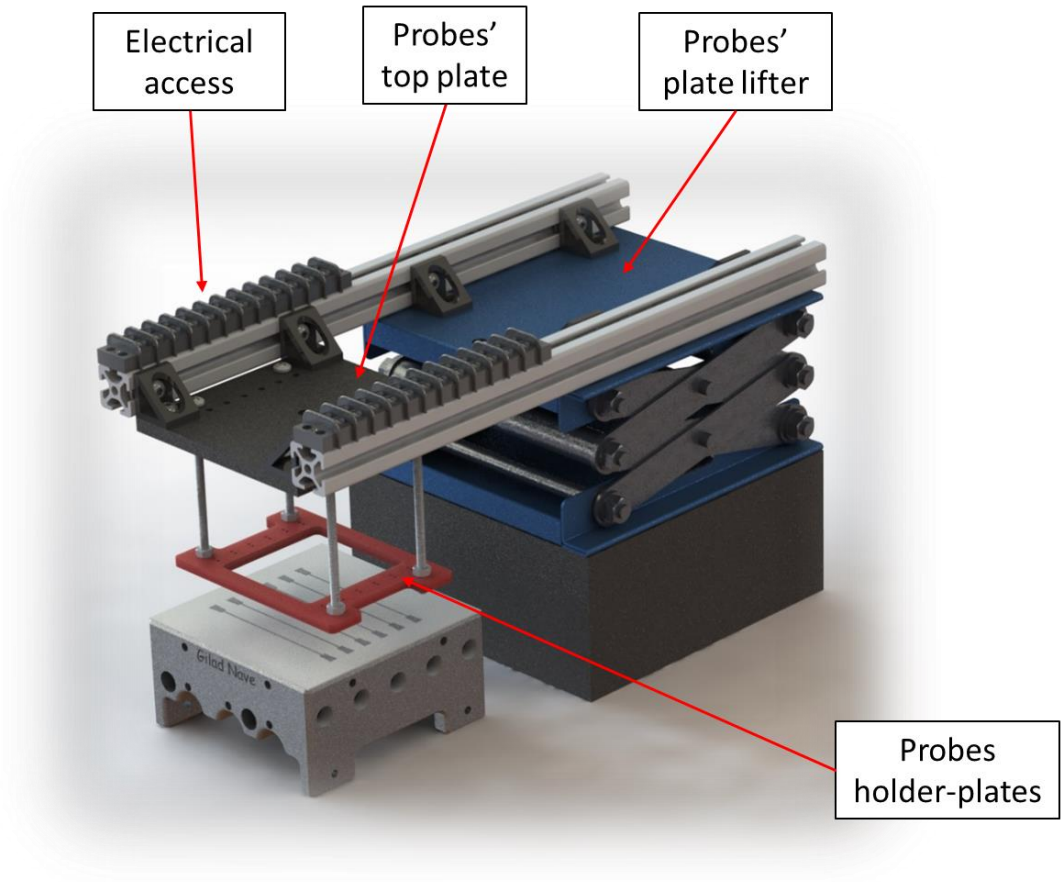

Figure 4-12: Proposed design for rigid in-situ electrical test probe holder configuration.

The second prototype of the probes for in-situ electrical tests utilized the proposed design with increased structural rigidity, as shown in Figure 4-13. The probes were advanced towards the testing location through access rods. As mentioned earlier, these access rods were connected to a thermally and electrically insulated top-plate

crafted from Delrin polymer (Polyoxymethylene). The top-plate, in turn, was linked to the crane arms and had the capacity for vertical movement.

In Figure 4-13, the second prototype of the probes for the in-situ electrical tests was constructed from aluminum leads. The leads were manufactured using water-jet to but them from a thin aluminum sheet. The use of aluminum proved beneficial as it prevented reactions between the probes and the paste, thereby expediting the preparation time for each individual test run. Additionally, the structural configuration of the probes was designed to offer spring-like characteristics, which likely contributed to their flexibility and adaptability during testing.

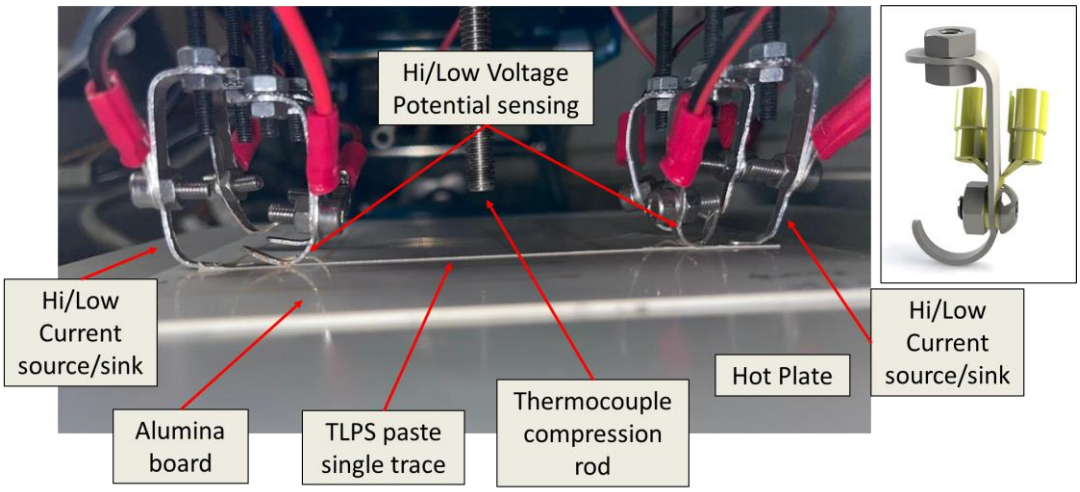

Figure 4-13: Second prototype of the probe design for the in-situ electrical test. The second prototype features hour aluminum probes.

The third and current prototype of the probe design for in-situ electrical tests represents a significant departure from the second prototype. While the second prototype aimed to avoid any reaction between the probe heads and the paste-pads, the

current design deliberately encourages such a reaction. This shift in philosophy is driven by two key reasons.

Firstly, allowing a reaction between the probes and the paste ensures an optimal electrical connection and minimizes noise from contact resistances. This enhanced electrical connection contributes to a stable and reliable signal during the in-situ electrical experiment.

Secondly, since the probes are now intended to react with the paste, it was deemed crucial to make it easy and cost-effective to replace the probe heads when needed. The third and current design, presented in Figure 4-14, addresses this change in testing philosophy through the use of Pogo-Pin probes.

The Pogo-Pin probes consist of two parts. The first part is a stationary socket, which is soldered to the electrical wires to provide reliable and consistent electrical contacts. The soldered connections are protected and insulated with pieces of heat-shrink plastic. The socket part of the probe is held stationary by top and bottom thermally and electrically insulating fiber glass board plates.

The second part of the Pogo-Pins incorporates an internal spring and is press-fitted into the stationary socket part. The probe's head, typically made of stainless steel coated with an electrical element (e.g., Sn, Ni, etc.), utilizes the stainless-steel core for a robust structural design, thereby extending the probe's lifespan.

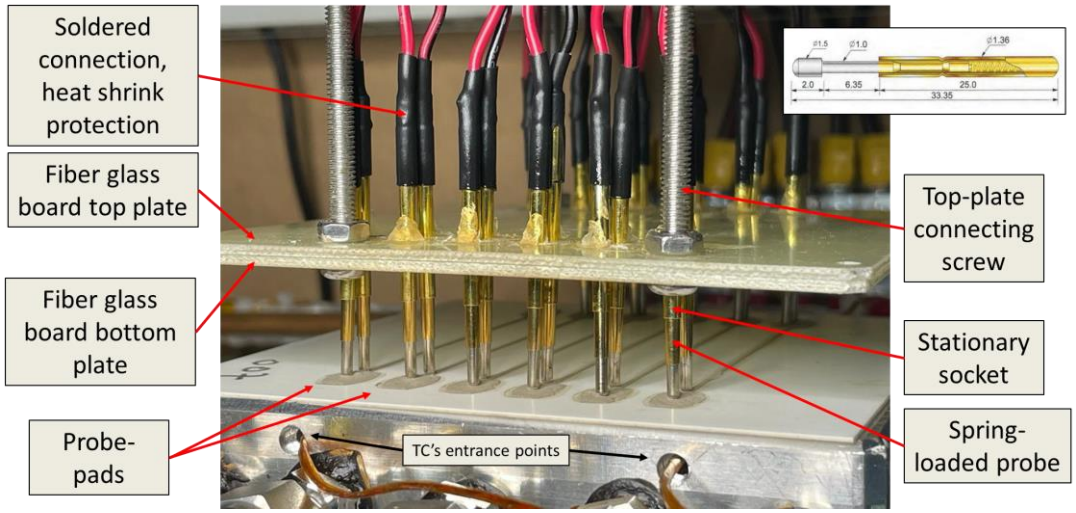

Figure 4-14: Current prototype of the probes configuration for the in-situ electrical tests. The current configuration utilizes spring loaded Pogo-pins that allow for efficient, fast, reliable, and accurate measurement.

Figure 4-15: The figure shows the compressed-state of the current probe configuration. The compressed state supplies cumulative downward force against the alumina board that improves the heat transfer from the hot-plate.

As shown in Figure 4-15, the utilization of spring-based probes in the third and current design offers an additional advantage by exerting cumulative downward force

on the ceramic alumina board. This force enhances the thermal contact between the hot plate and the testing ceramic alumina board, leading to improved heat transfer efficiency.

The figure also illustrates the insulation sleeves enveloping the copper pipes and insulation pads placed at each of the hot plate's legs. These features serve the purpose of minimizing thermal leakage from the hot plate to the modular aluminum-frame of the experiment's apparatus. By effectively insulating these elements, the thermal integrity of the experiment is preserved, contributing to accurate and consistent measurements.

4.1.4 Control Schemes

In order to design an effective temperature profile for a given experiment or specific thermal-processing requirements, a control system for the hot plate is essential. The control system should possess the capability to maintain stable set-point temperatures and control the rate of cooling and heating.

The initial step in establishing the control system involves mathematically identifying the transfer function of the process. Figure 4-16 displays a typical work environment of the System Identification app provided by Matlab. Unlike white or gray-box methods, which derive the transfer function using known system models, the Matlab System Identification app employs a black-box method to mathematically determine the transfer function. This application necessitates a set of inputs and outputs that were measured using an open-loop control scheme configuration.

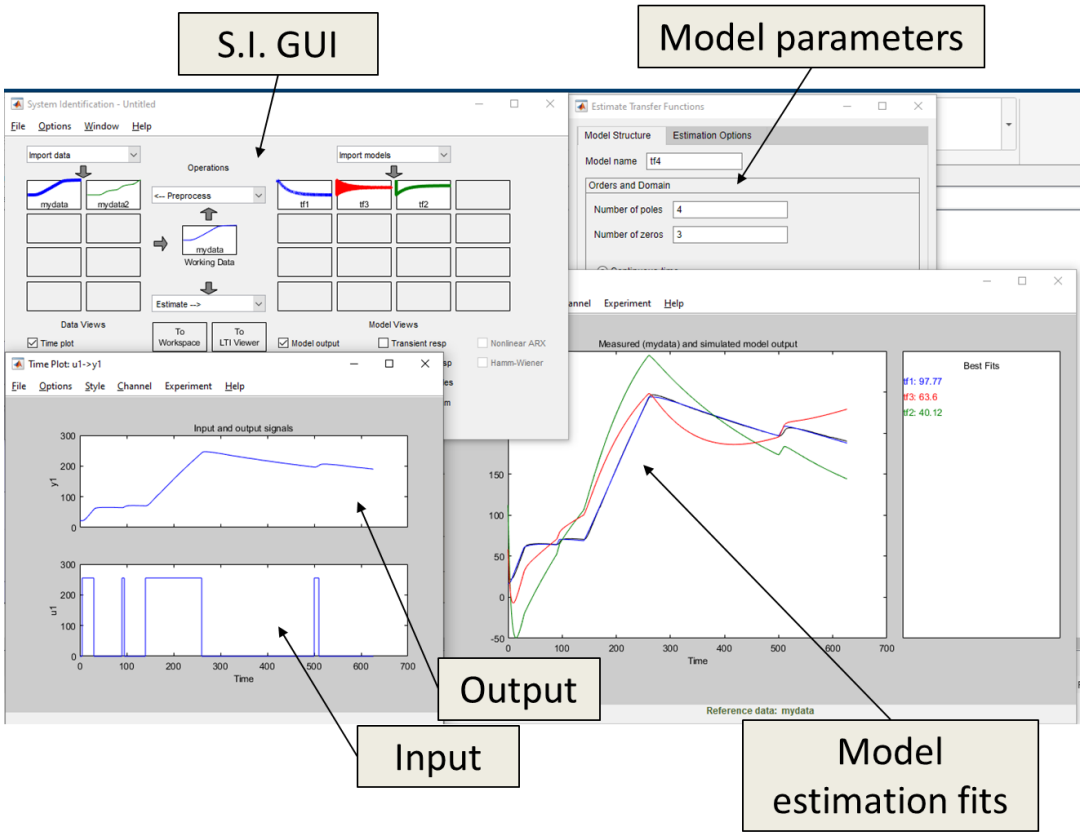

Figure 4-16: Typical work environment of the System Identification application.

The input and output signals must maintain consistent time intervals and scanning frequency. To enhance the quality of the input-output relationship, it is preferable to measure the output with minimal physical delays, such as measuring the temperature far from the heating elements. The System Identification app also requires a minimum of two sets of input-output measured data. The first set is used to calculate and estimate the transfer function, while the second set is employed to validate the resultant transfer function of the system. Figure 4-17 illustrates the validation curve fit of the resultant transfer function obtained from the System Identification app. The

validation curve exhibits an 87.3 percent fit to the measured output signal, which was deemed sufficient to proceed with the development of the control system.

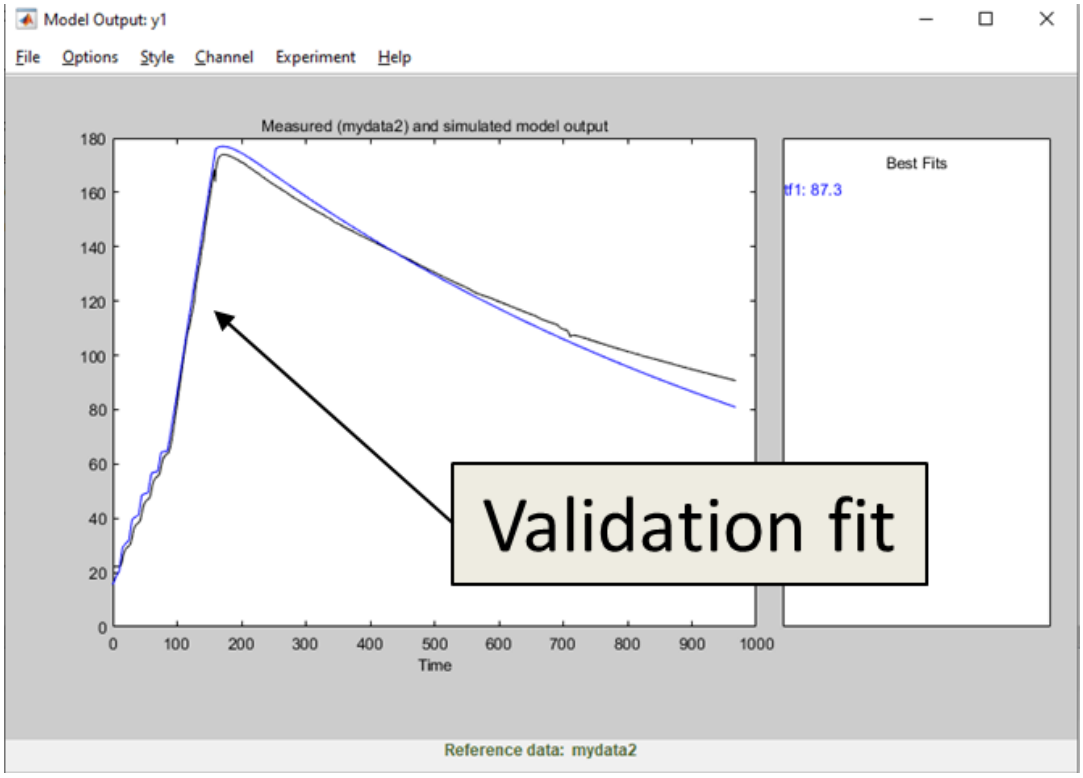

Figure 4-17: Validation curve fit of the resultant transfer function that was obtained from the System Identification app.

Figure 4-18 showcases the Simulink (Matlab) environment designed for the hot plate's control system design and tuning. Unlike the scripted environment in Matlab, Simulink offers a block-based control design, where different groups of blocks can be activated at any given time. The workflow in Figure 4-18 commences from the Data Acquisition Block, responsible for obtaining temperature measurements with consistent time intervals, which can later be fed into the System Identification app for transfer function estimation.

Upon obtaining the system's transfer function, the workflow returns to the Simulink environment under the Simulation Block. Here, the transfer function is implemented into a basic closed-loop control configuration, including an untuned PID controller, as seen in Figure 4-18 from the bottom right. The initial PID tuning is performed using the PID Tuner app, followed by multiple simulations in the Simulation Block to manually tweak the PID parameters until the desired performance is achieved.

Subsequently, the workflow moves to the Real Live-Control Block, where the control system actively engages the real physical system, namely the heaters in the hot plate. In this block, the output PID signal is converted into Pulse Width Modulation (PWM) signals. These PWM signals activate corresponding DC-AC optocoupler zero-crossing Solid-State Relays (SSRs). Upon activation, the SSRs open the gate to the 120Hz AC sinusoidal signal from the wall. The PWM signal allows controlling the gate-opening based on the frequency-based pulse width of the SSR signal. This action effectively regulates the amount of power delivered to the heaters, controlling the temperature.

Based on the results from the Real Live-Control Block, the PID can be further tuned to close the gap between simulation and real performance of the control system. The iterative process between the Simulation Block and the Real Live-Control Block may require a few tuning rounds until the desired PID coefficients are achieved. Once the PID coefficients are obtained, the user gains the ability to control the temperature profile with optimal control settings.

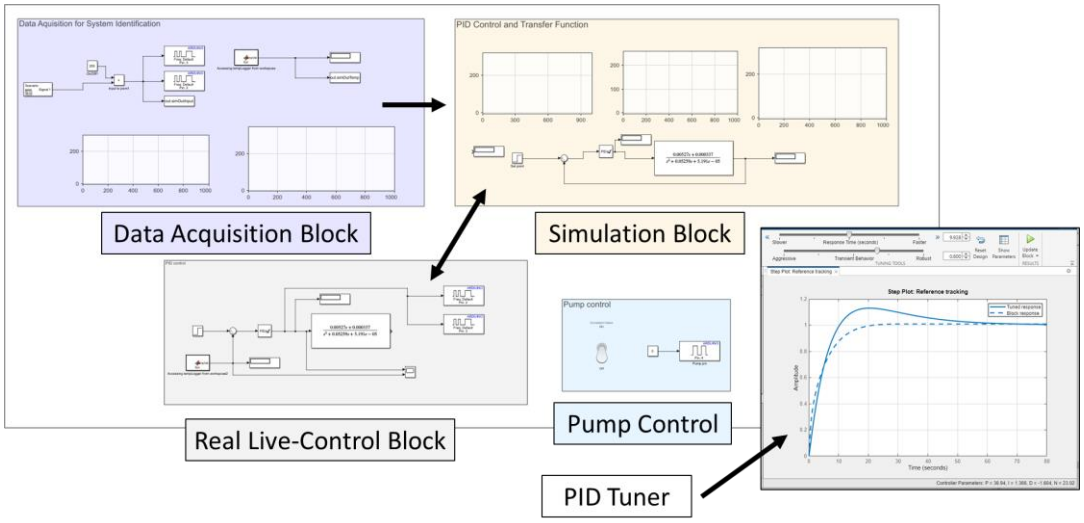

Figure 4-18: Simulink (Matlab) work-flow and work-environment for designing the PID controller for the hot-plate.

Figure 4-19 shows the response of a tuned PID controller to a step input. The step input (blue signal in the left plot) activates after ten seconds and instantaneously rises from 0°C to 60°C. The response signal of the simulated thermal-system is plotted on the same plot in orange color. Notably, the response demonstrates minimal overshoots and a sharp heating slope toward the set point temperature.

In the right plot of Figure 4-19, the resultant PWM signal controlling the Solid-State Relays (SSRs) is illustrated. The PWM control signal is derived solely from the Proportional-Derivative (PD) controller. Initially, the proportional part of the PD controller drives the PWM control signal to its maximum level of 255. This full-power signal is sustained until the simulated hot plate approaches the set-point temperature. At this point, the derivative part of the PD controller becomes active and significantly reduces the PWM control signal to zero. This rapid reduction in the PWM signal

effectively halts the hot plate's heating, thereby achieving minimal temperature overshoot. Once the overshoot is diminished, the PWM signal gently rises again to a minimal level, maintaining the hot plate at a constant temperature. The PID controller's well-tuned response ensures precise temperature control during the dynamic process, effectively minimizing deviations from the desired set point.

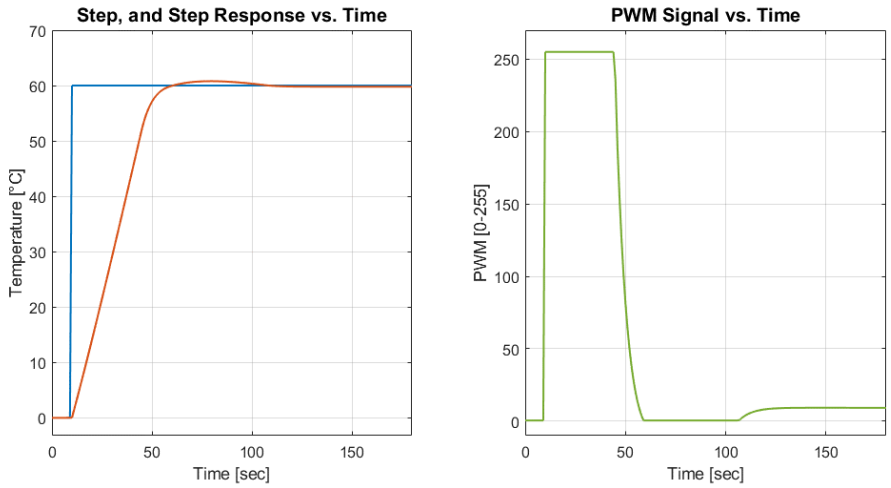

Figure 4-19: Resultant simulated performance the PD hot-plate controller.

Figure 4-20 displays the measured temperature curve of a potential temperature profile for the in-situ electrical experiment. Future iterations of the control system will integrate a ramp function to regulate the heating rate during the experiment. Although this function has not been implemented yet, the maximum PWM signal was trimmed at 90% to slow down the heating rate, resulting in a heating rate of 82.2°C/min. Once the temperature reaches the set-point temperature of 300°C, the experiment dwells for 5 minutes before activating the pump to cool the hot plate.

At this point, the pump control was not yet integrated into the control system, and it operates at full power once activated. The resultant cooling exponential curve exhibits a cooling time constant (tau) of approximately six seconds. This cooling characteristic demonstrates excellent performance. With the implemented control signal for the water pump, the cooling system has the potential for an optimal design of the temperature profile to terminate the experiment.

The design of the experiment termination is crucial in obtaining unbiased data. A well-designed termination should avoid thermal shocks that might deform the test sample while ensuring it is not too slow, preventing any chemical or diffusion interactions that could impact the measured data. Achieving a precise and controlled termination ensures accurate and reliable results from the in-situ electrical experiment.

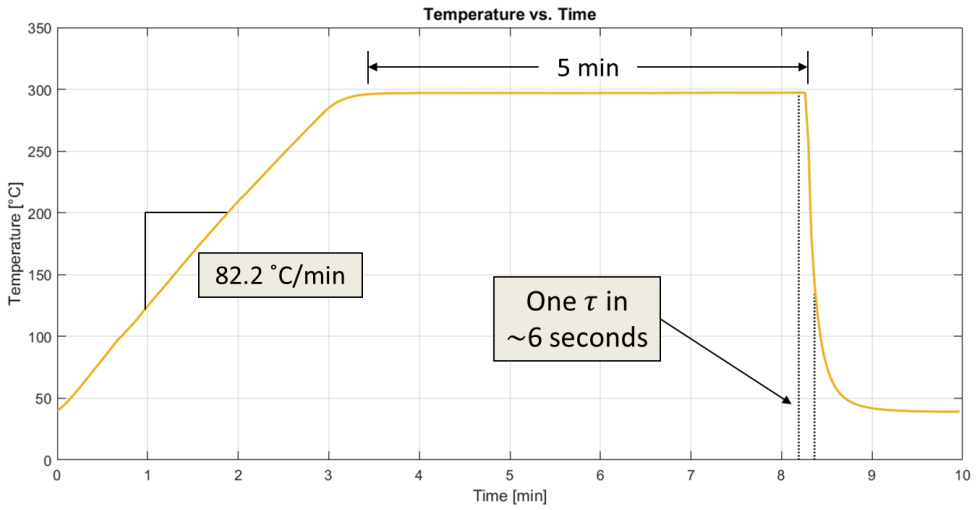

Figure 4-20: Measured temperature profile for the in-situ electrical experiment.

Figure 4-21 shows the capabilities of the hot plate coupled with the control system and the different experimental curves that the system can produce for different experimental needs.

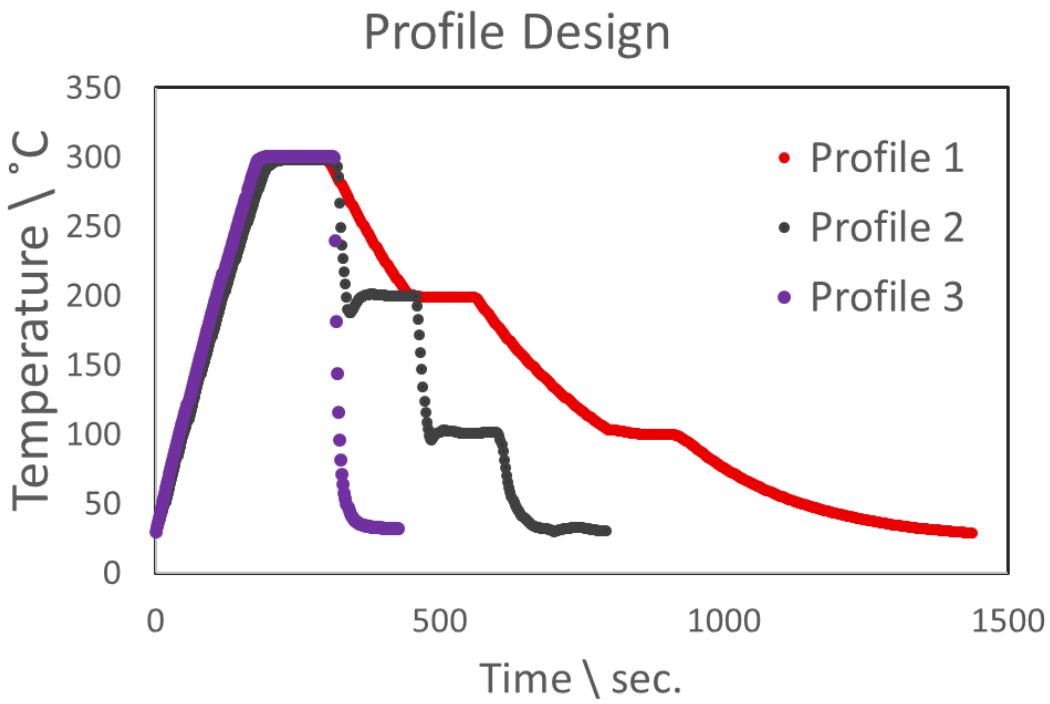

Figure 4-21: Temperature profiles for different experimental conditions.

4.1.5 Data Logging and Equipment Calibration

Data logging plays a critical role in the successful execution of the in-situ resistivity tests. Due to the logarithmic nature of the measured resistance data, the data logging device must be capable of sensing multiple logarithmic ranges. Typically, the data logger includes different sets of electrical circuits optimized to measure resistance within each logarithmic range. Therefore, any data logger used in the DRT experiment must feature an automatic-range function to accurately measure the resistivity signals across these various ranges.

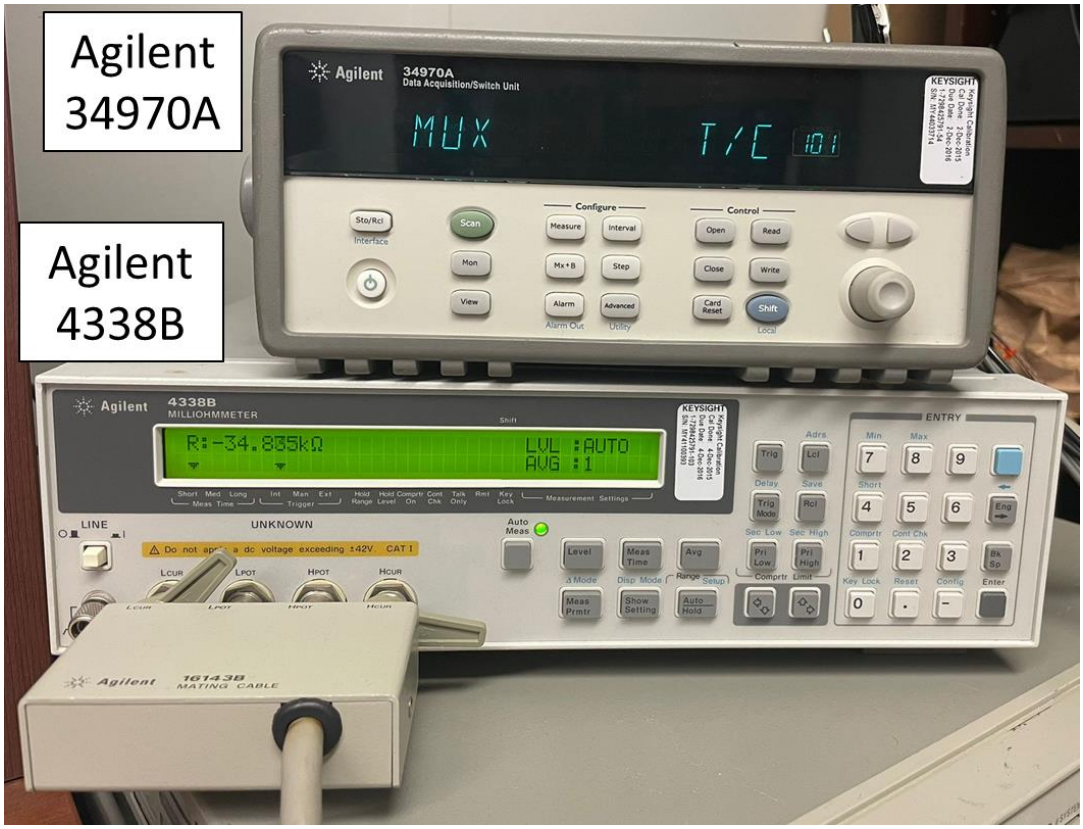

Figure 4-22: Data logging equipment use to calibrate, and log data during the in-situ electrical experiment.

Considering the need for an automatic-range function, two types of data loggers have been qualified for the in-situ electrical tests. The first one is the Agilent 34970A, shown in the top part of Figure 4-22. This data logger operates based on a multiplexer system that switches between channels. Each Agilent 34970A can host up to three data cards, with each data card capable of holding up to 20 individual channels (reducing to 5 signals per data card in a 4-point probe testing configuration). By employing fundamental measurements or voltage drop conversions, the Agilent 34970A can be

configured to measure various types of signals, including temperature, voltage drops, resistance, and electrical currents.

The second qualified data logger for the DRT is the Agilent 4338B, a one-channel instrument specifically designed to measure electrical resistance. This data logger is particularly well-suited for measuring low-level resistances within the micro-ohm and milli-ohm range, making it ideal for in-situ electrical test applications.

The two qualified data loggers, Agilent 4338B and Agilent 34970A, differ fundamentally in their measurement methods. The Agilent 4338B is an AC-based measurement tool, utilizing an AC test signal to mitigate thermo-electrical effects that can arise from prolonged DC currents. On the other hand, the Agilent 34970A is a DC-based measurement tool. Although the Agilent 34970A can take multiple, repeated measurements without activating the mechanical multiplexer when measuring from a single channel, using the multiplexer could introduce additional noise to the sensed signal. To reduce this noise, the specific selected channel can be set to a standby-mode, and measurements can be taken at digital-based requests through software like Matlab and a GPIB communication.

This clean sensing method was crucial during the calibration of the Agilent 4338B data logger. The calibration involved using standard resistors at logarithmic-based ranges. For milliohm-level calibration, a piece of 18-gauge copper wire was utilized with either of the testing devices.

To verify the normal operation of the data loggers, a second Agilent 34970A data logger was used to measure the supplied current of the 4-point probe resistance measurement method. The measured supplied current can then be compared against the reported values found in each of the data loggers' manuals. Figure 4-23 and Figure 4-24 display the logarithmic-based resistance measurement ranges and their corresponding testing currents for the Agilent 34970A data logger and the Agilent 4338B data logger, respectively.

DC, Resistance, and Temperature Accuracy Specifications

± (% of reading + % of range) [1]
Includes measurement error, switching error, and transducer conversion error

Function	Range [3]	Test Current or Burden Voltage	24 Hour [2] 23 °C ± 1 °C	90 Day 23 °C ± 5 °C	1 Year 23 °C ± 5 °C	C
DC Voltage	100.0000 mV		0.0030 + 0.0035	0.0040 + 0.0040	0.0050 + 0.0040	0
	1.000000 V		0.0020 + 0.0006	0.0030 + 0.0007	0.0040 + 0.0007	0
	10.00000 V		0.0015 + 0.0004	0.0020 + 0.0005	0.0035 + 0.0005	0
	100.0000 V		0.0020 + 0.0006	0.0035 + 0.0006	0.0045 + 0.0006	0
	300.000 V		0.0020 + 0.0020	0.0035 + 0.0030	0.0045 + 0.0030	0
Resistance [4]	100.0000 Ω	1 mA current source	0.0030 + 0.0035	0.008 + 0.004	0.010 + 0.004	0
	1.000000 kΩ	1 mA	0.0020 + 0.0006	0.008 + 0.001	0.010 + 0.001	0
	10.00000 kΩ	100 µA	0.0020 + 0.0005	0.008 + 0.001	0.010 + 0.001	0
	100.0000 kΩ	10 µA	0.0020 + 0.0005	0.008 + 0.001	0.010 + 0.001	0
	1.000000 MΩ	5 µA	0.002 + 0.001	0.008 + 0.001	0.010 + 0.001	0
	10.00000 MΩ	500 nA	0.015 + 0.001	0.020 + 0.001	0.040 + 0.001	0
	100.0000 MΩ	500 nA || 10 MΩ	0.300 + 0.010	0.800 + 0.010	0.800 + 0.010	0

Figure 4-23: Resistance ranges and their corresponding supplied current for the Agilent 34970A data logger.

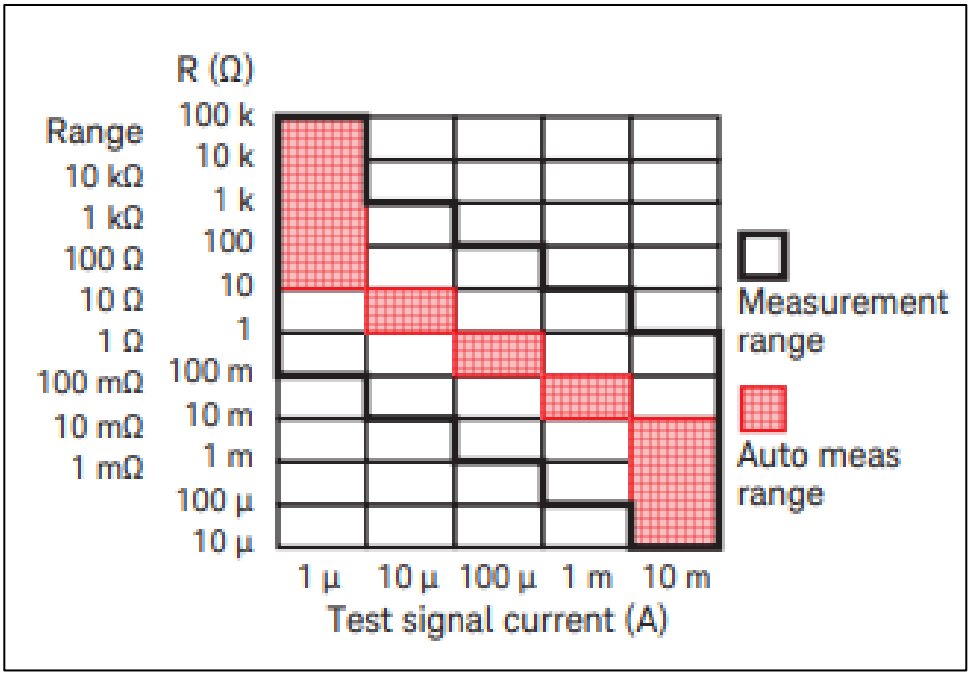

Figure 4-24: Resistance ranges and their corresponding supplied current for the Agilent 4338B milliohm-meter.

4.1.6 Apparatus and Location in the Laboratory

The location of the in-situ electrical test is of important in minimizing noise in the measured signal. Conducting the DRT without a partially controlled atmosphere requires careful consideration of various environmental factors, such as humidity levels, ambient temperatures, and consistent air streams, which can influence the final measured data values. Additionally, the test apparatus' location in the laboratory should have access to at least one nearby sufficient power outlet with a reliable current supply.

Currently, the apparatus is situated in room EGL1187 of the laboratory. It is placed close to a major electrical board to facilitate power supply. The main electrical line of the test is connected to a single-configuration electrical outlet, as shown in Figure 4-25. Using a single-configuration electrical outlet ensures that other users in

the lab will not share the same electrical phase and draw more current than is permissible (as sometime happens). By carefully selecting the appropriate location and ensuring a stable power supply, potential sources of noise and interference in the measured data can be minimized, thus enhancing the accuracy and reliability of the experiment.

Figure 4-25: In-situ electrical test apparatus location in the laboratory (left). The right figure shows the exclusive electrical outlet that is used by the test.

The in-situ electrical test apparatus, as shown in Figure 4-26, is mounted on a single adjustable 2000lb capacity mobile cart, featuring coarse and fine adjustable gears for easy maneuverability. The apparatus is structured into three main levels for efficient organization. The lower level houses the heavy equipment, including the diaphragm pump and the water reservoir. The middle level accommodates the testing and other electrical equipment, such as the main PC, data loggers, and a Wi-Fi receiver. The top level serves as the primary experiment zone, housing the hot plate, testing probes, probe's lifting crane, main electrical board, adjustable light and magnifier, adjustable monitor, and an adjustable lifter keyboard mount.

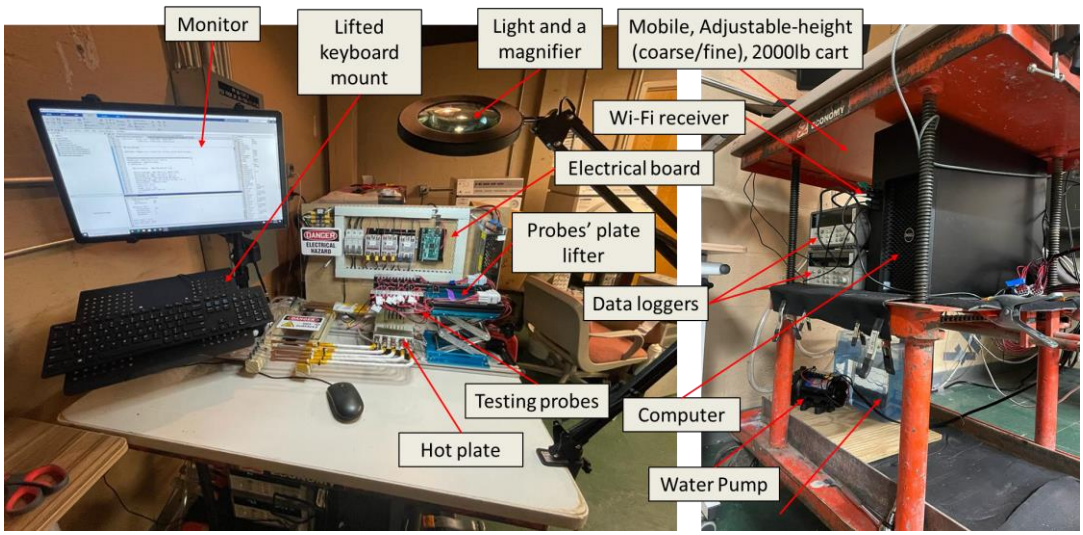

Figure 4-26: In-situ electrical test apparatus and components.

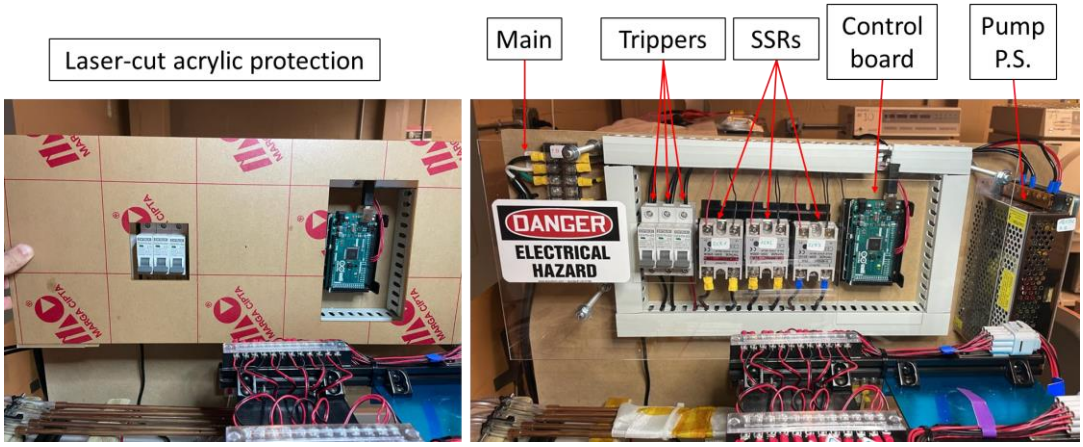

Figure 4-27: Electrical board, and laser-cut acrylic protection window for the in-situ electrical test.

The electrical board of the in-situ electrical test apparatus is illustrated in Figure 4-27. The figure also features the laser-cut acrylic protection for the electrical board. The electrical board, from left to right, consists of the main electrical input, electrical trippers, SSRs, control board, and a pump power supply. The acrylic protection offers easy access to both the electrical trippers and the control board. The electrical board is

designed to be modular, allowing for multiple configurations with respect to the testing zone. This modular design enhances flexibility and ease of maintenance for the electrical components of the test apparatus.

5 EXPERIMENTS RESULTS AND DISCUSSION

With the custom-made hot plate and testing equipment, in-situ electrical tests were conducted. As will described in this chapter, the electrical tests were followed by a series of additional data acquisition that helped construct the fundamental understanding to the first processing stage of the TLPS material at an open atmosphere condition. The follow-up data acquisition includes ESEM observations and image processing, EDS X-ray analysis, white light profilometer cross-section analysis, and additional data analysis through Arrhenius relationship modeling.

5.1 In-situ Electrical Characterization

In this study the tested samples were stencil printed on 0.762 mm thick Al_2O_3 boards. The original cross section area of the printed TLPS paste samples was designed to be 0.1 mm^2. The measured length of the sample was constant throughout the test and was set to be 64 mm. The stencil printed samples are shown in Figure 4-9. The metals that were used in this study and their relevant properties are listed in Table 5-1. In all paste combinations, the HMP to LMP ratio was maintained as 80% to 20% respectively. The metal loading for all paste combinations was 91% with the rest 9% weight as an organic binder.

To decouple the cross-effects occurring during the initial heating stage of the TLPS paste, we visually and quantitatively verified the size distribution and shape of the particles. This was accomplished by capturing environmental scanning electron

microscopy (ESEM) micrographs and employing image processing methods, as illustrated in Figure 5-1. Figure 5-1 shows that the particle distribution for both the LMP paste system is almost similar in shape and follow a lognormal distribution, with mean diameter of 3.13 μm, and 2.85 μm for In and Sn respectively. Thus, the effect of the particles' size can be ruled out as a factor in this study. Figure 5-1 also show that most of the particles are spherical and in the micron range.

Table 5-1: Metal powders used in this study.

Element	Electrical Resistivity $\mu\Omega \cdot cm$ @ 293 K	Melting Point $^{\circ}C$	HMP/LMP	Powder mesh size	Particle shape	Manufacture
Ag	1.59	961.9	HMP	-325	Spherical	Alfa-Aesar
In	8.4	156.6	LMP	-500	Spherical	Alfa-Aesar
Sn	10.9	232.0	LMP	-500	Spherical	US Research Nanomaterials, Inc

For this study, In and Sn were used as the LMP and Ag as the HMP. The metal particles were mixed with three commercially available organic binders: A, B, and C. In addition, two heating rates of 30 $^{\circ}C/min$ and 90 $^{\circ}C/min$ were tested. Table 5-2 shows all the paste combinations that were tested in this study. Eighteen to 28 individual samples were tested for each paste combination.

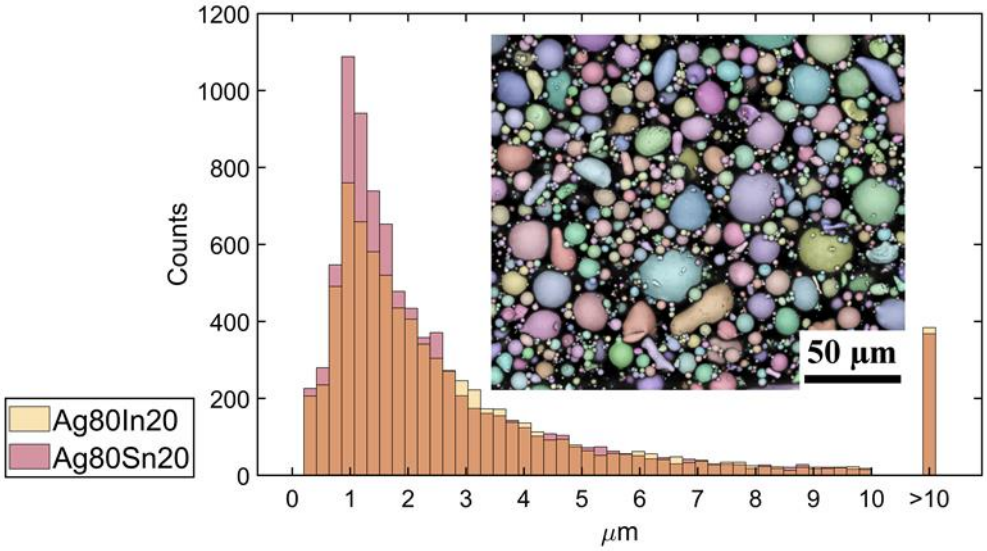

Figure 5-1: Particle size distribution (diameter) of the both the Ag-In and Ag-Sn paste formulations.

Table 5-2: Test combinations of different paste formulations and heating rates.

Test Combination	Organic Binder	LMP	HMP	Heating Rate
AI9	A	In	Ag	90 $^{\circ}C/min$
BI9	B	In	Ag	90 $^{\circ}C/min$
CI9	C	In	Ag	90 $^{\circ}C/min$
AS9	A	Sn	Ag	90 $^{\circ}C/min$
BS9	B	Sn	Ag	90 $^{\circ}C/min$
CS9	C	Sn	Ag	90 $^{\circ}C/min$
AI3	A	In	Ag	30 $^{\circ}C/min$
AS3	A	Sn	Ag	30 $^{\circ}C/min$

The in-situ electrical tests conducted on various paste combinations have provided valuable insights into the underlying competing mechanisms that contribute to the electrical conductivity development and structural stability of the TLPS material during early processing stages. Figure 5-2 presents the summarized raw data of the in-situ electrical tests, where the y-axis represents the electrical resistivity in units of $\Omega \cdot$

cm, represented in a log scale, and the x-axis represents temperature in $^{\circ}C$. Analysis of the plots in Figure 5-2 reveals a consistent trend in the electrical evolution of the TLPS material.

The general trend exhibits a dual decrease in resistivity values, with the initial drop being more substantial in the majority of instances. Specifically, the first drop signifies a change in resistivity values that can span over six orders of magnitude, typically ranging s from 1 x 10^4 $\mu\Omega \cdot cm$ as the upper limit of the data logger, down to 1 x 10^{-3} $\mu\Omega \cdot cm$. In specific test combinations, the first drop in resistivity values is followed by a lower plateau region where resistivity remains relatively stable with minimal changes. The duration of this lower plateau region can vary, ranging from just a few degrees Celsius, as observed in test combination AI9, to over ΔT = 100 $^{\circ}$C, as seen in test combination AS3 in Figure 5-2.b. Following the second major drop, the resistivity curves stabilize and exhibit minimal additional changes as the temperature increases.

To facilitate clear visualization of different effects, the plots are categorized accordingly. Figure 5-2.a and Figure 5-2.b illustrate the effect of heating rates on In and Sn-based samples, respectively. Remarkably, irrespective of the LMP selection, the heating rate exhibits a similar impact on the TLPS systems. In both In and Sn-based samples, the electrical signal initiates at lower temperatures when subjected to low heating rates, as seen in test combinations AI3 and AS3. However, once the material

experiences its first major drop in resistivity, the performance of both low and high heating rate samples converges, resulting in similar resistivity trend.

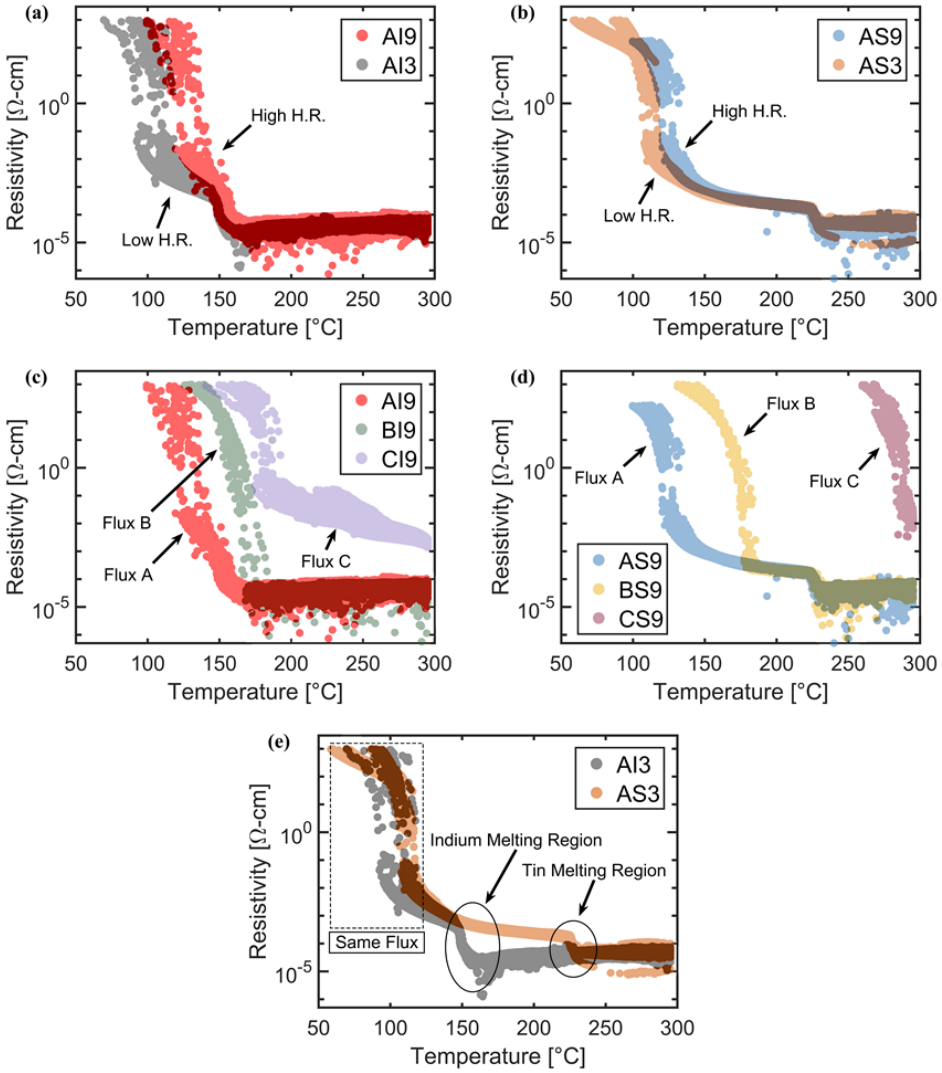

Figure 5-2: (a) Effect of heating rate on In-based samples. (b) Effect of heating rate on Sn-based samples. (c) Effect of flux selection on In-based samples. (d) Effect of flux selection on Sn-based samples. (e) Effect of LMP selection.

Figure 5-2.c and Figure 5-2.d demonstrate the influence of different organic binders on the paste formulations with In and Sn-based samples, respectively. Notably,

the selection of flux significantly affects the shape, location, and final value of the resistivity curve evolution in both cases. Flux A consistently exhibits electrical signals at lower temperatures compared to flux B and flux C. This observation effectively isolates the effect of flux selection on the electrical performance of TLPS pastes, irrespective of the LMP choice. Furthermore, test combinations utilizing flux A and flux B exhibited resistivity values of approximately 1 x 10^{-5} $\mu\Omega \cdot cm$ at 300 ˚C. In contrast, formulations based on flux C achieved resistivity values of about 1 x 10^{-3} $\mu\Omega \cdot cm$ at the same temperature.

Figure 5-2.e specifically focuses on the impact of different LMP selections on TLPS paste formulations. Test samples AI3 and AS3, employing the same flux and heating rate, are compared. The plot in Figure 5-2.e reveals that the second major drop in electrical resistivity corresponds to the melting of the LMP, occurring around the melting point of In and Sn for test combinations AI3 and AS3, respectively. The three main effects during the experiment's heating stage are summarized in Figure 5-3. The figure shows that:

A. Changing the LMP in the paste formulations can delay or promote the second main drop in the resistivity values of the TLPS material.

B. Changing the flux selection has the potential to completely change the location and the overall trend of the electrical evolution of the material.

C. Changing the heating rate of the processing has an effect of the first major drop in the electrical resistivity of the TLPS material.

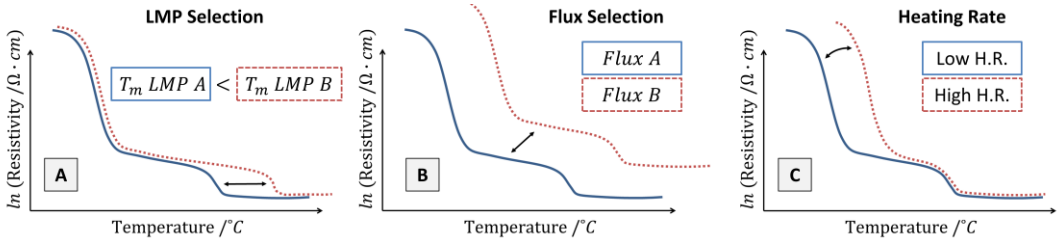

Figure 5-3: Shows the three main effects that were observed in the in-situ electrical resistivity tests.

5.2 Electrical Percolation and Packing Densities

In order to gain deeper insights into the underlying mechanism driving the initial significant decline in electrical resistivity of the TLPS material, a comprehensive analysis utilizing ESEM micrographs and image processing techniques was conducted. The packing densities of test combinations BI9, BS9, AI3, and AS3 were quantitatively evaluated as a function of temperature, and the results are displayed in Figure 5-4. Eighteen different samples were measured with a total sampled area of 0.716 mm^2 per each temperature and test combination.

Figure 5-4 demonstrates that in the lower temperature range below 130 ˚C, variations in packing density can be attributed to the use of different organic binders, specifically A and B. Test combinations utilizing flux B exhibit a marginal 4% reduction in packing density between 50 ˚C and 100 ˚C. This observation may be correlated with the delayed electrical response of these test combinations, as shown earlier in Figure 5-2.c and Figure 5-2.d. As the respective melting points of the indium

and tin-based LMP are reached, a decrease in packing density is observed. Importantly, this reduction in packing density is consistent regardless of the organic binder selection. Before reaching the melting points of the LMP, test combinations BI9, BS9, AI3, and AS3 demonstrate respective increases in packing density of 8.22%, 14.62%, 9.95%, and 8.09% compared to their minimum measured packing densities.

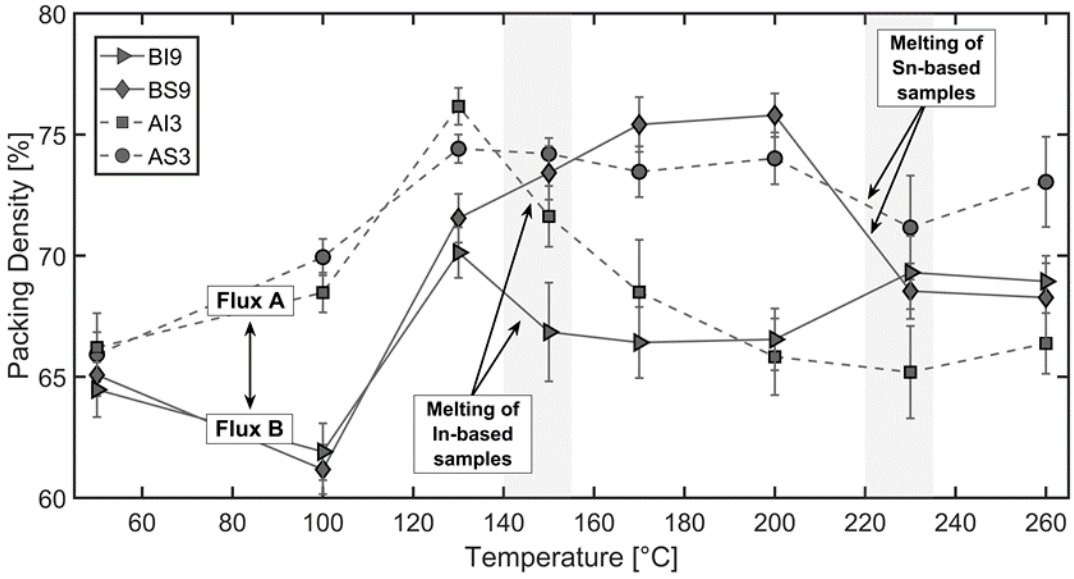

Figure 5-4: Packing densities vs. temperature of test combinations BI9, BS9, AI3, and AS3.

A set of representative images, complementary to Figure 5-4, of the Sn-based test combination BS9 is presented in Figure 5-5. In particular, below the melting point of Sn at approximately 232 $^{\circ}C$, the metal particles exhibit incremental increased proximity to each other, indicating the formation of electrical percolation networks. Additionally, the melting of Sn particles and the initial development of a structural

backbone are evident as the temperature reaches 230 ˚C and 260 ˚C. These micrographs also reveal the formation of pores and the residual presence of the organic binder.

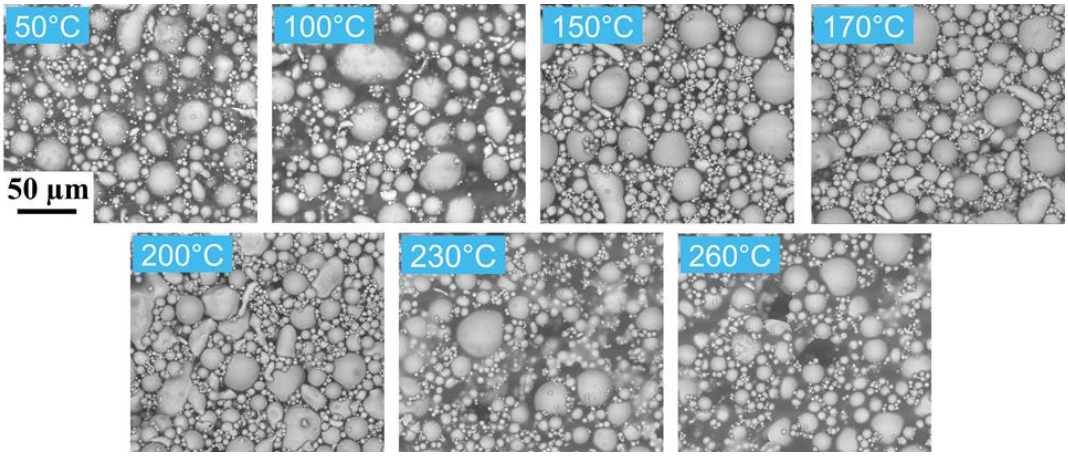

Figure 5-5: Micrographs of test combinations BS9 at temperatures of 50, 100, 150, 170, 200, 230, and 260 ˚C.

The Energy Dispersive Spectroscopy (EDS) readings of In-based test combination AI3, and Sn-based test combination AS3 are presented in Figure 5-6. The EDS readings were obtained from the top of the samples. For both the Indium-based combination AI3, and the Sn-based combination AS3, the EDS readings of carbon at around 0.28 keV, which can be considered as signal of the organic binder, show reduction in signal intensities when approaching to the respective melting temperatures of the LMPs. These trends support the increase in packing density below the melting temperatures of the LMPs, and the formation of electrical percolation networks. Additionally, for both AI3 and AS3, at temperatures above the respective melting temperatures of the LMPs, the EDS signal of the organic material experiences a sudden increase in its intensity. The presence of aluminum in all the spectrums is most likely

originated from the Al_2O_3 ceramic substrates, while the presence of oxygen signals can be related to both the ceramic substrate and the organic material.

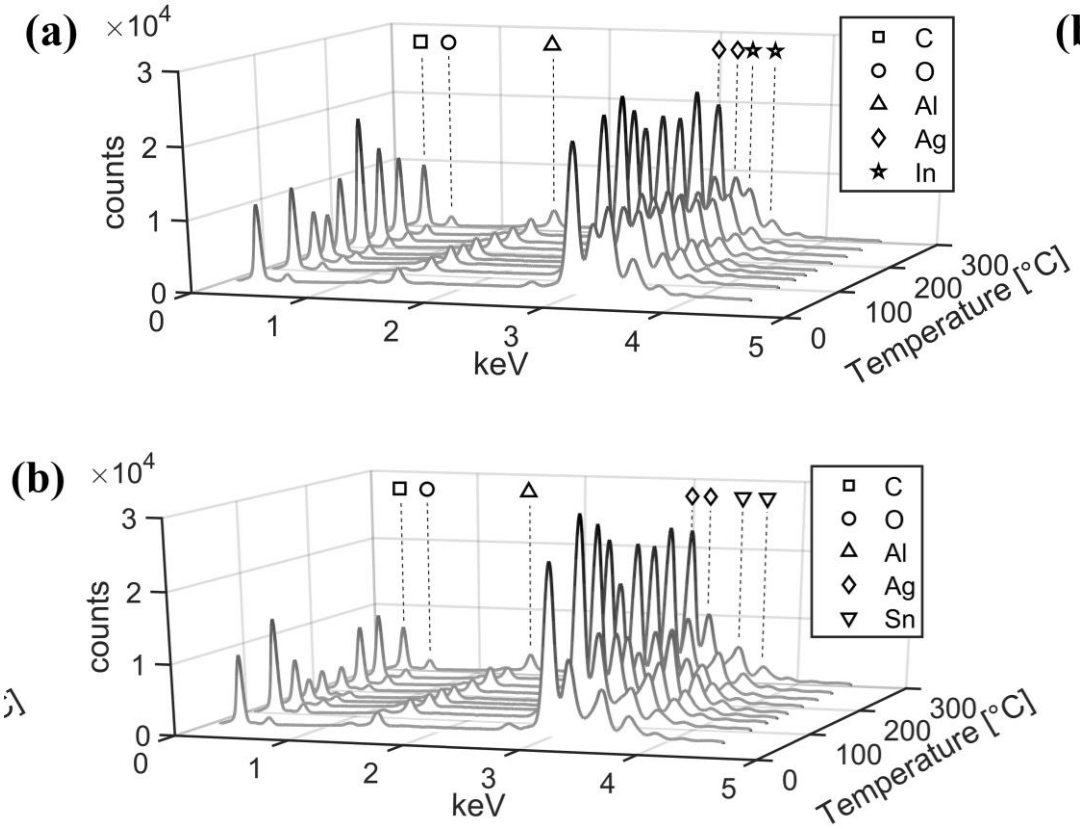

Figure 5-6: EDS spectrums of test combinations AI3 (a) and AS3 (b) as a function of temperature.

Figure 5-7.a and Figure 5-7.b show the elemental maps of test combination AI3 at 130 and 260 ˚C, respectively, and Figure 5-7.c and Figure 5-7.d shows the elemental maps of test combinations AS3 at 130 and 260 ˚C, respectively. The colors red, purple, and green represent the HMP, LMP, and organic material respectively.

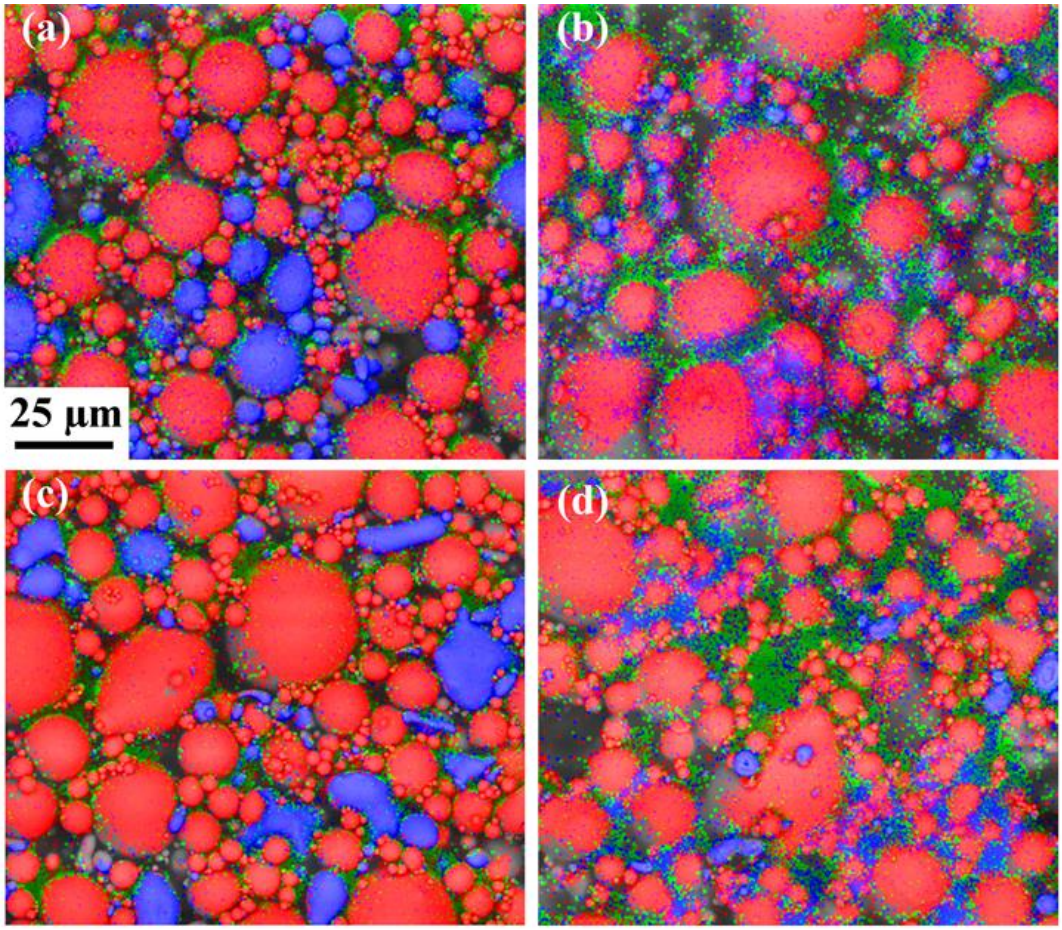

Figure 5-7: EDS elemental maps of: (a) AI3 at 130 ˚C. (b) AI3 at 260 ˚C. (c) AS3 at 130 ˚C. (d) AS3 at 260 ˚C. Red = HMP, Purple = LMP, Green = Organic material.

The EDS elemental maps presented in Figure 5-7 confirm the increased signal of organic material at temperatures higher than the respective melting temperatures of the LMPs. At the time of the LMP melting, interactions occur between the metal and the organic binder liquid phases. The increased signal of organic material during the melting of the LMP is likely due to these interactions, as described in [162]. The densification of the metal system is also inhibited by outgassing of the organic binder [163,164]. The presence of the organic binder during the melting of the LMP

potentially impedes further system densification. However, figures Figure 5-7.b and Figure 5-7.d demonstrates that despite the presence of some organic binder, certain LMPs retained their spherical shape. The failure of certain LMPs to react or wet the HMP's surface upon reaching their melting point can be attributed to inadequate removal of the oxidation layer. Previous studies have demonstrated a substantial increase in the oxide layer of pure indium particles when they reach their melting point at 156 ˚C [165]. However, in both the In-based and Sn-based pastes, the majority of LMPs melt and establish metal-liquid bridges between the HMP Ag particles, as shown in Figure 5-7.

5.3 LMP Liquid Phase Behavior

The discussion of the metal-phase liquid bridges is important for the understanding of the structural formation of the paste, as well as the ability to predict if the system will undergo densification, or increased state of porosity. For suspension particulate systems, there are four states of solid-liquid interactions which are defined as follows [166–169]:

1. Pendular state: the liquid bridges are isolated from each other.
2. Funicular state: the liquid bridges form some degree of coalescence. While the liquid bridges may coalesce with each other, the coalescence is not uniform and some gas or secondary liquid-phase is present between the molten metal liquid bridges.

3. Capillary state: forms a uniform and homogeneous state of liquid bridges between the HMP solid-phase particles.
4. Drop state: the HMP solid-phase particles are completely submerged by the molten LMP phase.

Upon melting if the LMP, and with relative low saturation of molten liquid metal that was used in this study (20% LMP to 80% HMP), the TLPS paste system experience all of the four different states of liquid bridge solid-liquid configuration as shown in Figure 5-8. The pendular state can often be seen between large Ag-particles ($D > 25\ \mu m$) as shown in Figure 5-8.a. The funicular and capillary states are seen between medium size particles ($5 < D < 25\ \mu m$) and are shown in Figure 5-8.b and Figure 5-8.c. With low saturation systems, the drop-state can often be seen coating a group of smaller silver particles ($D < 5\ \mu m$) as shown in Figure 5-8.d, which in fact forms a locally high saturation region. When the solid-state particle size is smaller, the probability of the liquid metal to fully coat the particles increases. The coexistence of multi-state solid-liquid interactions such as the pendular, funicular, capillary, and drop states during the processing of the TLPS paste is most likely the main reason for the decrease in packing densities of the TLPS systems during the melting of the LMP as shown earlier in Figure 5-7.

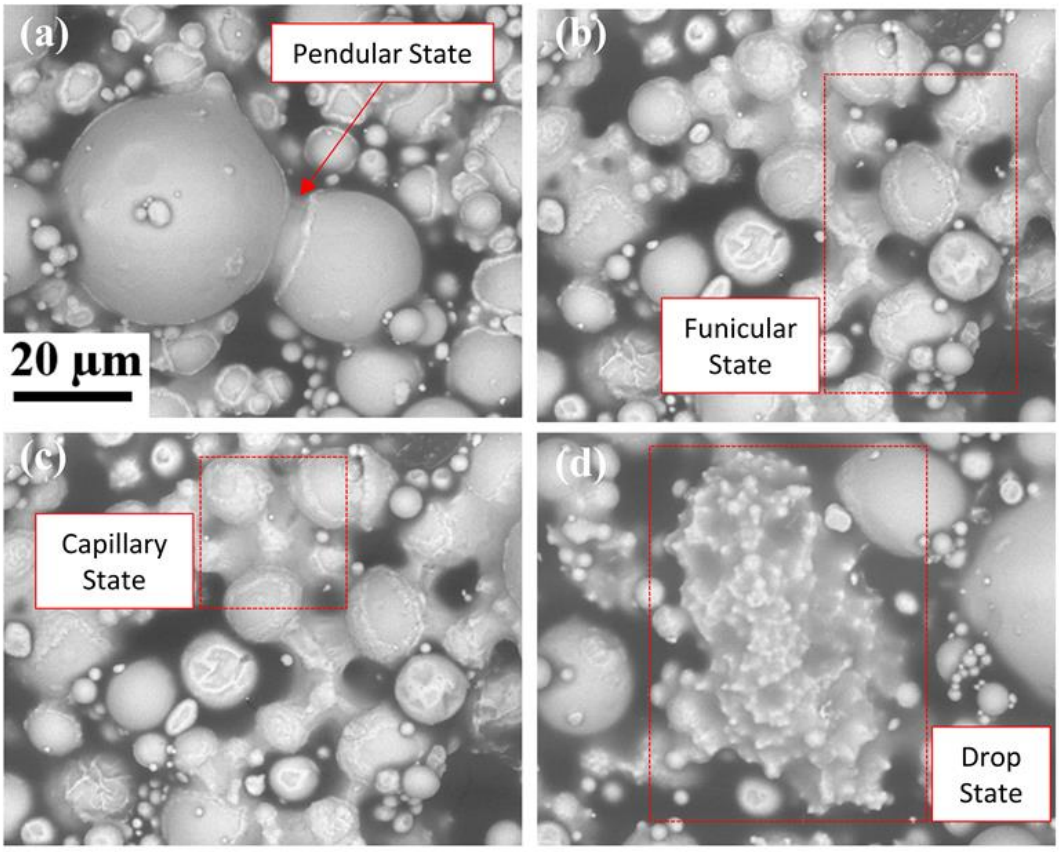

Figure 5-8: Shows the four states of liquid bridges and solid-liquid interactions that the TLPS paste experience during the melting of the LMP. (a) Pendular state. (b) Funicular state. (c) Capillary state. (d) Drop state.

The TLPS paste system in this study is characterized by a relatively low saturation of metal liquid phase material, resulting in an isolated state of solid-state Ag particles. These particles experience attractive forces from various directions, which can be attributed to the minimization of the surface energy of liquid bridges between them. The suction pressure (S) between similar-sized particles by the capillary bridge can be calculated using the Young-Laplace equation, which is a function of the liquid

surface tension and the external (r_{ext}) and internal (r_{int}) radii of the liquid bridge. This equation is expressed as [170]:

$$S = T\left(\frac{1}{r_{ext}} - \frac{1}{r_{int}}\right) \quad 5.1$$

The force applied by two neighboring particles can be determined using equation 5.1, which considers the suction pressure and the area of the liquid bridge:

$$F = S\pi r_{int}^2 + T(2\pi r_{int}) \quad 5.2$$

Illustrations of equations 5.1 and 5.2 are shown in Figure 5-9.a and Figure 5-9.b respectively. The attractive and capillary force between particles will cease to be effective at a critical distance, causing the liquid bridge to rupture [168].

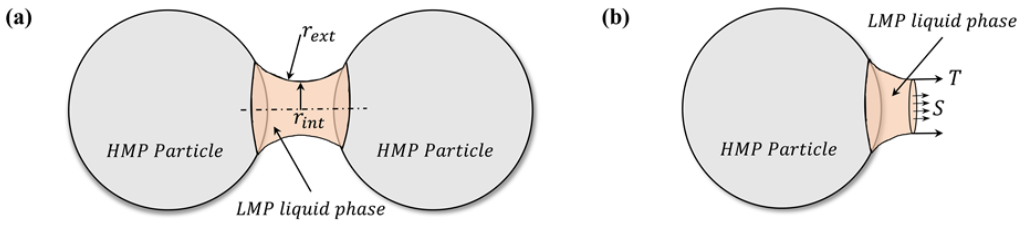

Figure 5-9: Illustration of the liquid bridge between two similar size solid-phase particles (a). Illustration of the suction pressure S and the surface tension T forming the capillary force between the solid particles (b).

It should be noted that these equations are applicable only for isolated liquid bridges, as in the pendular state. Forces applied on funicular and capillary systems are discussed in further detail in [166,168]. Various studies have explored the effects of applied forces on particulate systems of different radii [171,172], as well as different contact angles resulting from different wetting of the liquid phase over solid-state particles [173]. In the TLPS paste system, all of these scenarios coexist at and above

the melting point of the LMP, increasing the probability of an inhomogeneous state of densification.

5.4 Formation of Structural Backbone

Resistivity, denoted as ρ is the resistivity in $\Omega \cdot cm$, is a fundamental property of materials and it can be represented as follows:

$$\rho = \frac{RA}{L} \tag{5.3}$$

It is necessary to verify if the TLPS paste samples undergo a change in volume in order to adjust equation **5.3** as follows:

$$\rho(T) = \frac{R(T)A(T)}{L} \tag{5.4}$$

Keyence structured white light profiler microscope model VR-3200 was used to measure the cross sections of our samples at varying temperatures. Specifically, the ceramic substrate with the printed samples were removed from the hot plate at temperatures ranging from 50 ˚C to 300 ˚C and immediately cooled them on a cool metal surface. For each temperature, we measured six different samples across a 1.893 mm for each sample. Figure 5-10.a and Figure 5-10.b show the cross section of In-based samples from test combination AI9 before and after the melting of the LMP at 150 ˚C and 170 ˚C, respectively. Despite an initial stencil cross section of 0.1 mm^2, the structured white light profiler microscope measurements failed to detect a significant change or reduction in cross section. This can be clearly seen in the fit line in Figure 5-10.c that shows a negligible change in cross section of 5 x 10^{-5} $mm^2 \cdot {}^{\circ}C^{-1}$,

and poor goodness of fit value of 19.58%. This result can be attributed to two main reasons. First, cross-section measurements at different temperatures represent point-wise measurements and thus are sensitive to any variability originating from the stencil paste deposition. Performing an in-situ cross-section measurement would overcome this variability issue as it will follow the cross-section development with respect to the initial cross-section measurement of individual samples. Second, the quick formation of the structural backbone of the samples resulted in minimal to no change in overall cross-section measurement. We observed early reactions fronts between the metal liquid-phase and the Ag HMP immediately after the melting of the LMP, forming IMCs with higher melting points and reduced ability to liquify at low temperatures, as shown in Figure 5-10.d. In the ESEM, the backscatter mode can detect the IMC reaction fronts due to their different atomic weight, which results in different contrast in the image. The reaction fronts are highlighted in Figure 5-10.e.

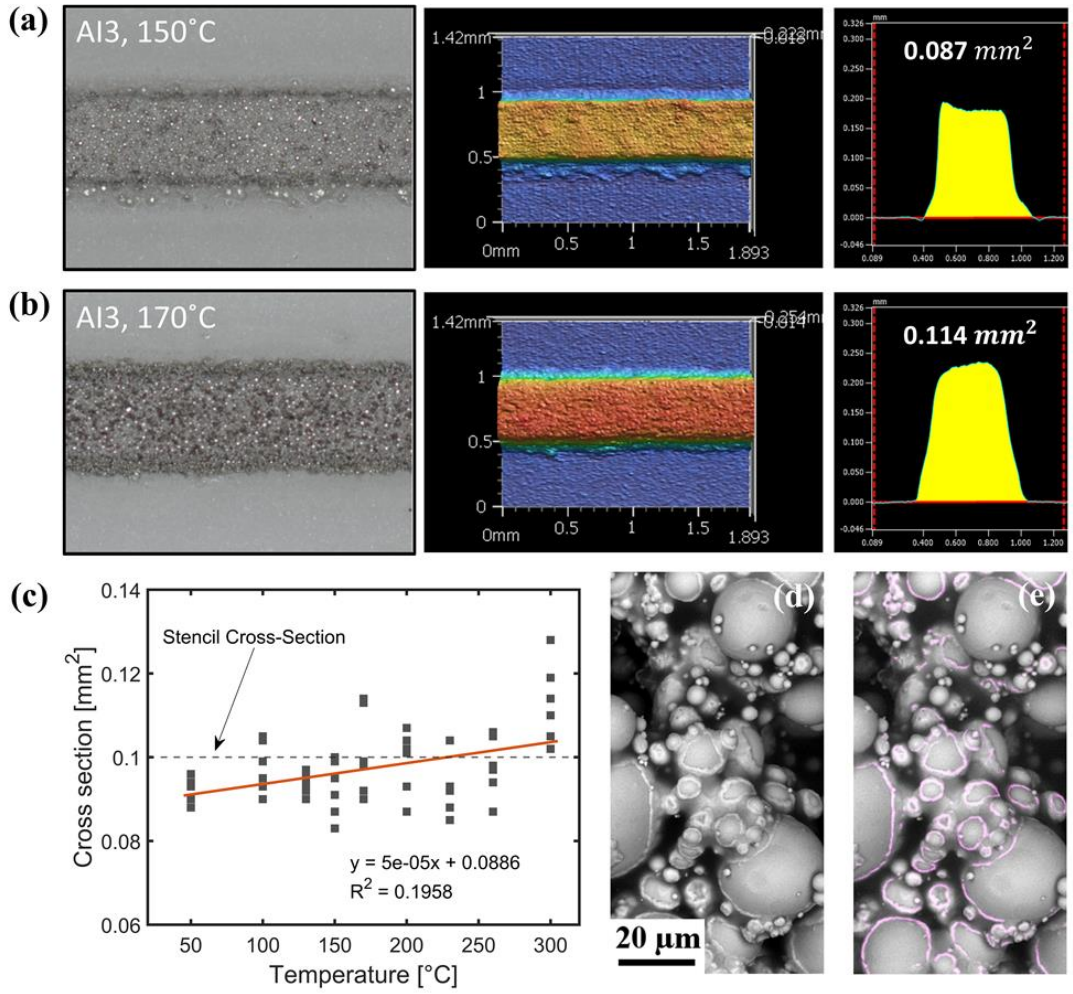

Figure 5-10: Structured white light profiler microscope measurements of test combination AI3 at 150 ˚C (a), and at 170 ˚C (b). Cross section of test combination AI9 at different temperatures (c). ESEM micrographs of In-based test combination AI3 sample at 170 ˚C (d), and the same figure with highlighted reaction fronts (e).

5.5 Characterization Summery

At this stage of the analysis, the multiple processes that occur during the initial heating stage of the TLPS paste can be illustrated. The electrical conductivity and structural formation of TLPS paste can be divided into five main stages, which are summarized as follows:

(S.I). The first stage as shown in Figure 5-11 is the initial paste phase. In this stage, the conductive particles are embedded in the non-conductive organic binder such that the resistance is too high to detect. This length of this stage is governed by the composition and selection of the organic binder.

(S.II). At the second stage the conductive particles are still isolated from each other by the organic binder. However, an initial weak electrical signal can be attributed to the evaporation of lighter weight organic molecules of the organic binder complex as described in [174] and [175], and the respective minimal increase in volume fraction of the conductive particles. The volatile low molecular weight molecules near the binder-vapor interface evaporate first, while non-volatile longer and heavier organic molecules undergo degradation to produce volatile decomposition products such as monomers, dimers, CO_2, and H_2O. Capillary-driven binder redistribution accelerates the removal of the non-volatile molecules.

(S.III). TLPS paste experiences a significant reduction in electrical resistivity, irrespective of the organic binder used. This reduction results from a more substantial increase in the volume fraction of conductive particles, as discussed in [176] and [177]. This increase enables the system to cross the percolation network threshold, which typically follows an exponential trend, as described in [178]. The electrical data presented in Figure 5-2.c and Figure 5-2.d suggest that the sufficient increase in the volume fraction of the conductive particles depends on the properties of the organic binder itself, implying a correlation between the percolation network threshold and an

accelerate rate of binder burnout, as also outlined in [174]. The visible rise in the volume fraction of conductive particles is particularly evident at the top of the samples, providing empirical support for the theory that the percolation network develops from the uppermost regions towards the lower portions of the samples, as shown in Figure 5-11.

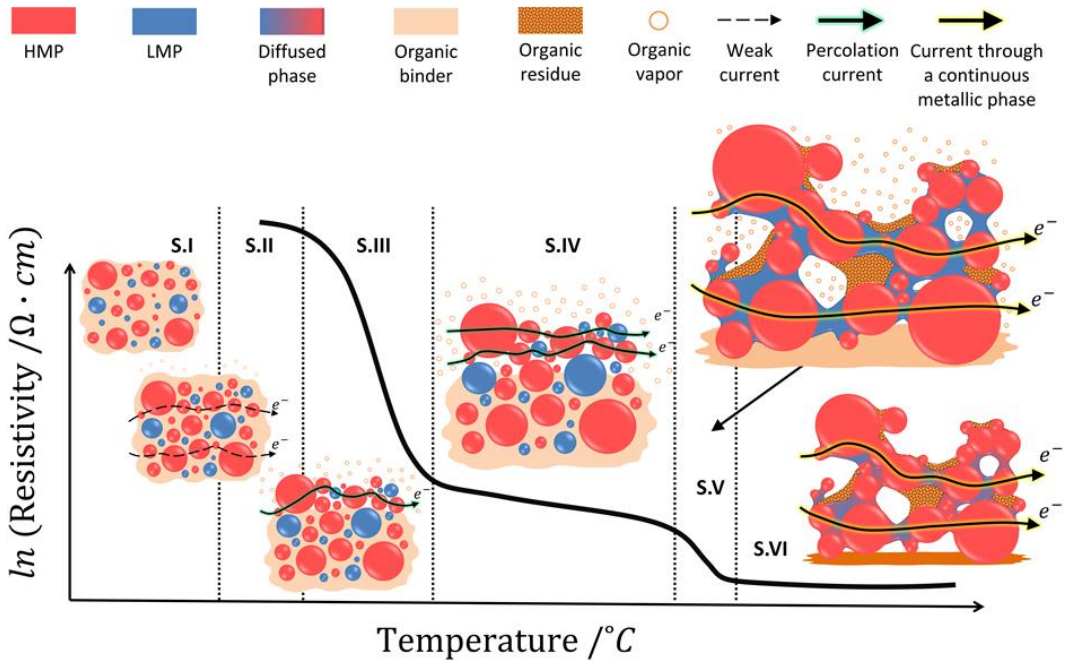

Figure 5-11: Illustration of the electrical and structural evolution of the TLPS paste.

(S.IV). After the system passes the conductive percolation threshold, the change in electrical performance is minimal. The organic binder continues to evaporate and initiates more electrical paths through the samples. The additional electrical path cause to farther reduction in the equivalent resistance following the traditional Ohm's Law.

(S.V). The fifth stage of the electrical and structural evolution of TLPS is considered the most critical stage. In this stage, multiple physical phenomena occur simultaneously at different magnitudes, such as liquid-solid diffusion, different states of liquid-solid interactions and forces, particulate suspensions with dual liquid phase interactions, oxidation removal by the organic binder, and continuous burnout and outgassing of the organic burnout. The saturation levels of the metal liquid-phase determine the state of the liquid-solid interaction and forces. Adding to the complexity of the different states of capillary forces between the Ag HMP is the continuous diffusion between the LMP and HMP. The diffuse interface contributes to the kinetics in which the overall system generates its backbone structure. A numerical study by [179] attempts to show the dynamics of such a system. The quick generation of backbone structure can be advantageous from an AM point of view, allowing for sequential layer printing with minimal partial heating times. However, if the system is locked into a porous structural state, further densification can be challenging [180]. Incomplete removal of the organic binder at the melting time of the LMP hinders intimate contact between the LMP and HMP and prevents the system from achieving its full densification potential.

(S.VI). The sixth stage marks the end of the temperature-dependent electrical conductivity evolution of the TLPS paste. At this stage, relatively slower solid-state diffusion becomes the dominant diffusion mechanism of the system. Furthermore, if the Ag particles are not adequately coated or alloyed with the LMP, the system

experiences oxidation and decreased electrical conductivity. The structural stability of the material develops as the storage modulus increases in magnitude compared to the loss modulus of the system, as shown in [181]. Flux residue is also a concern for the structural and electrical performance of the system, preventing the completion of densification, potentially causing stress concentrations and oxidation of the system.

5.6 Related Energies

Stages three to five can also be analyzed from an Arrhenius relationship point of view. The Arrhenius relationship for electrical conductivity can be written as follows:

$$\sigma = \sigma_0 \, exp\left(-\frac{E_a}{RT}\right) \tag{5.5}$$

Where σ is the conductivity in $S \cdot cm^{-1}$, σ_0 the pre-exponential factor in $S \cdot cm^{-1}$ (i.e. the maximum conductivity that the material would have at infinite temperature), E_a is the activation energy in $kJ \cdot mol^{-1}$, R the universal gas constant, and T the absolute temperature in Kelvin. Taking the logarithmic of both sides of equation **5.5** allows to fit the data with the standard linear regression model (LM) as follows:

$$y_i = \beta_0 + \beta_1 x_i + \epsilon_i \tag{5.6}$$

$$\epsilon_i \sim N(0, \sigma_\epsilon^2) \tag{5.7}$$

Where y_i is the ith estimate response value, x_i is the ith predictor, β_0 is the intercept, β_1 is the slope, and ϵ_i is the normally distributed random error term with a

variance of σ_ϵ^2. This notation assumes that not two measurements were taken at the same predictor value. In terms of the Arrhenius relationship, equations **5.5** and **5.6** can be written as follows:

$$ln(\sigma)_i = ln(\sigma_0) + \left(\frac{1}{T_i}\right)\left(\frac{-E_a}{R}\right) + \epsilon_i \qquad 5.8$$

Equation **5.8** can be fitted separately to stages three, four, and five. We did not attempt to fit the equation to stage two due to insufficient amount of data (stage two values approaching the measurement limits of the data logger), and to stage six as it showed negative positive slope in the Arrhenius plots which correspond to negative energies. Figure 5-12 shows the multiple Arrhenius fits of equation **5.8** applied to the data of test combination AI3. As can be seen in the figure 16.a, the fit for the fifth stage perform reasonably well with goodness of fit value R^2 of 87.00. However, the fit for the fourth stage performs worse with R^2 value of 62.75, and the fit for stage three shows that only 6% of the variation in the electrical conductivity can be explained with the inverse of temperature. When performing the same fit procedure onto an individual sample from the sample test combination, the goodness of fit values improve dramatically and score values of 96.51, 97.78, and 96.66 for stages five, four and three respectively, as shown in Figure 5-12.b. Visual inspection of the fit of the third stage in Figure 5-12.a shows that the fit line goes across the samples instead of along the general slope of the data of this stage. This is particularly noticeable during the third stage. In addition, the relative increase in the R^2 values from stage three to stage five can be explained by the fact that the data from the third stage, which was found to be

correlated to organic evaporation kinetics, and formation of electrical percolation network, is more stochastic in nature. When the electrical measurements approaching stage five in which the LMP melt, the electrical resistivity values start to converge and become less random, and more deterministic.

To solve the apparent randomness across the samples, we expand the standard LM formula and use Linear Mixed Models (LMM) [67,68] which allow to use random intercepts, random slopes, or both. Random Intercept LMM formula is written as follows:

$$y_{ij} = \beta_0 + \beta_1 x_{ij} + \alpha_{0j} + \epsilon_{ij} \quad 5.9$$

$$\alpha_{0j} \sim N\left(0, \sigma_{\alpha_0}^2\right) \quad 5.10$$

$$\epsilon_{ij} \sim N(0, \sigma_{\epsilon}^2) \quad 5.11$$

Where y_{ij} is the ith response of the jth group. The terms β_0 and β_1 are the fixed intercept and slope of the level 2 data, with ϵ_{ij} is the level 1 random error term with a gaussian distribution, and a variance of σ_{ϵ}^2. The level two random intercept α_{0j} is normally distributed and has a variance of $\sigma_{\alpha_0}^2$. The random intercept model is restricted to have the same slopes for all data levels, i.e., the slope of the mean response of all the data, and the slope of the mean response per individual groups of data is similar. The application of equation **5.9** is shown in Figure 5-12.c.

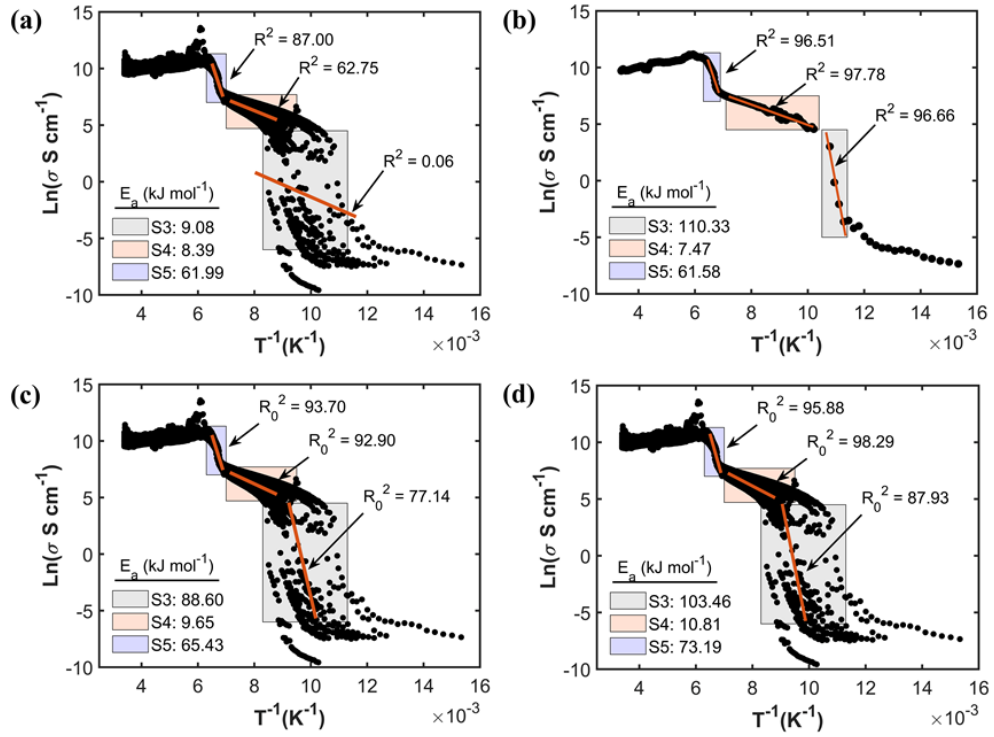

Figure 5-12: Arrhenius fits using LM and their respective activation energies for stages 3,4, and 5 for test combination AI3 (a). Arrhenius fits using LM and their respective activation energies for stages 3,4, and 5 for only one sample from test combination AI3 (b). Arrhenius fits using random intercept LMM and their respective activation energies for stages 3,4, and 5 for test combination AI3 (c). Arrhenius fits using random intercept and slope LMM, and their respective activation energies for stages 3,4, and 5 for test combination AI3 (d).

To further expand the random intercept model, an added term of random slope per each data group can be added. The LMM with both random intercepts and random slopes can be written as follows:

$$y_{ij} = \beta_0 + \beta_1 x_{ij} + \alpha_{0j} + \alpha_{1j} x_{ij} + \epsilon_{ij} \quad 5.12$$

$$\alpha_{0j} \sim N\left(0, \sigma^2_{\alpha_0}\right) \quad 5.13$$

$$\alpha_{1j} \sim N\left(0, \sigma^2_{\alpha_1}\right) \quad 5.14$$

$$\epsilon_{ij} \sim N(0, \sigma_{\epsilon}^2) \quad 5.15$$

Where the added term to equation **5.12** is the normally distributed random slope α_{1j} with variance of $\sigma_{\alpha_1}^2$. The application of equation **5.12** is shown in Figure 5-12.d.

Our main focus in this work is extracting the general fixed effect slopes, and the corresponding activation energies of the different states of the electrical evolution. We thus use the conditional ordinary R_o^2 statistics that captures both the fixed and random response for comparison measure of the different LMMs as follows:

$$R_o^2 = 1 - \frac{SSE}{SST} \quad 5.16$$

$$SST = SSR + SSE \quad 5.17$$

$$SSR = \sum(F_i - \bar{F})^2 \quad 5.18$$

$$SSE = \sum(y_i - F_i)^2 \quad 5.19$$

Where SSE is defined as the sum of squared conditional residuals, y_i represents the ith response value and F_i denotes the fitted conditional response. SSR is calculated as the sum of squared deviations between the fitted values F_i and the mean of the fitted values $\bar{F}$. Last, SST corresponds to the total sum of squares.

Table III presents the fixed effects obtained from the LMM Arrhenius fits with random intercepts and random slopes. As discussed in section 5.5, stages three and five are associated with thick binder burnout and LMP melting, respectively. Notably, the activation energies in Table 5-3 for stages three and five are considerably higher compared to those of stage four, which corresponds to thin binder burnout and the

broadening of the existing electrical percolation network. For the third stage, the activation energies are 88.48, 139.36, and 328.51 $kJ \cdot mol^{-1}$ for test combinations AI9, BI9, and CI9, respectively. This increase in activation energy aligns with the elevated temperatures at which stage three takes place. A similar trend can be observed for the third stage between the test combinations AS9 and BS9, with activation energies of 106.03 and 197.42 $kJ \cdot mol^{-1}$, respectively.

Table 5-3: Fixed effects using random intercept and slope LMM for the Arrhenius relationships for stages 3, 4 and 5 for the different test combinations.

Combination		Stage III	Stage IV	Stage V
$\boldsymbol{AI9}$	$T\ /°C$	120-140	140-150	150-155
	$E_a\ /kJ\ mol^{-1}$	88.5 (71.8, 105.1)	19.3 (16.7, 21.8)	82.2 (72.4, 92)
	$Ln(\sigma_0\ /\sigma\ cm^{-1}\ )$	82 (68.1, 95.9)	22.4 (20.4, 24.3)	73.8 (65.8, 81.7)
	R_0^2	0.91	0.95	0.99
$\boldsymbol{BI9^a}$	$T\ /°C$	150-185		
	$E_a\ /kJ\ mol^{-1}$	139.4 (130.5, 148.2)		
	$Ln(\sigma_0\ /\sigma\ cm^{-1}\ )$	105 (98.3, 111.6)		
	R_0^2	0.91		
$\boldsymbol{CI9^b}$	$T\ /°C$	170-190	190-285	
	$E_a\ /kJ\ mol^{-1}$	328.5 (275.6, 381.4)	27.3 (24.8, 29.8)	
	$Ln(\sigma_0\ /\sigma\ cm^{-1}\ )$	182.5 (152.8, 212.2)	17 (16, 18.1)	
	R_0^2	0.81	0.98	
$\boldsymbol{AS9}$	$T\ /°C$	110-135	155-220	220-230
	$E_a\ /kJ\ mol^{-1}$	106 (99.2, 112.9)	6.2 (6, 6.4)	133.5 (122.6, 144.4)
	$Ln(\sigma_0\ /\sigma\ cm^{-1}\ )$	103.8 (97.8, 109.8)	12.1 (12, 12.2)	80.6 (74.7, 86.5)
	R_0^2	0.95	0.98	0.97
$\boldsymbol{BS9}$	$T\ /°C$	170-180	190-220	225-230
	$E_a\ /kJ\ mol^{-1}$	197.4 (180.1, 214.7)	3.7 (3.6, 3.9)	148.9 (116.8, 180.9)
	$Ln(\sigma_0\ /\sigma\ cm^{-1}\ )$	138.2 (126, 150.4)	10.7 (10.6, 10.8)	88.6 (71.5, 105.8)
	R_0^2	0.89	0.91	0.95
$\boldsymbol{CS9^c}$				

AI3	$T\ /°C$	80-120	120-145	145-155
	$E_a\ /kJ\ mol^{-1}$	103.5 (83.7, 123.2)	10.8 (9.6, 12)	73.2 (67, 79.4)
	$Ln(\sigma_0\ /\sigma\ cm^{-1}\ )$	117.2 (99.1, 135.3)	16.5 (15.6, 17.5)	67.9 (62.9, 73)
	R_0^2	0.88	0.98	0.96
AS3	$T\ /°C$	100-120	150-220	220-230
	$E_a\ /kJ\ mol^{-1}$	85.7 (77.9, 93.4)	3.8 (3.6, 4.1)	106.8 (93.9, 119.7)
	$Ln(\sigma_0\ /\sigma\ cm^{-1}\ )$	93.7 (84.6, 102.8)	10.6 (10.5, 10.8)	66.1 (59.2, 73)
	R_0^2	0.91	0.99	0.96

[a] Goes from stage 3 directly to stage 6
[b] Does not show a clear transition to stage 5
[c] Stages overlap

5.7 Conclusion

In this study we systematically investigated the electrical and structural formation of Ag-based TLPS paste materials. Different paste and processing combinations were examined, including various organic binders, alloying elements (In and Sn), and heating rates. The material characterization was carried out through in-situ electrical measurements of these combinations. Through our findings, we were able to divide the electrical and structural evolution into six different stages that occur during the heating of the paste samples. The electrical conductivity of the material begins through the formation of an electrical percolation network during the evaporation of the organic binder, which improves further during the melting of the LMP. The importance of achieving a uniform capillary state was demonstrated, and the pitfalls of insufficient and timely removal of the organic binder were highlighted. The rapid formation of the structural backbone of the TLPS paste material, which is highly

beneficial for rapid and robust AM applications, was also presented. Furthermore, LMMs were used to extract the activation energies of the different evolution states for the different test combinations. The findings can guide future research in the formulation of the paste, processing conditions, and alloying element selections. Future research should focus on investigating the effects of different particle sizes and distributions of HMP and LMP particles, different LMP to HMP ratios, and different ambient conditions to further understand the cross effects that take place during the initial processing of the TLPS material.

6 SIMMULATION AND MODELING

This chapter concentrates on reproducing the electrical findings from chapter 5. It starts by establishing a modeling framework for composite materials, specifically the TLPS, with a case-study of the Cu-Sn TLPS system. The second part of this chapter further develops the modeling and simulation framework to achieve a more accurate representation of the material during the early processing stage, aligning with the objectives of this work.

6.1 Overview on TLPS Used for Case-Study Simulation and Modeling

For an arbitrary binary system, TLP is a type of sintering process in which metal A (filler metal) melts and diffuses into metal B (base metal) while the base metal remains in a solid phase throughout the entire process. The liquid phase gradually consumes (hence the term transient), solidifies isothermally ($\Delta T = 0$) until no liquid remains [182], and creates either solid solution or Inter IMC, depending on the choice of metals [152]. This process is different from traditional sintering process in which the diffusion is done by mass transport (several diffusion modes and creep) without reaching the melting point of any of the metal participants. The TLP sinter process also differs from brazing (hard soldering), as the applied temperature that is used to melt the filler metal is lower and kept below 450˚C. It also differs from welding as it allows to join two different base metals. Two prerequisites for a successful binary TLPS process and bonding between the metals are mutual solubility (as in solid solution) or reactivity

(as in IMC), and sufficient wettability of the solid phase by the liquid phase [152].

The main advantage of the TLPS material is the ratio between the processing temperature and the operational temperature. The TLPS is processed with temperature below 300˚C and above the melting temperature of the lower-melting temperature metal, such as Sn with $T_{m\text{-}low}$ of 231.9°C. After the processing is completed and the different phases of IMC have formed, the resultant melting temperature of the TLPS material will then be much higher, and will shift towards the melting temperature of the second participant metal, such as Cu with $T_{m\text{-}high}$ of 1,085°C.

In some TLPS Metal Matrix Composite (MMC) systems, materials may exhibit, excessive voiding, stiffness and brittleness, as well as high raw material price (depends on the metal system), and long processing time. These disadvantages are rather general and should be further addressed to a specific metal binary/tenantry TLPS system.

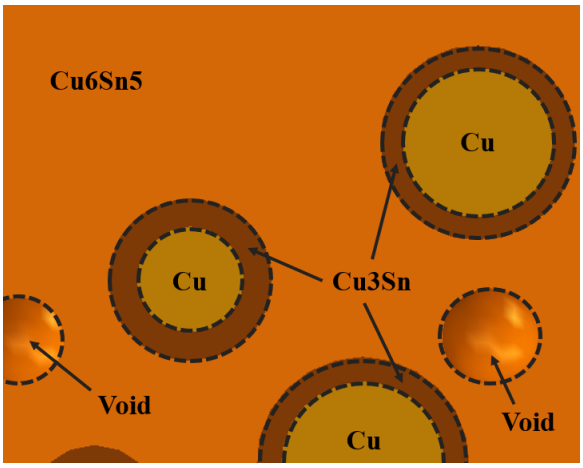

Figure 6-1: Illustration of a Cu-Sn microstructure TLPS MMC system.

The microstructure of the Cu-Sn TLPS MMC system under study is shown in Figure 6-1. In such system, when Cu and Sn are mixed and sintered under 300°C, two

primary IMCs will develop: Cu6Sn5 (matrix phase) and Cu3Sn (transition phase). Initially, Cu particles (aggregate phase) will react with Sn particles to form the Cu6Sn5 while consuming the Cu and Sn atoms. Thereafter, following a further aging process, Cu3Sn will develop around the Cu particles by consuming the Cu atoms and by transforming some of the Cu6Sn IMC phase. During this process, voids form through several mechanisms such as: reduction of volume due to increased density of the TLPS, Kirkendall effect due to differences in diffusion rates, and evaporation of the organic flux [152]. The isotropic material properties that were used for this study are shown in Table 6-1.

Table 6-1: Isotropic elastic material properties of Cu-Sn TLPS phases.

	Cu	**Cu3Sn**	**Cu6Sn5**
Density [kg/m^3]	8890.0	8900.0	8280.0
Elastic Modulus [GPa]	119	108.3	85.56
Poisson's Ratio	0.34	0.299	0.23
CTE [ppm/°C]	17.0	19.0	16.3
Thermal Conductivity [W/mK]	385.0	70.4	34.1

6.2 Modeling Composites Materials

In micro- and nano-scales, most materials will show some level of heterogeneity in the form of grain boundaries, cracks, voids, inclusions, and other material defects. However, for most practical applications and simulations, effective (macro) material properties are required. Through homogenization (averaging) techniques, it is possible to calculate these effective material properties. Analytical methods and finite element methods are such homogenization techniques. While the first approach is useful and effective for some applications, it lacks sufficient level of

detail, and often depends on some set of assumptions. On the other hand, finite element simulations are capable of simulating detailed structures and systems. The main drawback of finite element simulations is the large computational cost.

To optimize the use of finite element simulations of composite materials, models assume periodicity of the geometry and boundary conditions. These two assumptions enable to shrink the size of the finite element model and achieve the same effective material properties as a full-size model. Furthermore, the reduction of model size, and therefore the reduction of computing cost, allows to simulate detailed models with minimal geometry assumptions or simplifications. According to Hori et al., the choice of periodic boundary conditions over homogenous strain or stress boundary conditions, have proven to be the most accurate, as the two other boundary conditions overestimate or underestimate the effective properties of the material [183].

In this work, only periodic boundary conditions were used. Models with periodic geometry are still under development. To overcome the lack of true periodic geometry, larger sized test models were generated to achieve the necessary statistical representation. The model was then tested and validated against a stochastic model [184] which uses a different technique to solve for the effective properties.

The use of periodicity requires the development of a Representative Volume Element (RVE). The RVE must statistically represent the considered material volume and the local continuum properties [185]. Regardless of the presence of periodicity in the microstructure, the requirement of the RVE is to have a ratio of $D/d >> 1$, where D

is the dimensions of the RVE and d is the size of the smallest inclusion of interest. The optimum choice of RVE size would be one that includes the largest amount of detail of direct influence on the macro properties, while maintaining the simplest or smallest model.

Once the RVE with a volume V_{RVE} is obtained, the extraction of an arbitrary macro material property can be done by the following equation:

$$\langle T \rangle = \frac{1}{V_{RVE}} \int_V T(\boldsymbol{x}) dV \qquad 6.1$$

Where T($\boldsymbol{x}$) is an arbitrary micro property, $\langle T \rangle$ is the corresponding macro property, and $\boldsymbol{x}$ is an orthogonal position vector. For the same RVE, any spatial field such as temperature field or displacement field needs to feature periodicity. The periodic displacement field for example, can be expressed as:

$$u_i(\boldsymbol{x}) = \langle \varepsilon \rangle_{ij} \boldsymbol{x}_j + u_i^*(\boldsymbol{x}) \quad i \; and \; j = 1,2 \; or \; 3 \qquad 6.2$$

Where $u_i(\boldsymbol{x})$ is the spatial displacement field, $\langle \varepsilon \rangle_{ij}$ is a second order tensor of the macro strain, and $u_i^*(\boldsymbol{x})$ is a periodic function that represents the small displacement perturbations due to the heterogeneities at the micro scale. By the definition of periodicity, these perturbations are similar for neighboring RVEs [186]. Equation **6.2** implies that the overall macro body, as a collection of small identical RVEs, will maintain a displacement continuity, and as a result, traction continuity. These two continuities ensure that after the body deforms due to any sort of loading, the material will not overlap.

Since $u_i^*(\boldsymbol{x})$ is generally an unknown quantity, equation **6.2** cannot be applied directly as a boundary condition. However, the displacement on two opposite sides of an RVE can be written as:

$$u_i^{k+}(\boldsymbol{x}) = \langle\varepsilon\rangle_{ij}\boldsymbol{x}_j^{k+} + u_i^*(\boldsymbol{x}) \quad k = 1,2\ or\ 3 \tag{6.3}$$

$$u_i^{k-}(\boldsymbol{x}) = \langle\varepsilon\rangle_{ij}\boldsymbol{x}_j^{k-} + u_i^*(\boldsymbol{x}) \tag{6.4}$$

Where k+ and k- represents any two opposite faces of the RVE and $u_i^*(\boldsymbol{x})$ is the same in both equations due to periodicity. Taking the difference between equation **6.3** and equation **6.4** yields:

$$u_i^{k+}(\boldsymbol{x}) - u_i^{k-}(\boldsymbol{x}) = \langle\varepsilon\rangle_{ij}(\boldsymbol{x}_j^{k+} - \boldsymbol{x}_j^{k-}) = \langle\varepsilon\rangle_{ij}\Delta\boldsymbol{x}_j^k \tag{6.5}$$

For each pair of the opposite sides of the RVE, $\Delta\boldsymbol{x}_j^k$ is constant, and $\langle\varepsilon\rangle_{ij}$ is a known applied strain. The right-hand side of equation **6.5** then becomes constant, and can be applied as a displacement boundary condition in FE simulations. For linear elastic analysis, equation **6.5** also guarantees the traction continuity [187].

For an arbitrary small applied displacement, the effective strain and stress can be obtained by using equation **6.1** as follows:

$$\langle\sigma\rangle_{ij} = \frac{1}{V_{RVE}}\int_V \sigma(\boldsymbol{x})dV \tag{6.6}$$

$$\langle\varepsilon\rangle_{ij} = \frac{1}{V_{RVE}}\int_V \varepsilon(\boldsymbol{x})dV \tag{6.7}$$

Where $\langle\sigma\rangle_{ij}$ and $\langle\varepsilon\rangle_{ij}$ are second order tensors of the effective stress and strain respectively. $\sigma(\boldsymbol{x})$ and $\varepsilon(\boldsymbol{x})$ are the corresponding stress and strain fields throughout the

selected RVE. Using these two effective properties, it is then possible to solve for the full effective symmetric stiffness $\langle C \rangle_{ijkl}$ forth order tensor by using the generalized Hooke's law:

$$\langle \sigma \rangle_{ij} = \langle C \rangle_{ijkl} \langle \varepsilon \rangle_{ij} \quad 6.8$$

By obtaining the coefficients of the stiffness matrix, it is then possible to use them in any macro level simulations and analysis. In cases when the stiffness matrix features some symmetric characteristics, such as in isotropic material or orthotropic material, taking the inverse of the matrix, which will yield the compliance forth order tensor $\langle S \rangle_{ijkl}$, will output some directional or isotropic material constants such as elastic modulus and Poisson's ratio.

With the same approach of extracting the effective mechanical properties from a periodic model, the effective thermal conductivity second order symmetric tensor, $\langle \kappa \rangle_{ij}$, can be calculated with the following relationship:

$$\langle \kappa \rangle_{ij} = -\langle q \rangle_i / \nabla T_j \quad 6.9$$

Where: $$\nabla T_j = \Delta T / L_j \quad 6.10$$

With the periodic temperature condition:

$$T^{k+} - T^{k-} = \Delta T \quad 6.11$$

Where $\langle q \rangle_i$ is the effective heat flux in the ith direction, ∇T_j is the temperature gradient along the jth direction, ΔT is the applied macro temperature difference, L_j is the respective RVE's length, and T^k is the temperature on the kth face of the RVE. For

a given applied temperature change, the effective thermal flux can be calculated by applying equation **6.1**:

$$\langle q \rangle_i = \frac{1}{V_{RVE}} \int_V q(x) dV \qquad 6.12$$

Where $q(\boldsymbol{x})$ is the micro heat flux field in the RVE. Analogously to the displacement field and traction continuities, when a change in temperature is applied to an RVE, the temperature and heat fluxes must maintain continuity on opposite faces of the RVE.

Finally, the Thermal Expansion Coefficient (CTE) can be calculated by applying a change in temperature, and calculating the resultant strain along each of the principle directions as follows:

$$\langle \alpha \rangle_i = \frac{\Delta L_i}{L_i \Delta T} = \frac{\langle \varepsilon \rangle_i}{\Delta T} \qquad 6.13$$

Where $\langle \alpha \rangle_i$ is the effective CTE in the ith direction, and the effective strain $\langle \varepsilon \rangle_i$ is calculated according to equation **6.8** [188].

6.2.1 Methods of Preparing the Model

The first step of building the RVE of the Cu-Sn TLPS microstructure is generating randomly distributed particles' coordinates. This step was done by writing a Matlab code that ensures that the particles do not overlap with each other or cross the boundaries of the RVE. In addition, the Matlab code allows the user to choose a minimum distance between the particles, size of the transition phase, and control over the desired volume fraction of the phases and voiding. The minimum distance

parameter is important to ensure the quality of the mesh and was chosen to be two units of length.

Through the FE software Abaqus, a python code was written to: read the Matlab files with the coordinates of the particles, apply mesh and boundary conditions, define interactions between the particles and the matrix, define relationship between groups of nodes to ensure periodicity, run the desired tests, and output the desired results.

The interaction between the particles and IMC phases were assumed to have perfect bonding, and were defined in the python code by using Tie Constraints. To ensure periodicity of the model, the code generates reference points (RP_i for i = 1,2 or 3) that can be defined as the right-hand side of equation **6.5** or equation **6.11**, the applied displacement or temperature difference. The code then finds pairs of nodes on opposite faces, and groups them with the appropriate reference points. To avoid over constrained model, this step requires to have three groups of nodes pairs: vertices nodes, edge nodes, and face nodes. The full derivation of the periodic part of the code can be found in [189], which also provides python script to help apply the periodic conditions.

Table 6-2: Applied boundary conditions for stiffness tensor calculations

Load Case	$u(\boldsymbol{x})_{RPx}$	$u(\boldsymbol{x})_{RPy}$	$u(\boldsymbol{x})_{RPz}$
Tension - xx	(δ, 0, 0)	(0, 0, 0)	(0, 0, 0)
Tension – yy	(0, 0, 0)	(0, δ, 0)	(0, 0, 0)
Tension – zz	(0, 0, 0)	(0, 0, 0)	(0, 0, δ)
Shear - xy	(δ/2, 0, 0)	(0, δ/2, 0)	(0, 0, 0)
Shear – xz	(0, δ/2, 0)	(0, 0, 0)	(0, 0, δ/2)
Shear - yz	(0, 0, 0)	(0, δ/2, 0)	(0, 0, δ/2)

The boundary conditions were divided into three groups of tests to solve for each of the effective material properties: the effective stiffness matrix, the effective

CTE vector, and the effective thermal conductivity matrix. To calculate the full effective stiffness tensor, six monotonic tests were applied: three pure tension tests along the principle axis, and the corresponding three pure shear tests as shown in Table 6-3. The applied displacement δ was chosen to be small enough to ensure linear elastic response. In all of the tests, one corner node was completely constrained in all directions to prevent rigid body translation.

For each one of the load cases, the python code extracted the full effective stress and strain tensors, which then allowed to solve for one respective row of the effective stiffness tensor by following equation **6.8**.

The applied boundary condition for calculating the effective CTE was a field temperature change of $\Delta T = 10°C$ across the entire RVE. The RVE was allowed to expand in all directions while maintaining periodicity. Similar to the effective stiffness matrix calculations, one corner node was completely constrained in all directions to prevent rigid body translation.

Last, to calculate the full effective thermal conductivity matrix, three different tests were applied to the RVE as shown in Table 6-3.

Table 6-3: Applied boundary conditions for thermal conductivity tensor calculations, where ΔT = 100°C.

Load Case	$T(\boldsymbol{x})_{RPx}$	$T(\boldsymbol{x})_{RPy}$	$T(\boldsymbol{x})_{RPz}$
ΔT – xx	(ΔT, 0, 0)	(0, 0, 0)	(0, 0, 0)
ΔT – yy	(0, 0, 0)	(0, ΔT, 0)	(0, 0, 0)
ΔT – zz	(0, 0, 0)	(0, 0, 0)	(0, 0, ΔT)

According to Moghaddam at el., periodic models are susceptible of being predictable, and hence a stochastic model which is more statistically rigorous and capable of considering parametric uncertainty is required [184]. To validate the accuracy of the current model, the generated geometry was slightly altered to enable reproduction of the stochastic model and the results are shown in Appendix I. The averaged percent change between the stochastic model and the current model for the elastic modulus, Poisson's ratio, and CTE were found to be 2.519%, 7.284%, and 0.239% respectively. These values were considered reasonable to validate the current model. Deviation in results might occur due to differences in particle' sizes, exact particles distribution, and volume fraction of the particles from model to model.

The next step of preparing the model was to validate that the particle distribution is indeed random and that the model exhibits isotropic behavior without bias in any direction. This can be validated by looking at the stiffness and thermal conductivity tensors of arbitrary tests. For the stiffness tensor, if the off diagonal values of the forth, fifth, and sixth rows and columns are few orders of magnitude smaller than the rest of the values, it is reasonable to assume that the material is isotropic. For example, equation **6.14** shows the stiffness tensor for a Cu-Sn system with 12% voiding (values are times 1E+10):

$$\langle \mathbf{C} \rangle = \begin{bmatrix} 12.20 & 5.111 & 5.101 & -.002 & -.002 & -.003 \\ 5.111 & 12.207 & 5.099 & -.005 & -.001 & -.015 \\ 5.101 & 5.099 & 12.201 & -.002 & -.001 & -.009 \\ -.002 & -.005 & -.002 & 3.452 & -.002 & -.001 \\ -.002 & -.001 & -.001 & -.002 & 3.450 & -.002 \\ -.003 & -.015 & -.009 & -.001 & -.002 & 3.449 \end{bmatrix} \quad 6.14$$

The last step of preparing the model was to optimize the size of the RVE. This step is done by running multiple simulations with similar percentage of particles phases and voiding, while increasing the volume of the RVE as shown in Figure 6-2:

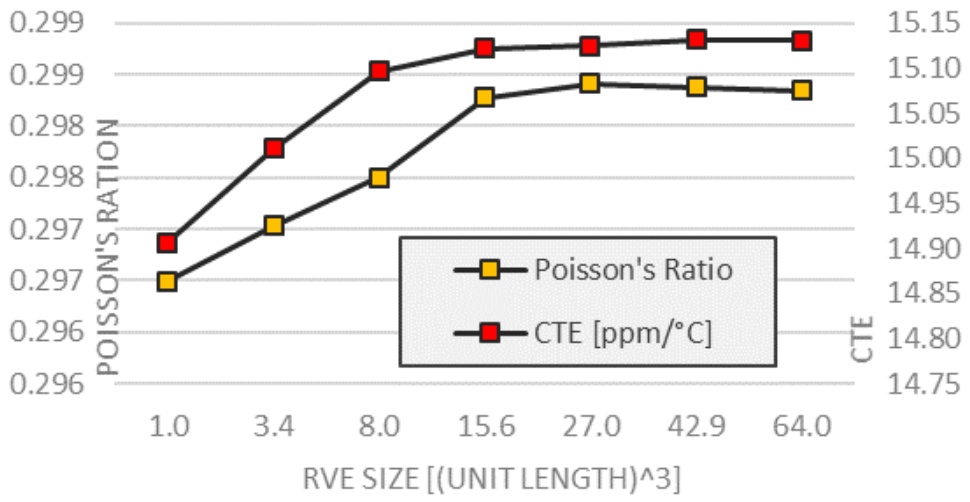

Figure 6-2: Effective Poisson's ratio and CTE vs. RVE size.

6.2.2 Results and Discussion

Based on the studies that show the phase evolution of the Cu-Sn TLPS material [39,187], the model was used to exhibit the effective properties accordingly. Figure 6-3 show the effective properties with respect to phase evolution. When the Cu6Sn5 is starting to evolve on the expense of Cu atoms, the elastic modulus

experiences a relative significant decrease. The rest of the properties are decreasing as well. When the Cu3Sn is starting to evolve, at the beginning mostly on the expense of Cu atoms, the elastic modulus, CTE, and thermal conductivity are increasing while the Poisson's ratio keeps decreasing. At the end, when the Cu particles are completely consumed due to ageing, when the Cu6Sn5 transforms to Cu3Sn, the elastic modulus and CTE are increasing, while the Poisson's ration keeps decreasing. The thermal conductivity shows no significant change in value. While for some effective properties such as the CTE the trend due to the phase evolution can be seen clearly, for other properties the behavior seems to depend on several parameters, and further investigation has to be done to isolate the influence of each of the IMC phases and their combinations.

Another set of simulations were conducted to show the effect of void content while the rest of the phases maintain the same volume percentage as shown in Figure 6-4.

A.

B.

C.

D.

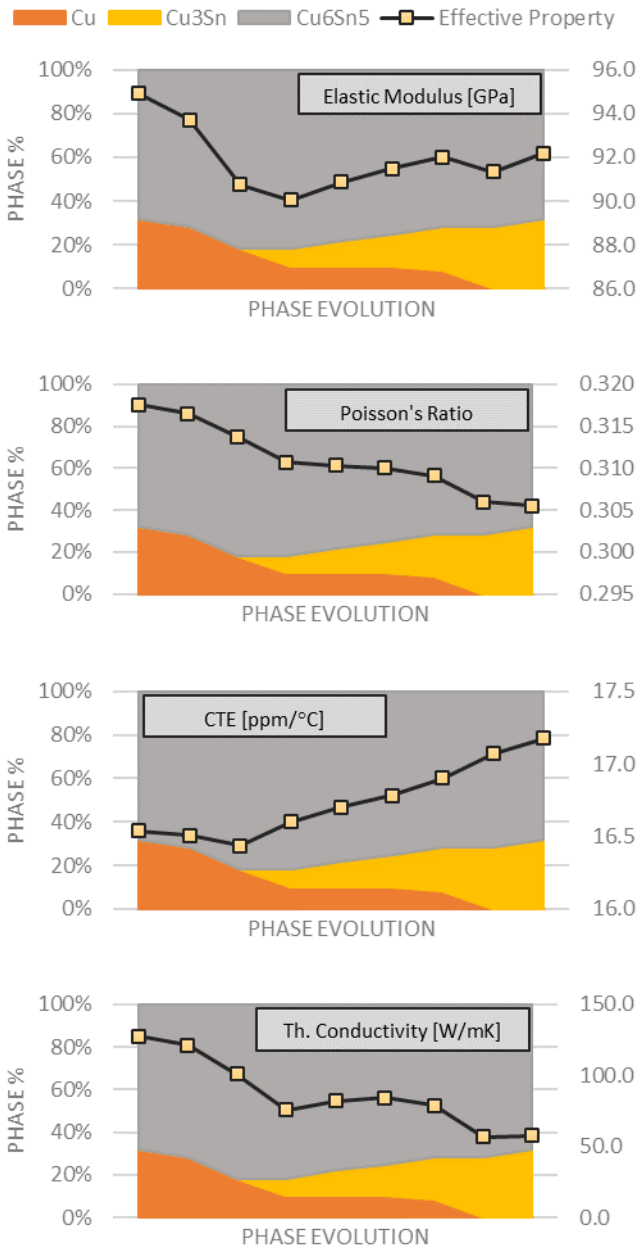

Figure 6-3: Shows the effective elastic modules, Poisson's ratio, CTE, and thermal conductivity vs. phase evolution due to aging process.

The influence of monotonic increase in void content can be seen clearly as each of the effective properties increases or decreases monotonically as well. With increased

void content, the elastic modulus is increasing, while the Poisson's ratio, CTE, and thermal conductivity are decreasing. The graphs in Figure 6-4 assumes constant size of voids which when altered, might have a second order influence on the effective properties.

6.2.3 Conclusion for establishing TLPS MMC modeling and simulation

In this first part of this chapter, a comprehensive method of evaluating effective material properties of heterogeneous media was presented. The method includes the use of periodic boundary conditions through full coupling of the RVE model. With previous knowledge of the microstructure evolution of Cu-Sn TLPS material, the model was used to predict the effective properties of such MMC system such as the elastic modulus, Poisson's ration, CTE, and thermal conductivity. In future, the model will be tested against real experiment for further validation and better predictions. In addition, the model will be utilized to investigate additional TLPS alloys. Development of full periodic geometry is still necessary to satisfy the full mathematical derivation of periodic media.

A.

B.

C.

D.

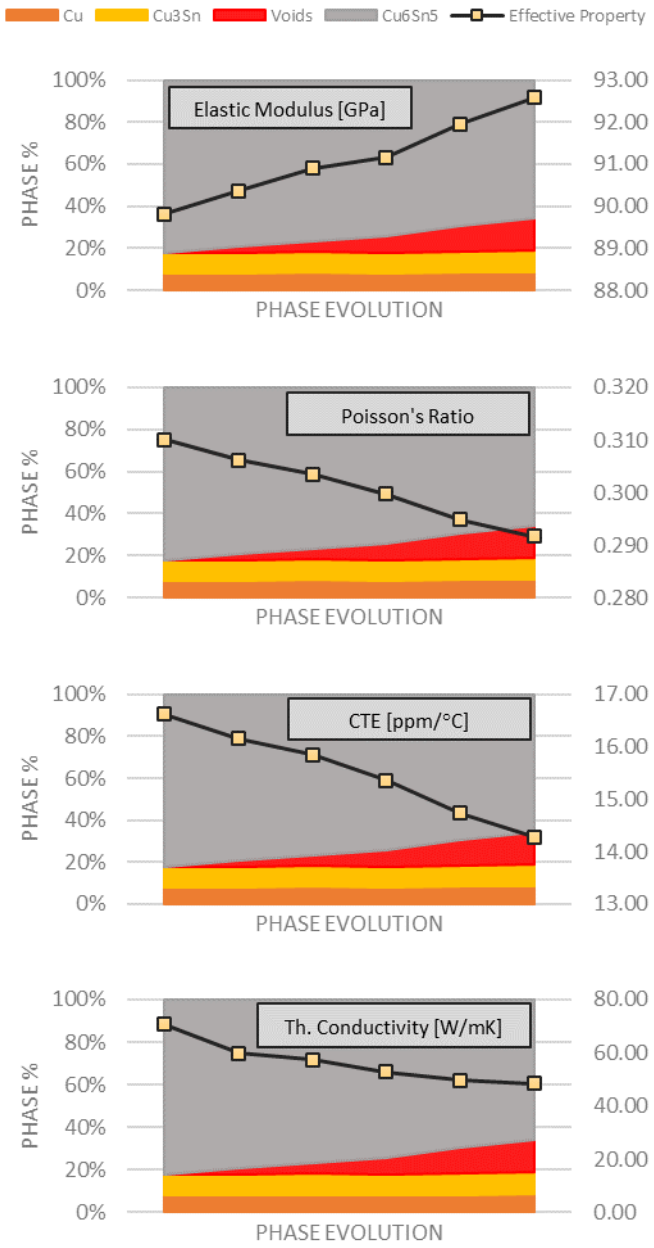

Figure 6-4: Shows the effective elastic modulus, Poisson's ratio, CTE, and thermal conductivity vs. increased void content while maintaining constant volume fraction of the Cu and Cu3Sn phases.

6.3 Electrical percolation simulation and modeling

This section advances the existing modeling and simulation framework of MMC TLPS materials. It enhances the geometric generation of the TLPS system by implementing several improvements. These enhancements encompass the integration of periodic 3D geometry, enhanced control over particle distribution generation, accommodation for contacting spheres, simulation of contact resistance and flux residue, geometric representation of liquid bridges, and validation of in-situ electrical test outcomes.

6.3.1 Periodic Geometry

Macroscopic objects with micro or meso-scale characteristics pose challenges for practical modeling. To address this, a representative volume element is often employed. When geometry can be condensed into a consistent repeatable shape, the RVE is defined as a unit cell. In scenarios where micro and meso-scale features are random, the RVE must embody a statistically significant material sample. The distinction between a unit cell and a statistical RVE is shown in Figure 6-5.

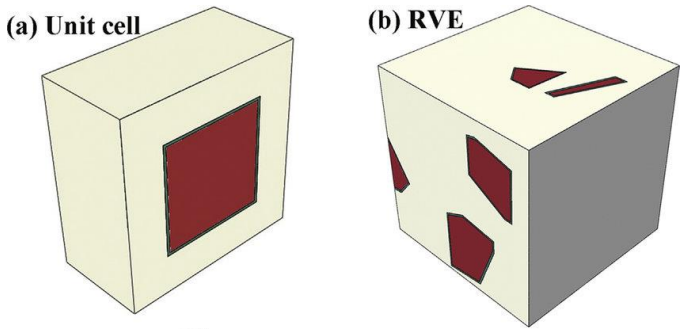

Figure 6-5: Shows the difference between a unit-cell RVE (a), and a statistical-based RVE (b) [190]**.**

The utilization of a unit cell proves beneficial when it reliably replicates actual experimental material and outcomes. Unlike the statistical RVE, the unit cell can be simplified in terms of size and complexity, leading to easier generation and reduced computational cost. However, situations often arise where unit cell simplification falls short of reproducing experimental results, necessitating a randomized statistical-based RVE. The minimum size of such a statistical RVE is often determinable when the calculated property approaches an asymptotic value, as previously illustrated in Figure 6-2. Notably, the RVE in Figure 6-2 was not established based on periodic geometry, which inherently results in larger RVEs to counteract edge effects and achieve statistically significant outcomes. Furthermore, studies have shown that edge effects can exert negative influences on results. To mitigate edge effects and enable higher inclusion volume fractions, a periodic geometry was incorporated, as shown in Figure 6-6.

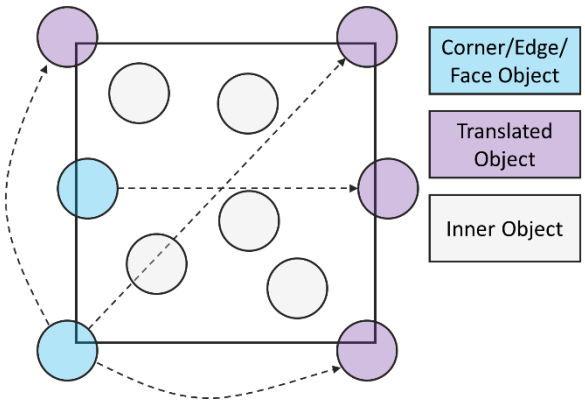

Figure 6-6: 2D representation of a periodic geometry RVE with edges and corners. This illustration can be further extended to 3D representation in which the RVE has faces, edges, and corners.

Similar to non-periodic geometry, the coexistence of two randomly generated overlapping objects is precluded due to inherent physical infeasibility. Moreover, an enhancement introduced in the present section pertains to the inclusion of admissible interactions among touching particles. This augmentation serves to facilitate the simulation of contact resistance and electrical percolation phenomena. Accordingly, particle objects in proximity or surpassing a designated threshold distance, calculated as follows:

$$\left\|position_i - positions_{1:(i-1)}\right\| \leq radius_i + radius_{1:(i-1)} + Dist_{threshold} \quad 6.15$$

Here, $position_i$ represents the current randomly generated particle with a corresponding radius donated as $radius_i$. This particle is tested against all other particles with positions $positions_{1:(i-1)}$ and radii $radius_{1:(i-1)}$. The parameter $Dist_{threshold}$ designates the threshold distance, which assumes a non-negative value greater than or equal to zero.

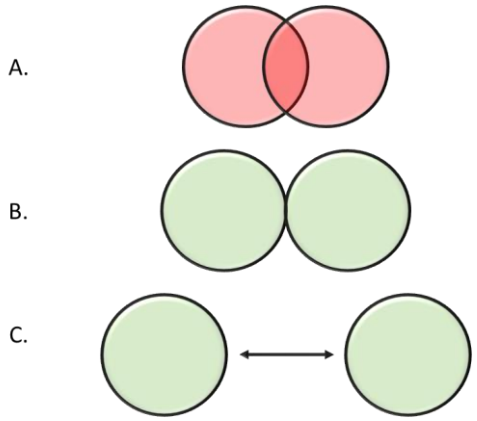

Figure 6-7: Unsatisfied positional constraint (a). Satisfied positional constraints (b,c).

These principles are visually represented in Figure 6-7 and are universally applicable to all particles subjected to translation. In the event that any of these principles are violated by any translated particle, it becomes imperative to discard the entire ensemble of translated particles, inclusive of the original constituent.

6.3.2 Procedure for Generating Experimentally-Based Periodic Geometry

In order to enhance simulation accuracy and verification procedures, an ideal scenario involves generating geometry that perfectly mirrors the actual physical material utilized in experimental settings. Drawing insights from the depicted particle distribution in Figure 5-1, the process of modeling the geometry necessitates the generation of a log-normal distribution. The conventional approach of sequentially introducing particles, as employed in prior sections, proves inadequate for attaining a log-normal particle distribution, often leading to geometries with notably diminished volume fractions.

In accordance with measured experimental data that shown in Figure 5-4, the targeted volume fractions are approximately 70 to 80%, constituting a packing density of conductive spherical particles. A critical challenge associated with adapting sequential addition for log-normal particle distribution lies in the rapid saturation of the RVE with smaller particles, predominantly due to their higher likelihood of being added. This leaves insufficient space to accommodate larger particles.

To address this, a modification to the standard sequential addition algorithm has been implemented to facilitate the realization of a log-normal particle distribution. The

modified procedure is shown in Figure 6-8. The altered procedure introduces three primary supplementary parameters: Weight Bias, Reduction Value, and Reduction Cutoff. Initially, a set of radii conforming to the desired log-normal distribution is generated, each assigned a distinct identifier. Subsequently, the selection probability for a given radius from this pool is skewed in favor of larger particles, as indicated by the straightforward relationship:

$$w_i = radius_i \tag{6.16}$$

Here, w_i is the i_{th} bias value for the corresponding i_{th} radius. Naturally, using this relationship, the larger radii result with larger bias values. This bias can be further emphasized by using the following implicit relationship:

$$w_i = w_i^n \tag{6.17}$$

Here, n is an additional parameter that serves as a bias amplifier.

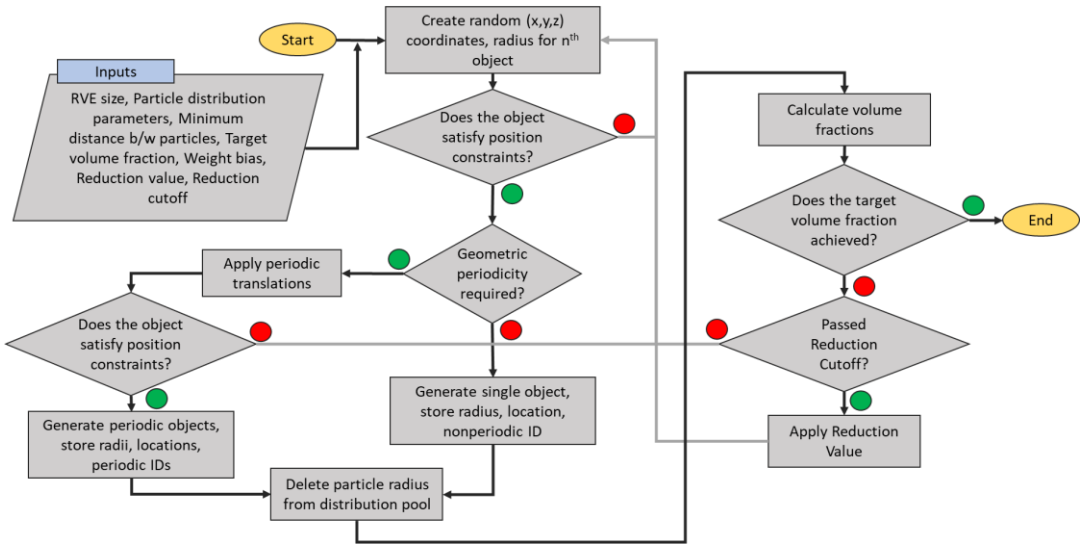

Figure 6-8: Procedure for generating experimentally-based periodic RVE.

To achieve a log-normal particle distribution that faithfully replicates experimental measurements within a reasonable timeframe, the need arises to eventually attenuate or eliminate the applied bias. Consequently, the introduction of the Reduction Cutoff parameter becomes imperative. Upon exceeding this cutoff value in terms of volume fraction, the algorithm incorporates an additional parameter, Reduction Value, during each iteration, yielding the modified relationship:

$$w_i = (ReductionValue) * w_i \quad 6.18$$

Furthermore, as illustrated in Figure 6-8, subsequent to each successful iteration of object integration within the RVE, the corresponding radius is removed from the pool of radii. This procedure expedites computational execution and significantly contributes to improved log-normal distribution outcomes.

Figure 6-9 demonstrates the successful application of the proposed algorithm across two distinct log-normal target distributions. Visual inspection confirms the algorithm's efficacy in achieving congruent distributions. In both scenarios, the RVE assumes dimensions of 100 μm^2.

Examining Figure 6-9, it's evident that the log-normal distribution characterized by parameters μ=0.65 and σ=0.833 necessitated the incorporation of 5622 particles. This enabled the attainment of a volume fraction of 45% alongside an average particle size measuring 2.76 μm. In contrast, the second target distribution, with μ = 1.4 and σ = 0.85, demanded a smaller particle count of 1506. This yielded equivalent volume fraction and a mean particle size of 5.04 μm.

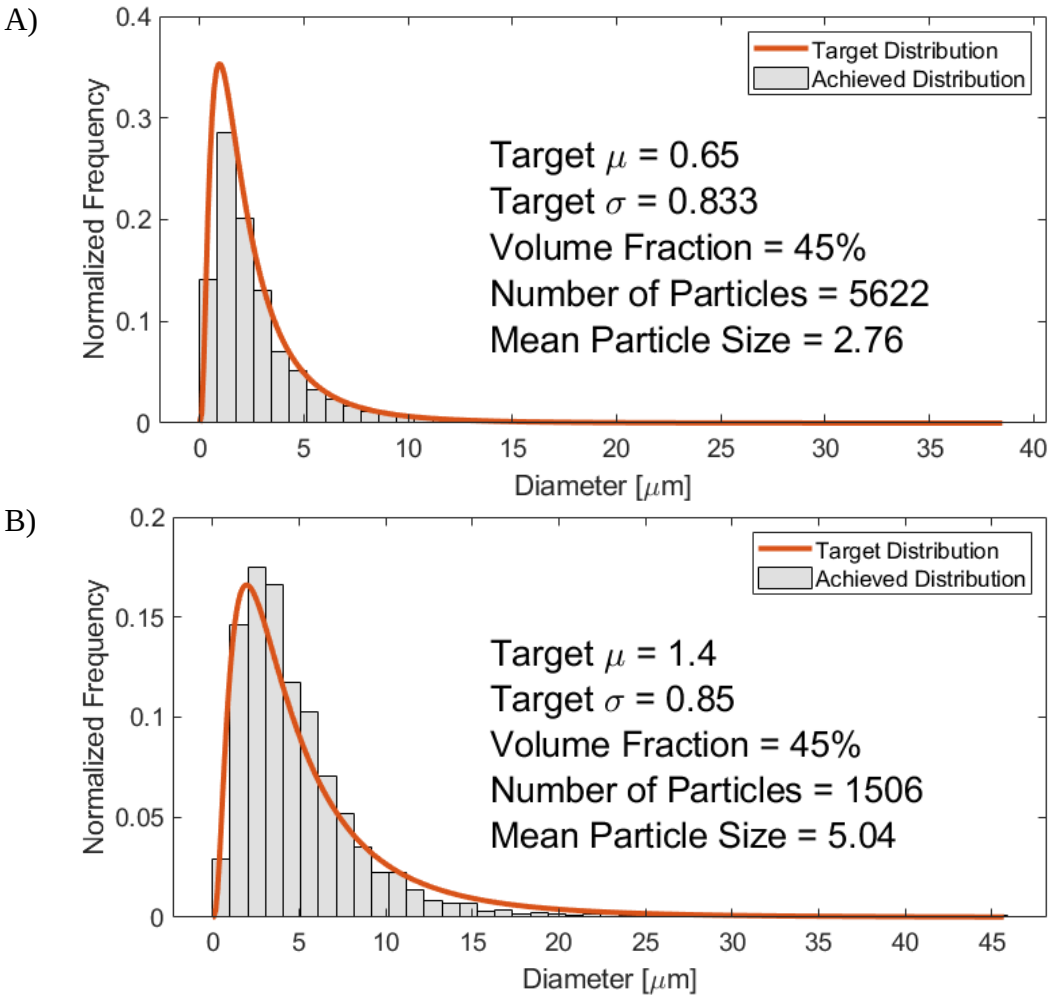

Figure 6-9: Example of target log-normal distributions with two parameters: (a) μ = 0.65 and σ = 0.833, (b) μ = 1.4 and σ = 0.85. The achieved histograms are shown with their respective volume fractions, number of particles, and mean particle size for an RVE with volume of 100 μm^2.

6.3.3 Procedure for Dividing Particle Objects to a Specific Weight Ratio

Following the generation of particles within the RVE, the subsequent step entails assigning them appropriate material attributes in accordance with the predetermined A:B target metal ratio. This ratio selection is typically informed by the underlying experimental configuration; however, it can also function as an adjustable

parameter for computational explorations. The protocol governing the allocation of material properties to the respective particles is elucidated in Figure 6-10.

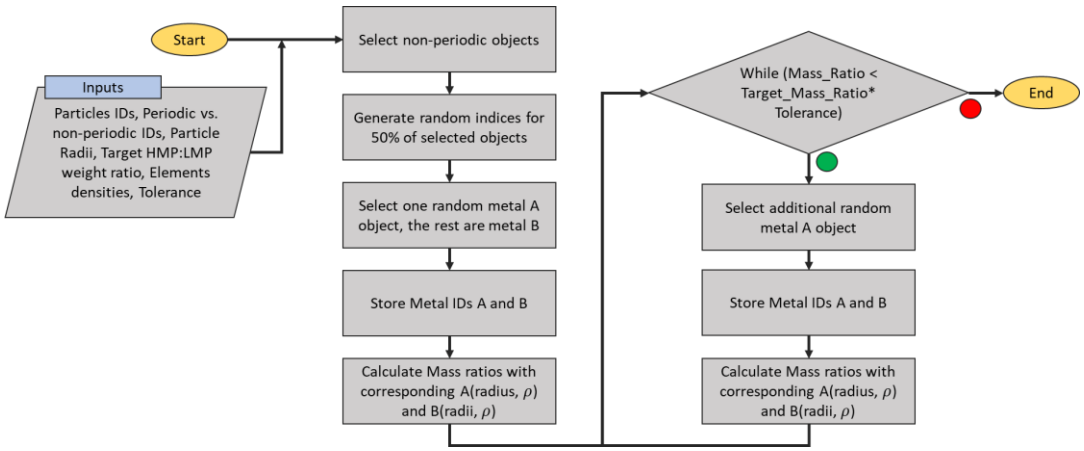

Figure 6-10: Procedure to divide the generated particles into a specific A:B metal ratio.

6.3.4 Voxelating Periodic Geometries and Modeling Contact Resistance

For the purpose of subjecting the RVE to Finite Element Method (FEM) analysis through specialized software (Ansys, Abaqus, etc.), the RVE must undergo a meshing process. A recommended strategy for meshing circular and spherical entities involves utilizing triangle elements for circles and tetrahedra elements for spheres. However, the inherent challenge arises when dealing with objects in close proximity; the sheer number of mesh elements required to bridge the gap between these objects becomes impractical due to computational time and resource constraints.

The problem increases when attempting to accurately simulate percolation networks, intrinsically reliant on the precise modeling of adjacent particle configurations and contact interactions. Addressing this predicament demands a divergent approach. Consequently, the generated geometry is transformed into a

voxelated counterpart, where each voxel corresponds to the 3D equivalent of a pixel in 2D. This technique circumvents the meshing limitations associated with close-proximity particles and facilitates a more viable simulation of percolation phenomena.

Voxelating the geometry presents a major challenge characterized by the inherent loss of information when adopting voxel sizes that are inadequately small. In light of this, for the present study, a deliberate decision was made to define the RVE dimensions as 100 μm^2. Accompanying this choice is the introduction of a log-normal particle distribution that exhibits slight divergence from the experimentally-based particle distribution.

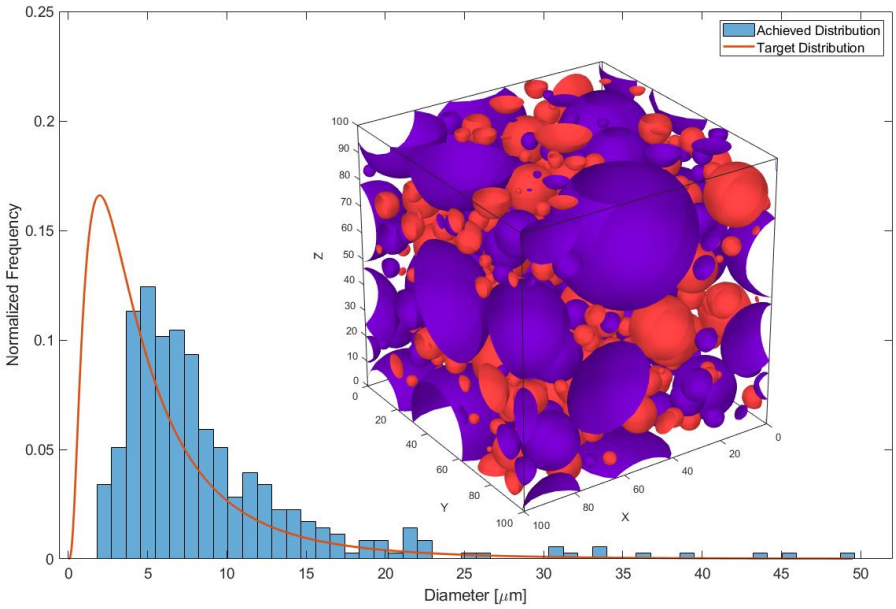

Figure 6-11: Generated adjusted particle distribution RVE with Volume Fraction 73% of conductive particles, with 80:20 distribution between HMP (purple) and LMP (red).

Figure 6-11 exhibits a generated RVE instance, featuring a volumetric fraction of 73% and characterized by an 80:20 distribution between HMP (purple) and LMP

particles (red). This adjustment in how the particles are distributed is aimed at avoiding the problem of having really small particles. Those tiny particles would require too many small voxels for the simulation, making it impractical to carry out.

During the simulation of contact percolation networks, certain parameters are established, such as the electrical conductivity of both HMP and LMP particles. Meanwhile, the electrical conductivity of the organic binder is reasonably assumed to approach an extremely low value, nearly zero [191]. Within the simulation, the principal unknown lies in the effective contact resistance and the presence of oxide layers.

The process involves parameterizing the equivalent contact resistance, which is then subsequently determined based on real experimental outcomes for a specific volume fraction or packing density, as shown in the Figure 6-12. In all simulations, a uniform voxel size of one metric unit was maintained.

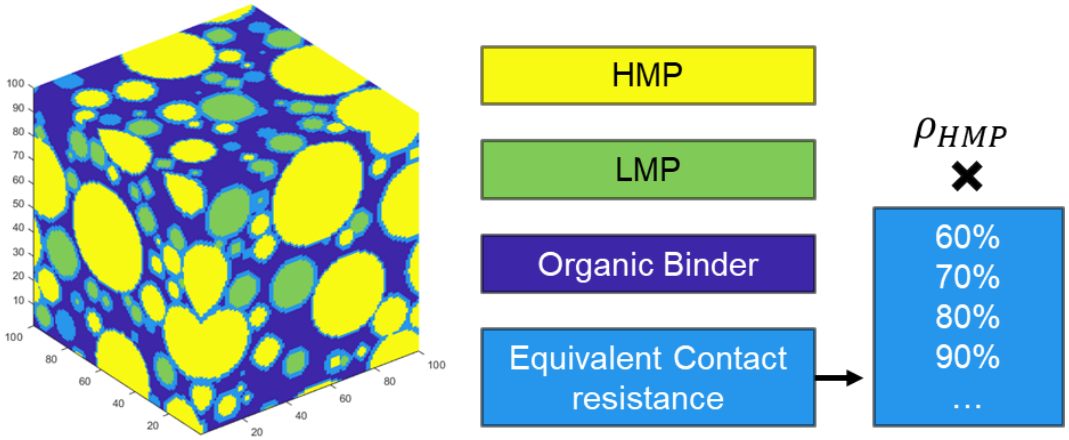

Figure 6-12: Voxelated generated RVE with four phases: HMP, LMP, organic binder, and a parameterized equivalent contact resistance.

6.3.5 Modeling Liquid Bridges

In contrast to conventional percolation models, the scenario within the context of TLPS material necessitates the incorporation of a representation for the liquid bridges that emerge during the melting process of the LMP particles. These liquid bridges are illustrated in detail within Figure 5-8.

In order to replicate the liquid connections observed as molten liquid bridges among solid particles, this investigation employed and integrated a geometry based on weighted quadratic Bezier curves. Bezier curves have been developed to model the inherent curvature of natural shapes and possess the capacity to address the intricate meniscus configurations encountered in capillary formations [192]. The general form of a continuous or discrete weighted Bezier curve encompassing n^{th} points is a parametric expression that can be formulated in the subsequent manner:

$$B(t) = \frac{\sum_i^n b_{i,n}(t) P_i w_i}{\sum_{i=0}^n b_{i,n}(t) w_i} (1-t)^2 \tag{6.19}$$

Where

$$b_{i,n}(t) = \binom{n}{i} t^i (1-t)^{n-i}, i = 0, .., n \tag{6.20}$$

And

$$\binom{n}{i} = \frac{n!}{i!\,(n-i)!} \tag{6.21}$$

Where t is a continuous or discrete parameter. For the weighted quadratic Bezier form with two points and one control point can be represented as follows:

$$b_0 = (1-t)^2 \tag{6.22}$$

$$b_1 = 2t * (1-t) \tag{6.23}$$

$$b_2 = t^2 \tag{6.24}$$

$$B(t) = \frac{b_0 P_0 w_0 + b_1 P_1 w_1 + b_2 P_2 w_2}{b_0 w_0 + b_1 w_0 + b_2 w_0} \tag{6.25}$$

An illustrated reduced 2D implementation of the quadratic Bezier curve between two similar size spheres is shown in Figure 6-13. In the figure, the quadratic Bezier curve is connecting the points D^* and E^*, with a control point at C^*. For simplicity, the size of the vectors AD and BE can be parameterized as a fraction of the corresponding radii of each of the particles. Point C is usually located in the middle point between the edge of the two particles. The height of C^* can be adjusted by changing the weights of the Bezier curve.

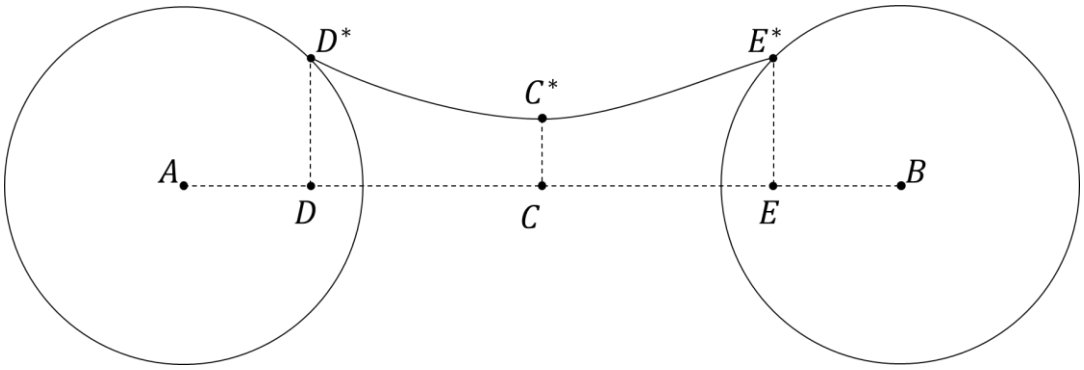

Figure 6-13: Illustrated 2D implementation of quadratic Bezier curve between two points D^* and E^*, with a control point at C^*.

Figure 6-14 shows a 3D implementation of the revolved and voxelated Bezier curve between two spheres in the 3D space.

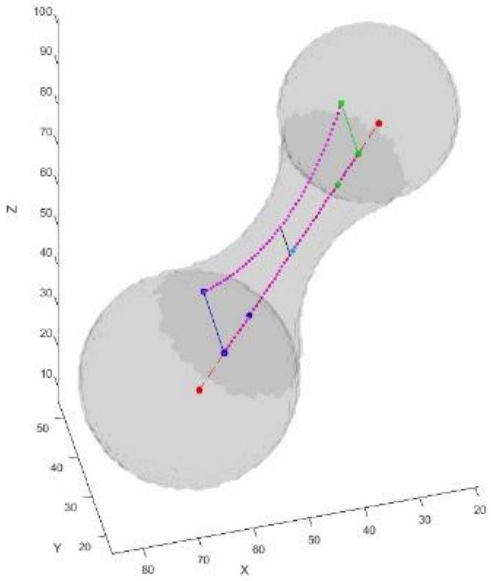

Figure 6-14: Revolved and voxelated implementation of Bezier curve between two spheres in 3D space.

Because the simulation conducted in this study does not consider dynamic changes over time, it is crucial to accurately replicate the point when the LMP particles start melting and forming the liquid bridges. Achieving this involves a specific approach to model the creation of liquid bridges as the LMP particles melt.

This approach involves first removing all the LMP particles from the RVE space. Following this, the process shifts to introducing liquid bridges, which connect only the HMP particles. As these liquid bridges are added, their mass is determined based on the density of the LMP particles. This procedure is repeated in steps, with each new liquid bridge added while maintaining the original mass ratio of the system. To prevent situations where the generated liquid bridge is physically impractical, the procedure also allows to control the minimum allowed distance in which liquid bridges can be generated.

The same RVE with HMP particles in the same spots is then given different levels of packing by changing the number of liquid bridges added. This is done to see what happens when the packing or the volume fraction of the conductive particles decreases, but the electrical conductivity still gets better, just like in the earlier experimental results. If it can be simulated, it will confirm the ideas discussed in 5.2.

In all the simulations, the electrical material properties that were used are shown in Table 6-4. In the case of the values for the effective contact conductivity, parametric study was conducted with logarithmic increments. The conductivity of the organic binder was extrapolated based on the in-situ electrical results assuming the initial curves was sensed at room temperature. The RVEs were subjected to a voltage difference of 0.01V from the front X-face to the rear X-face, with all the other faces are kept perfectly insulated.

Table 6-4: Electrical properties used in the percolation simulation.

Material	*Electrical Conductivity* $\frac{\mathbf{1}}{\boldsymbol{\Omega - m}}$
Ag	6.293e07
In	1.2e07
Organic Binder	2.0e-3
Effective Contact Conductivity	$\sigma_{Ag} * [1e0, 1e-1, 1e-2, 1e-3 \dots]$

6.4 Electrical Percolation Simulation Results and Discussion

The outcomes of the electrical percolation simulation with varied parameters are presented in Figure 6-15. This graph illustrates the relationship between resistivity and the volume fraction of conductive particles, while adhering to an 80:20 ratio of Ag

to In. When the volume fraction of conductive particles remains below 35%, the material behaves as an insulator, displaying resistivity values exceeding $1 * 10^3\ \Omega - cm$. Beyond this threshold, there is a marked and rapid decline in resistivity values, resembling the initial drop observed in the in-situ electrical tests' findings.

As anticipated, modifying the effective contact resistance between particles does not exert any influence on the simulation results below the 35% volume fraction threshold. However, changes in the effective contact resistance parameter do influence the magnitude of the resistivity drop. This effect is consistent with increasing volume fraction, thus maintaining a corresponding correlation.

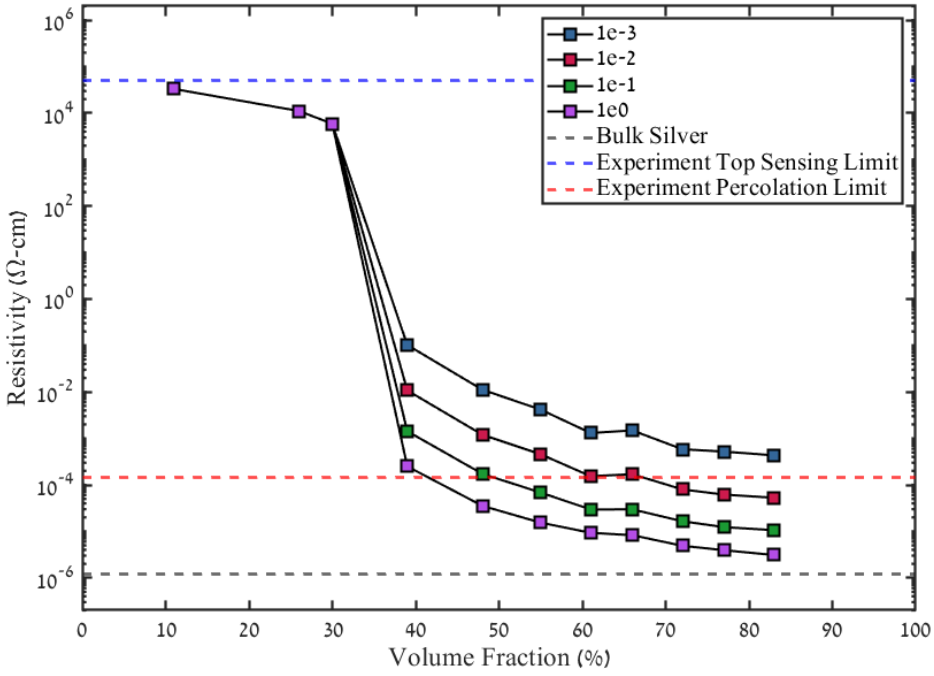

Figure 6-15: Results for the electrical percolation parametric simulation.

In Figure 6-16, the percolation state is illustrated for the initial two data points from Figure 6-15 exceeding the simulated percolation threshold of 35%. In both the left and right illustrations, the colors show the voltage decline from the heated end (red) to the zero voltage (blue).

Observing the left image, it becomes evident that within a given TLPS paste, only a single conduction path is required to surpass the percolation threshold, thus inducing the transition from an insulating to a partially conducting material. The right image demonstrates that supplementary percolation paths yield incremental electrical conductivity enhancements, much like the principles of parallel conductive Ohm's law.

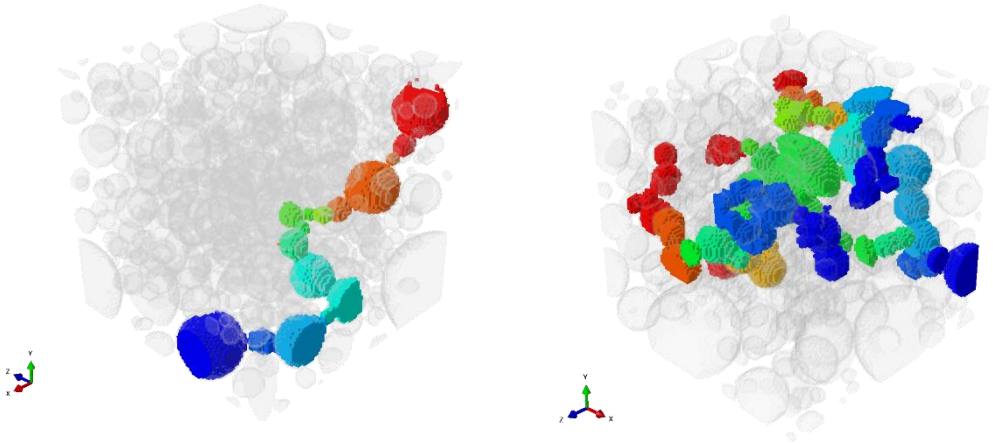

Figure 6-16: Percolation states for the first two data points from Figure 6-15.

To determine the suitable value for the effective contact resistance, the in-situ experimental percolation limit, consistently observed across all samples with organic binders A and B, was plotted. In line with Figure 5-4, simulation values aligning with the experimental percolation limit around 60-70% volume fraction were chosen as the

appropriate value for the effective contact resistance. Based on Figure 6-15, the selected contact resistance is $1 * 10^{-2} * \sigma_{Ag}$.

Once the effective contact resistance was selected, McLachlan model used to verify the results as it explains the macroscopic characteristics of the effective media based on the volume ratios of the matrix (organic binder), and the conductive particles [193] as follows:

$$\sigma_{eff} = \sigma_m \left[\Omega + \sqrt{\Omega^2 + \left(\frac{Vf_c}{1 - Vf_c}\right)\left(\frac{\sigma_p}{\sigma_m}\right)^{\frac{1}{t}}} \right]^t \quad 6.26$$

$$\Omega = \frac{1}{2(1 - Vf_c)} \left[1 - Vf_c - Vf + (Vf - Vf_c)\left(\frac{\sigma_p}{\sigma_m}\right)^{\frac{1}{t}} \right] \quad 6.27$$

Where σ_m and σ_p are the corresponding conductivities of the matrix and the conductive particles. Vf and Vf_c are the volume fraction and the threshold volume fraction accordingly. The parameter t is the critical exponent defined which is derived from the data. The fitted McLachlan model to the selected simulated data points is shown in Figure 6-17. The fitted model shows great ability to explain the data with an R^2 value of 0.9968. In addition, the model predicts the percolation threshold to be around 37% volume fraction of conductive particles, with a critical exponent of 1.721, which is in a good agreement with the literature [194]. Based on the electrical percolation simulation result, it is reasonable to confirm that the first drop in resistivity that was observed in the in-situ electrical experiments, is correlated to thermally-induced increase in the local volume fraction of the conductive particles.

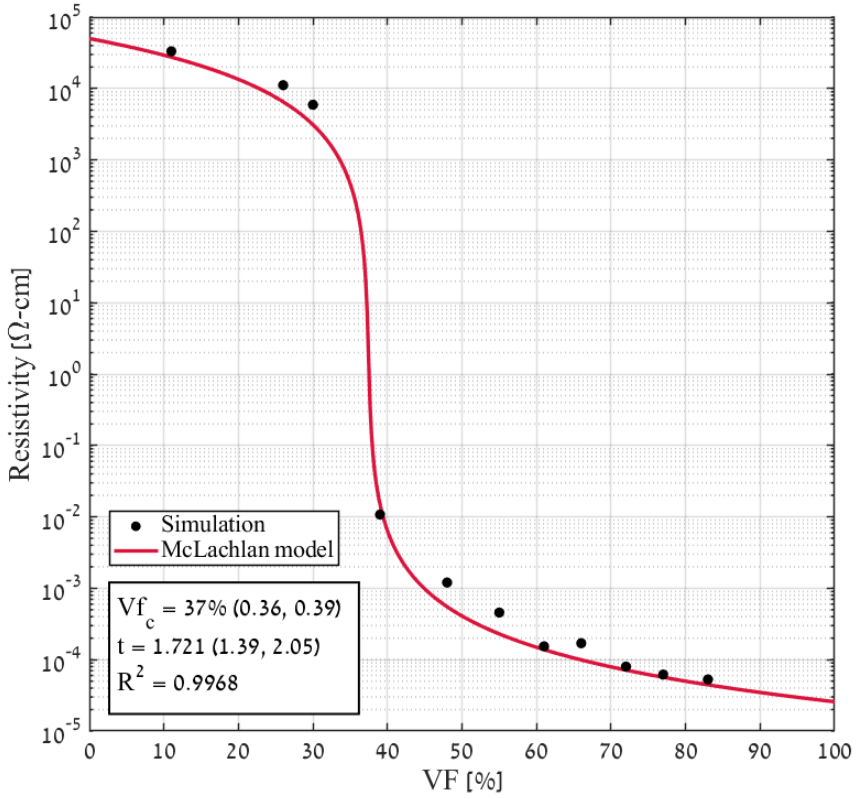

Figure 6-17: Verification of the simulation results with McLachlan model.

Subsequent to simulating the percolation network, the primary objective of the simulation was to capture the improved conductivity resulting from the melting of the LMP particles. The goal was to show that this conductivity improvement was happened despite the reduction in particle packing density during this process.

Figure 6-18 shows two chosen data points, representing volume fractions of 39% and 77%, respectively. These points were transformed into the liquid bridge configuration, resulting in a decrease in volume fraction from 39% to 33% and from

77% to 63%. This reduction in volume fraction aligns with the range previously observed in Figure 5-4.

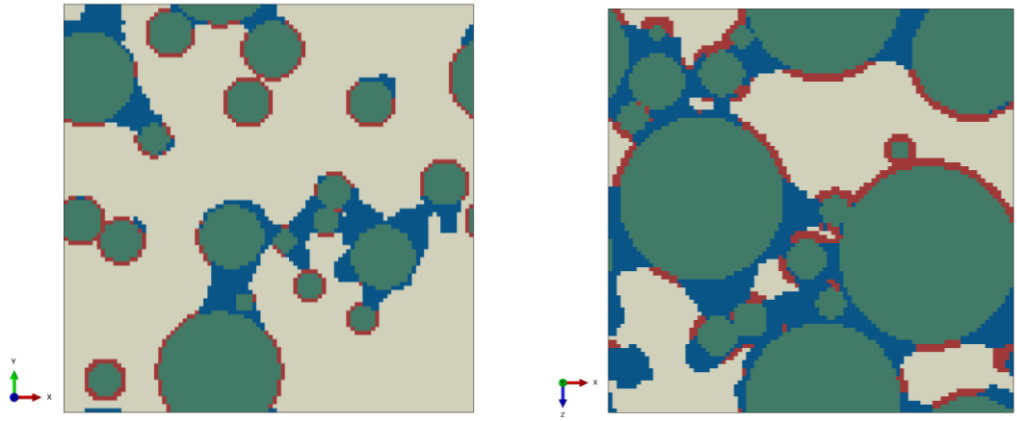

Figure 6-18: Cross sections of the two data points that were selected to show the conductive improvement during the melting of the LMP. The left figure was reduced from 39% to 33% volume fraction, and the right figure reduced from 77% to 63% volume fraction.

The outcomes presented in Figure 6-19, derived from the simulated liquid bridge models, validate the experimental findings and the discussed hypothesis. These findings indicate that despite a reduction in the overall volume fraction of conductive material, there is a notable decrease in electrical resistivity. The enhanced outcomes displayed in Figure 6-19 are summarized in Table 6-5.

Table 6-5: Simulation results for the liquid bridge electrical model.

Original VF [%]	*Reduction in VF after Liquid Bridge [%]*	*Original Percolation Electrical Resistivity* $[\Omega - cm]$	*Liquid Bridge Electrical Resistivity* $[\Omega - cm]$	*Reduction in Resistivity factor*
39	6	1.08e-02	5.72e-05	188.8
77	14	6.18e-05	8.34e-06	7.4

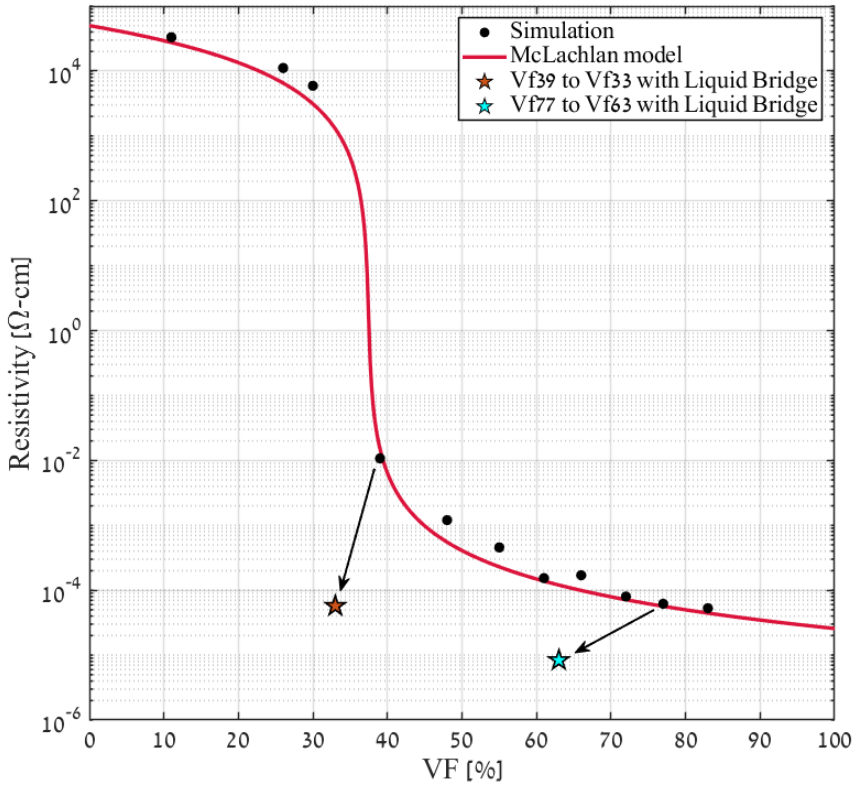

Figure 6-19: Shows the simulated improvement and shift in electrical conductivity despite the reduction in volume fraction of conductive material,

Figure 6-20 provides a visual representation of the electrical pathway within the liquid bridge simulation. On the left, the illustration reveals the electrical current pattern for the 33% volume fraction model, while the figure on the right depicts the corresponding electrical current for the 63% volume fraction model. It is evident that the unobstructed metal path facilitates the direct flow of current. To achieve further enhancement in electrical conductivity, attention should be directed towards minimizing the presence of pores and voids of the TLPS material.

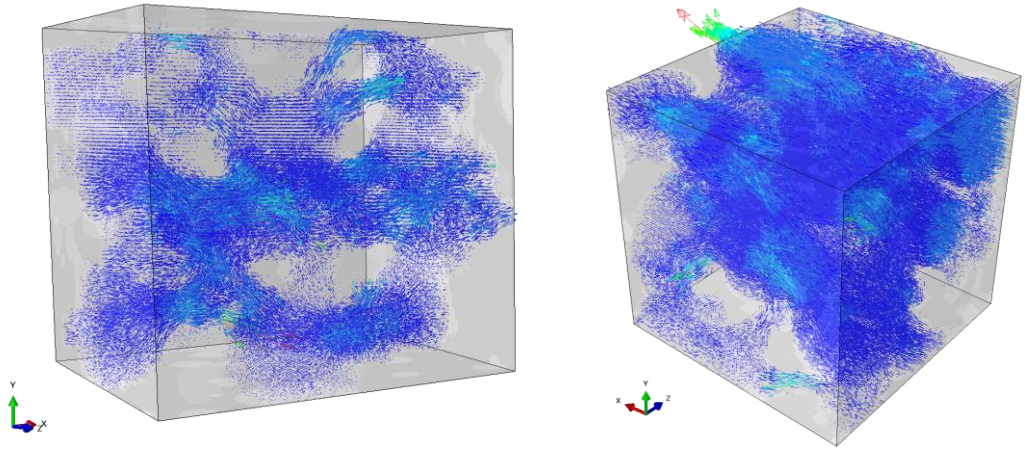

Figure 6-20: Representation of the electrical current under the voltage bias for the 33% VF model (left), and the 63% VF model (right).

7 SUMMARY AND CONTRIBUTIONS

This work and investigation were centered on the comprehensive analysis of the initial electrical and structural evolution of TLPS paste within an open atmosphere condition. The primary motivation for this study lies in the imperative to advance electronic and interconnect materials capable of withstanding harsh environments. A survey of Pb-free electronic materials suitable for extreme conditions was performed, with an emphasis on the motivation to select the TLPS as the material of interest and research. Furthermore, the work described the advantages inherent to AM, with a specific emphasis the need to develop robust AM solutions, which provides cost-efficiency, reduced complexity, and heightened manufacturing reliability. The following analysis surveyed the possible and known 3D printing methods, pinpointing the rationale for adopting paste-based DIW 3D AM as the preferred approach for this research. This trajectory also delved into the requisite transformation of TLPS into paste form to facilitate the DIW 3D AM process.

The background section introduced the working principles of TLPS systems. It examined different forms of target phases, ranging from solid solutions to specific IMCs, and elaborated strategies to achieve them. The diffusion process was divided into sequential phases characterized by their respective diffusion coefficients and states of diffusion. Following the overview of TLPS technology's operative mechanisms, specific TLPS systems, such as Cu-Sn, Ag-In, and Ag-Sn binary systems, are discussed. While the Cu-Sn system is primarily focused on specific IMCs like Cu_6Sn_5

and Cu_3Sn, the Ag-In and Ag-Sn systems are often targeting solid-solution phases renowned for their enhanced ductility performance. Subsequently, the background section extended to the integration of TLPS systems into a paste form, analyzing the roles and functionalities of organic binders and their constituent components.

The specific goals of this study are based on preliminary work and observations. Initially, diverse processing methods of 3D printing TLPS paste were tested, employing varied nozzle sizes and heating durations to determine their viability. Cross-sections of the TLPS traces, SEM micrographs, FTIR readings, and evaporations kinetics were obtained to help draw the preliminary conclusions. These preliminary tests highlighted the significance of the initial processing phase, revealing a gap in the understanding that needed further investigation. Subsequently, a comprehensive examination of the factors influencing this crucial processing stage were considered, forming the primary research objective. To bridge this knowledge gap and gain a deeper comprehension of the initial TLPS processing stage, the in-situ electrical test was proposed and developed.

The fourth chapter focused on the development of the in-situ electrical test. This development phase primarily involved two segments: the hot plate and the testing probes. The chapter outlined the iterative process of these main components. For the hot plate, this encompassed the enhancement of its ability to control temperature effectively through the implementation of heating and cooling functions, the establishment of control schemes, software integration, and manufacturing processes.

Concurrently, the development of the testing probes underwent multiple cycles of prototypes, including diverse designs and materials for the probes, compatible stencil prototypes, and the overall compatibility to the hot plate.

The fifth chapter started by examining the experimental results that were obtained from the in-situ electrical experiment. Different effects were identified and studied such as the applied heating rate, choice of LMP particles, and the choice of organic binders. In addition, to solidified and deepen the analysis, subsequent tests and measurements were employed. These measurements involved quantifying the packing density vs. temperature of the TLPS material through ESEM micrographs, elemental analysis through EDS measurements, and cross-sections analysis through a white light profiler. The observations also identified different states of solid-liquid interactions between the solid HMP and the molten LMP particles. Through these measurements and observations, the first processing stage was further divided into six sequential steps that are contributing to the electrical and structural formation of the TLPS material. The activation energies for some of these steps were extracted by using Arrhenius relationship, and LMM techniques.

To further validate and confirm the findings presented in the fifth chapter, the sixth chapter introduced a modeling and simulation framework. This framework encompasses the creation of a model with periodic geometry. Various algorithms were developed and applied to generate this periodic geometry. Once the periodic geometry was established, the models underwent FEM analysis using periodic boundary

conditions. This facilitated a homogenization technique aimed at determining the effective material properties of the TLPS material under different states. Furthermore, the simulation involved modeling liquid bridges to reinforce the observations indicating that, while the LMP particles melt, the packing density diminishes and electrical conductivity improves.

7.1 Academic Contributions

This study delivers a range of academic contributions across various domains, encompassing mechanical engineering, material science, and chemistry, with the potential to facilitate future interdisciplinary research and collaboration. The following points captures the specific academic contributions of this work:

1. **Recognition of the primary TLPS processing phase as a pivotal bottleneck necessitating dedicated attention.** This departure from some earlier studies, which predominantly targeted later and post-processing challenges, underscores the significance of addressing this initial stage.
2. **Elaborate mapping of considerations inherent in the initial stage of the TLPS processing.** These comprehensive mappings not only highlight research gaps but also unravel coupled effects, demanding further research and decoupling.
3. **For the first time in the literature, implementation of in-situ electrical measurements during TLPS paste heating and processing.** In contrast to studies relying on isolated post-processing data points, these in-situ tests enable

deeper understanding and additional correlation between different processing parameters and the overall performance of TLPS.

4. Utilization of in-situ electrical measurements to observe, illustrate, and isolate the influences of various processing factors. **This study decouples effects tied to heating rates, LMP particle selection, and the selection of organic binders**. Notably, lower heating rates prompt electrical signals and electrical percolation thresholds at lower temperatures due to organic binder evaporation that is less subjected to inertial heating and diffusion effects. LMP selection showed the ability to shift the second major drop in the electrical resistivity, usually closer to the melting point of the LMP particles. The selection of the organic binders showed its importance by completely change the form or shift the electrical evolution curve, making it a prime factor to consider when designing TLPS paste for robust AM applications.
5. Identification of distinct solid-liquid states. Previously, the solid-liquid interactions that take place during the processing of the TLPS material were generally referred as capillary interactions. While this is generally true, **this study identified and analyzed four discrete capillary states during TLPS paste processing with micro-scale-based powders.** This revelation helps to explain the decrease in packing density upon LMP particle melting and underscores the role of particle sizes: particles with diameters above 25 μm form isolated liquid bridges, particles with diameters between 5 and 25 μm

create connected and coalesced liquid bridges, and particles with diameters below 5 μm become fully submerged in the liquid LMP metal.

6. Based on white light profiler cross-section analysis, **the degree of cross-sectional change during the heating process was quantified.** It was shown that during the processing of the TLPS paste, there was a minimal change in cross-section, which implies the rapid structural formation and backbone of the material, allows for efficient AM applications.
7. **Sequential identification of electrical and structural TLPS paste development during the initial processing phase, quantification, and illustration of these stages.** Activation energies are extracted at different stages for various combinations of paste compositions, with processing parameters calculated using the Arrhenius relationship and LMM fitting techniques. It was shown that based on the measured activation energies, the two major drops in the electrical curve evaluation are associates with phase transitions of the organic binder and the LMP particles. For the third stage of the electrical evolution, activation energies were measured between 88.48, and 328.51 $kJ \cdot mol^{-1}$ for different test combinations. The increase activation energies were also found to be correlated with elevated processing temperature.
8. **Formulation of a simplified algorithm to generate RVEs** featuring particle volume fractions exceeding 80%, replicating empirically observed log-normal

size distributions. This approach requires minimal input parameters, facilitating reproducible modeling of observed microstructures.

9. **Introduction of Bezier curves for modeling liquid bridges arising from LMP particle melting.** This method simplifies the utilization of parametric curves and efficient implementation practices to model liquid bridges for simulation purposes.
10. Verification of in-situ electrical test outcomes through FEM simulations. These simulations verify numerous hypotheses, yielding profound insights. The simulations visualize electrical percolation formation and offer estimates for the effective contact resistance between un-melted particles and residual inorganic material, ultimately influencing the electrical performance of TLPS materials. In addition, McLachlan model for effective electrical conductivity was fitted the simulated data to gain additional insights towards the formation of the electrical evolution of the TLPS material.

7.2 Future Work

Based on the discoveries and analysis within this study, distinct areas of interest and potential future research directions emerge concerning the development of TLPS paste. In the future research, the focus should be directed towards these key domains:

1. **Development of TLPS Paste with Smaller Particles:** Future research could focus on formulating TLPS pastes incorporating particles below 5 μm. The aim is to achieve a uniform capillary action or completely submerge HMP particles

within the LMP liquid. This approach aims to enhance packing densities and reduce processing-related pores. Notably, the challenge lies in managing the significant increase in paste viscosity resulting from smaller particles when current and commercial organic binders are employed. This increase in viscosity could render the paste unsuitable for AM or stencil printing applications. Addressing this challenge requires the development of tailored organic binder systems that can effectively balance the viscosity issues associated with smaller particles.

2. **Verification of Particle Size Effects on Electrical Curve Evolution:** A productive avenue for exploration involves validating the impact of different particle sizes on the evolution of electrical curves through in-situ electrical tests, complemented by corresponding FEM simulations. The utilization of varied particle sizes or distributions holds potential to influence material evolution from multiple angles, including the formation of percolation networks, the dynamics of organic evaporation, and crucially, the dynamics governing different capillary states and forces.
3. **Mechanical Testing of Optimized Electrical Paste Formulation:** Subsequent to achieving an optimal formulation for the electrical paste, subsequent steps can include mechanical assessments such as shear testing and drop tests on the material. Addition, compatibility of future paste formulations with ceramic

substrates, crucial for applications involving high temperatures and harsh environments.

Appendix I – Replication of Stochastic FEA Study

Volume Fraction of Aggregates		5	10	15	20	27.5
Elastic Modulus [GPa]	Current Model	3.350	3.775	4.299	4.855	5.898
	Stochastic Model	3.340	3.728	4.173	4.688	5.635
	Percent Difference	0.309	1.240	2.985	3.496	4.569
Poisson's ratio	Current Model	0.394	0.387	0.380	0.373	0.360
	Stochastic Model	0.387	0.373	0.359	0.342	0.306
	Percent Difference	1.799	3.887	5.705	8.665	16.363
CTE [ppm/°C]	Current Model	52.296	49.621	46.607	44.041	40.170
	Stochastic Model	52.120	49.340	46.580	43.960	40.190
	Percent Difference	0.338	0.567	0.056	0.185	0.050

Appendix II – Dimensions and Sizes of Particles in The Simulation

	Aggregate 1 Radius	**Aggregate 2 Radius**	**Aggregate 3 Radius**	**Transition 1 Radius**	**Transition 2 Radius**	**Transition 3 Radius**	**Void Radius**
Figures (3-6)	18	20	28	21.96	24.4	34.16	15
Figures (7-10)	20	22	24	26	28.6	31.2	15

Bibliography

[1] G. Luderer, S. Madeddu, L. Merfort, F. Ueckerdt, M. Pehl, R. Pietzcker, M. Rottoli, F. Schreyer, N. Bauer, L. Baumstark, C. Bertram, A. Dirnaichner, F. Humpenöder, A. Levesque, A. Popp, R. Rodrigues, J. Strefler, and E. Kriegler, Impact of declining renewable energy costs on electrification in low-emission scenarios. Nat. Energy **7**, 32 (2022).

[2] Samuel K. Moore, Another Step Toward the End of Moore's Law. IEEE Spectrum, 9 (2019).

[3] J. R. Powell, The quantum limit to Moore's law. Proc. IEEE **96**, 1247 (2008).

[4] 3-micron Technology. https://www.tsmc.com/english/dedicatedFoundry/technology/logic/l_3micron.

[5] B. Bailey, The Impact of Moore ' s Law. https://semiengineering.com/the-impact-of-moores-law-ending/.

[6] L. Xiu, Time Moore: Exploiting Moore's Law from the Perspective of Time. IEEE Solid-State Circuits Mag. **11**, 39 (2019).

[7] J. Shalf, The future of computing beyond Moore ' s Law. Philos. Trans. R. Soc. **378**, 1 (2020).

[8] J. B. Aimone, Neural algorithms and computing beyond Moore's law. Commun. ACM **62**, 110 (2019).

[9] R. Chen, Y. C. Li, J. M. Cai, K. Cao, and H. B. R. Lee, Atomic level deposition to extend Moore's law and beyond. Int. J. Extrem. Manuf. **2**,

(2020).

[10] D. Jha, V. Gupta, W. keng Liao, A. Choudhary, and A. Agrawal, Moving closer to experimental level materials property prediction using AI. Sci. Rep. **12**, 1 (2022).

[11] W. Sha, Y. Guo, Q. Yuan, S. Tang, X. Zhang, S. Lu, X. Guo, Y.-C. Cao, and S. Cheng, Artificial Intelligence to Power the Future of Materials Science and Engineering. Adv. Intell. Syst. **2**, 1900143 (2020).

[12] T. Ma, Future of power electronics from TCAD perspective. Int. Conf. Simul. Semicond. Process. Devices, SISPAD **2020**-**Septe**, 97 (2020).

[13] C. Langpoklakpam, A. C. Liu, K. H. Chu, L. H. Hsu, W. C. Lee, S. C. Chen, C. W. Sun, M. H. Shih, K. Y. Lee, and H. C. Kuo, Review of Silicon Carbide Processing for Power MOSFET. Crystals **12**, 1 (2022).

[14] S. Siva Subramanian, R. Saravanakumar, B. P. Ganthia, S. Kaliappan, S. M. Beyan, M. Mallick, M. Mohanty, and G. Pavithra, A Comprehensive Examination of Bandgap Semiconductor Switches. Adv. Mater. Sci. Eng. **2021**, (2021).

[15] O. Deblecker, Z. De Grève, and C. Versèle, Comparative Study of Optimally Designed DC-DC Converters with SiC and Si Power Devices. Adv. Silicon Carbide Devices Process. (2015).

[16] K. O. Armstrong, S. Das, and J. Cresko, Wide bandgap semiconductor opportunities in power electronics. *Wide Bandgap Semiconductor*

Opportunities in Power Electronics (2016).

[17] A. Castellazzi, Opportunities and challenges of integrated WBG power electronics development. 2021 3rd Int. Symp. 3D Power Electron. Integr. Manuf. 3D-PEIM 2021 1 (2021).

[18] I. C. Kizilyalli, Y. Xu, E. Carlson, J. Manser, and D. W. Cunningham, Current and future directions in power electronic devices and circuits based on wide band-gap semiconductors. 2017 IEEE 5th Work. Wide Bandgap Power Devices Appl. WiPDA 2017 **2017-Decem**, 417 (2017).

[19] F. Blaabjerg and K. Ma, Future on power electronics for wind turbine systems. IEEE J. Emerg. Sel. Top. Power Electron. **1**, 139 (2013).

[20] D. Cervero, M. Fotopoulou, J. Muñoz-Cruzado, D. Rakopoulos, F. Stergiopoulos, N. Nikolopoulos, S. Voutetakis, and J. F. Sanz, Solid State Transformers: A Critical Review of Projects with Relevant Prototypes and Demonstrators. Electron. **12**, 1 (2023).

[21] T. Van Do, J. P. F. Trovao, K. Li, and L. Boulon, Wide-Bandgap Power Semiconductors for Electric Vehicle Systems: Challenges and Trends. IEEE Veh. Technol. Mag. **16**, 89 (2021).

[22] A. Barzkar and M. Ghassemi, Electric power systems in more and all electric aircraft: A review. IEEE Access **8**, 169314 (2020).

[23] L. Dorn-Gomba, J. Ramoul, J. Reimers, and A. Emadi, Power Electronic Converters in Electric Aircraft: Current Status, Challenges, and Emerging

Technologies. IEEE Trans. Transp. Electrif. **6**, 1648 (2020).

[24] S. Ohn, J. Yu, R. Burgos, D. Boroyevich, H. Suryanarayana, and C. Belcastro, Single pulse common-mode voltage PWM scheme to achieve high power-density for full-SiC three-level uninterruptible power supply. Conf. Proc. - IEEE Appl. Power Electron. Conf. Expo. - APEC **2019-March**, 2377 (2019).

[25] Y. Chen, S. Grijalva, L. Graber, and Y. Seyedi, Techno-Economical Assessment of AC and DC Power Distribution Architectures for Data Centers. 2022 North Am. Power Symp. NAPS 2022 **1**, 1 (2022).

[26] B. Jux, S. Foitzik, and M. Doppelbauer, A Standard Mission Profile for Hybrid-Electric Regional Aircraft based on Web Flight Data. Proc. 2018 IEEE Int. Conf. Power Electron. Drives Energy Syst. PEDES 2018 1 (2018).

[27] M. Z. Erel, K. C. Bayindir, M. T. Aydemir, S. K. Chaudhary, and J. M. Guerrero, A Comprehensive Review on Wireless Capacitive Power Transfer Technology: Fundamentals and Applications. IEEE Access **10**, 3116 (2022).

[28] J. A. Ferreira and P. Wilson, The Impact of ITRW: How Can WBG Power Semiconductors Break Through?. IEEE Open J. Power Electron. **2**, 327 (2021).

[29] L. Wang, W. Wang, R. J. E. Hueting, G. Rietveld, and J. A. Ferreira, Review of Topside Interconnections for Wide Bandgap Power Semiconductor Packaging. IEEE Trans. Power Electron. **38**, 472 (2023).

[30] C. Liu, Advanced Pb-free Interconnect Materials and Manufacture Processes to Enable High-temperature Electronics Packaging. (2022).

[31] H. Wang, M. Liserre, and F. Blaabjerg, Toward reliable power electronics: Challenges, design tools, and opportunities. IEEE Ind. Electron. Mag. **7**, 17 (2013).

[32] A. Hassan, Y. Savaria, and M. Sawan, Electronics and packaging intended for emerging harsh environment applications: A review. IEEE Trans. Very Large Scale Integr. Syst. **26**, 2085 (2018).

[33] F. Roccaforte, P. Fiorenza, G. Greco, R. Lo Nigro, F. Giannazzo, F. Iucolano, and M. Saggio, Emerging trends in wide band gap semiconductors (SiC and GaN) technology for power devices. Microelectron. Eng. **187**–**188**, 66 (2018).

[34] H. W. Vannessa Goodship, Ab L.N. Stevels, Ruediger Kuehr, Rebecca Stewart, Pascal Leroy, Heinz W. Böni, Jaco Huisman, Martin Goosey, Winifred L. Ijomah , M. Danis, Antoinette van Schaik, Markus A. Reuter, Kylash Makenji, Mark Savage, Maria Paola Luda, Arnold Tu, Waste Electrical and Electronic Equipment (WEEE) Handbook. *Waste Electrical and Electronic Equipment (WEEE) Handbook*, 2nd ed. (Woodhead Publishing, 2019).

[35] Z. Yao, S. Jiang, L. Yin, D. Ling, Z. Zhang, and L. Zhang, Effects of Joint Height on the Interfacial Microstructure and Mechanical Properties of Cu-Cored SAC305 Solder Joints. J. Electron. Mater. **49**, 5391 (2020).

[36] K. N. Tu, Reliability challenges in 3D IC packaging technology. Microelectron. Reliab. **51**, 517 (2011).

[37] O. R. Adetunji, R. A. Ashimolowo, P. O. Aiyedun, O. M. Adesusi, H. O. Adeyemi, and O. R. Oloyede, Tensile, hardness and microstructural properties of Sn-Pb solder alloys. Mater. Today Proc. **44**, 321 (2021).

[38] M. Aamir, R. Muhammad, and M. Hanif, Relationships between Microstructure and Mechanical Properties in High Sn Content Pb-based and Pb-Free Solder Alloy after Thermal Aging. Int. J. Adv. Mater. Manuf. **01**, 33 (2016).

[39] H. Zhang, J. Minter, and N. C. Lee, A Brief Review on High-Temperature, Pb-Free Die-Attach Materials. J. Electron. Mater. **48**, 201 (2019).

[40] S. juan Zhong, L. Zhang, M. lan Li, W. min Long, and F. jiang Wang, Development of lead-free interconnection materials in electronic industry during the past decades: Structure and properties. Mater. Des. **215**, 110439 (2022).

[41] Y. Chen, C. Liu, Z. Zhou, and C. Liu, Transient liquid phase bonding with Ga-based alloys for electronics interconnections. J. Manuf. Process. **84**, 1310 (2022).

[42] R. Z. Wang, H. H. Gu, S. P. Zhu, K. S. Li, J. Wang, X. W. Wang, M. Hideo, X. C. Zhang, and S. T. Tu, A data-driven roadmap for creep-fatigue reliability assessment and its implementation in low-pressure turbine disk at elevated temperatures. Reliab. Eng. Syst. Saf. **225**, 108523 (2022).

[43] D. Bani Hani, R. Al Athamneh, M. Abueed, and S. Hamasha, Neural-fuzzy

machine learning approach for the fatigue-creep reliability modeling of SAC305 solder joints. Sci. Rep. **13**, 1 (2023).

[44] O. Mokhtari, A review: Formation of voids in solder joint during the transient liquid phase bonding process - Causes and solutions. Microelectron. Reliab. **98**, 95 (2019).

[45] M. Kozak, P. Vesely, and K. Dusek, Analysis of solder mask roughness and stencil shape influence on void formation in solder joints. Weld. World **67**, 1347 (2023).

[46] S. M. Yeo, H. K. Yow, K. H. Yeoh, and S. H. Bin Ishak, Vacuum Reflow Process Optimization for Solder Void Size Reduction in Semiconductor Packaging Assembly. IEEE Trans. Components, Packag. Manuf. Technol. **12**, 1410 (2022).

[47] F. Jia, L. Niu, Y. Xi, Y. Qiu, H. Ma, and C. Yang, Experimental and multiphysics simulation study of atoms migration and morphology evolution in solder joints under high current density. Int. J. Heat Mass Transf. **202**, 123719 (2023).

[48] C. Imediegwu, S. Graham, D. G. Pahinkar, S. Narumanchi, P. Paret, and J. Major, Interdiffusion and formation of intermetallic compounds in high-temperature power electronics substrate joints fabricated by transient liquid phase bonding. Microelectron. Reliab. **137**, 114788 (2022).

[49] A. Lis, High power electronics packaging by transient liquid phase bonding.

High Power Electronics Packaging by Transient Liquid Phase Bonding, 2015.

[50] A. Khorram and M. Ghoreishi, Numerical and experimental study of flowing and spreading of silver-based filler metal droplet on different substrates during laser brazing process. Int. J. Adv. Manuf. Technol. **85**, 503 (2016).

[51] W. Zhang, Y. Cao, J. Huang, W. Zhao, X. Liu, M. Li, and H. Ji, Ultrasonic-accelerated metallurgical reaction of Sn/Ni composite solder: Principle, kinetics, microstructure, and joint properties. Ultrason. Sonochem. **66**, 105090 (2020).

[52] H. Pan, J. Huang, H. Ji, and M. Li, Enhancing the solid/liquid interfacial metallurgical reaction of Sn+Cu composite solder by ultrasonic-assisted chip attachment. J. Alloys Compd. **784**, 603 (2019).

[53] C. Chen, L. Zhang, X. Wang, X. Lu, L. li Gao, M. Zhao, and S. juan Zhong, Review of ultrasonic-assisted soldering in Sn-based solder alloys. J. Mater. Sci. Mater. Electron. **34**, 1 (2023).

[54] Y. T. Hwang, W. H. Chung, Y. R. Jang, and H. S. Kim, Intensive Plasmonic Flash Light Sintering of Copper Nanoinks Using a Band-Pass Light Filter for Highly Electrically Conductive Electrodes in Printed Electronics. ACS Appl. Mater. Interfaces **8**, 8591 (2016).

[55] B. Liu, Y. Tian, J. Feng, and C. Wang, Enhanced shear strength of Cu–Sn intermetallic interconnects with interlocking dendrites under fluxless electric current-assisted bonding process. J. Mater. Sci. **52**, 1943 (2017).

[56] F. Cosiansi, ISPET: Interface Sintering Process Enhanced Technology. ISPET: Interface Sintering Process Enhanced Technology, Politecnico di Torino Doctoral, 2016.

[57] N. Ismail, A. Atiqah, A. Jalar, M. A. Bakar, R. A. A. Rahim, A. G. Ismail, A. A. Hamzah, and L. K. Keng, A systematic literature review: The effects of surface roughness on the wettability and formation of intermetallic compound layers in lead-free solder joints. J. Manuf. Process. **83**, 68 (2022).

[58] H. Zhang, S. P. Lim, S. Lytwynec, T. Richmond, and T. Harter, A Drop-In High-Temperature Lead-Free Solder Paste that Outperforms High-Pb Pastes in Power Discrete Applications. 2022 Int. Conf. Electron. Packag. ICEP 2022 69 (2022).

[59] F. F. Le, R. van der Meulen, Y. K. Leong, M. Balakrishnan, and Z. Guan, Evaluation of Emerging High Melting Point Lead-free Solder and Hybrid Sinter Paste as Attaching Material for Clip Bond Package. Int. Symp. Microelectron. **2020**, 000235 (2020).

[60] S. Mukherjee, M. Nuhi, A. Dasgupta, and M. Modarres, Creep constitutive models suitable for solder alloys in electronic assemblies. J. Electron. Packag. Trans. ASME **138**, 1 (2016).

[61] N. Jiang, L. Zhang, Z. Q. Liu, L. Sun, W. M. Long, P. He, M. Y. Xiong, and M. Zhao, Reliability issues of lead-free solder joints in electronic devices. Sci. Technol. Adv. Mater. **20**, 876 (2019).

[62] J. McConnell, J. Bultitude, L. Jones, and J. Qazi, Transient liquid phase sintering materials (TLPS) vs. conventional solders for high temperature MLCC interconnects. Int. Symp. Microelectron. **2016**, 000624 (2016).

[63] J. Xu, M. Wu, J. Pu, and S. Xue, Novel Au-Based Solder Alloys: A Potential Answer for Electrical Packaging Problem. Adv. Mater. Sci. Eng. **2020**, (2020).

[64] G. Q. Lu, C. Yan, Y. Mei, and X. Li, Dependence of electrochemical migration of sintered nanosilver on chloride. Mater. Chem. Phys. **151**, 18 (2015).

[65] A. Mathew, R. Dudek, A. Otto, C. Scherf, S. Rzepka, N. Subhaiah, K. A. Rane, and J. Wilde, Investigation of reliability issues in sintered silver interconnected power devices and its lifetime prediction by FEM and experiment. ETG-Fachbericht **2022-March**, 436 (2022).

[66] S. K. Bhogaraju and E. Gordon, Material Innovation, Process Development, Reliability & Challenges with Copper Sintered Interconnects for High Power & Optoelectronics Packaging. in *PCIM Europe 2023; International Exhibition and Conference for Power Electronics, Intelligent Motion, Renewable Energy and Energy Management* (2023), pp. 1394–1399.

[67] Q. An, R. An, C. Wang, and H. Wang, Ductile-to-brittle transition in fracture behaviors of common solder alloys over a temperature range down to −150 °C. Mater. Today Commun. **29**, (2021).

[68] M. A. Fazal, N. K. Liyana, S. Rubaiee, and A. Anas, A critical review on performance, microstructure and corrosion resistance of Pb-free solders. Meas.

J. Int. Meas. Confed. **134**, 897 (2019).

[69] X. Zhao, W. Zhang, C. Wang, R. An, W. Liu, and C. Hang, Effect of Aging Time on Ductile–Brittle Transition Behaviors of Sn-3.5Ag Solder. J. Electron. Mater. **52**, 471 (2023).

[70] H. Zhang, H. Xu, X. Liu, and J. Xu, Fabrication of Cu@Sn TLPS joint for high temperature power electronics application. RSC Adv. **12**, 29063 (2022).

[71] J. Bultitude, J. McConnell, L. Jones, G. Miller, J. Magee, A. Templeton, A. Gurav, and R. Phillips, A Comparison between Solders & Transient Liquid Phase Sintered Interconnects in High Temperature Multilayer Ceramic Capacitors. J. Microelectron. Electron. Packag. **14**, 150 (2017).

[72] Properties of solder alloys. https://invacu.com/solder-alloys.

[73] A. Syed-Khaja, Diffusion Soldering for High-temperature Packaging of Power Electronics. Diffusion Soldering for High-Temperature Packaging of Power Electronics, FAU University, 2018.

[74] M. Myśliwiec and R. Kisiel, Die attachment Process Overview for High Power Semiconductors. 2023 46th Int. Spring Semin. Electron. Technol. 1 (n.d.).

[75] K. S. Siow, Die-attach materials for high temperature applications in microelectronics packaging: Materials, processes, equipment, and reliability. *Die-Attach Materials for High Temperature Applications in Microelectronics Packaging: Materials, Processes, Equipment, and Reliability* (2019).

[76] O. Dibua, A. Liao, F. Tasnim, J. Grose, D. Behera, C. Foong, and M. Cullinan,

A Study of the electrical resistivity of sintered copper nanoparticles. in *Solid Freeform Fabrication 2022: Proceedings of the 33rd Annual International Solid Freeform Fabrication Symposium – An Additive Manufacturing Conference* (2022), pp. 383–396.

[77] F. Yu, H. Liu, C. Hang, H. Chen, and M. Li, Rapid Formation of Full Intermetallic Bondlines for Die Attachment in High-Temperature Power Devices Based on Micro-sized Sn-Coated Ag Particles. Jom **71**, 3049 (2019).

[78] P. O. Quintero, Development of a shifting melting point Ag In paste via transient liquid phase sintering for high temperature environmnets. Development of a Shifting Melting Point Ag In Paste via Transient Liquid Phase Sintering for High Temperature Environmnets, University of Maryland at College Park, 2008.

[79] L. Becker, Chemical elements by market price. http://www.leonland.de/elements_by_price/en/list%0Ahttp://www.leonland.de/elements_by_price/list?ccy=USD&unit=kg.

[80] A. H. Espera, J. R. C. Dizon, Q. Chen, and R. C. Advincula, 3D-printing and advanced manufacturing for electronics. Prog. Addit. Manuf. **4**, 245 (2019).

[81] C. H. Rao, K. Avinash, B. K. S. V. L. Varaprasad, and S. Goel, A Review on Printed Electronics with Digital 3D Printing: Fabrication Techniques, Materials, Challenges and Future Opportunities. J. Electron. Mater. **51**, 2747 (2022).

[82] B. H. Lu, H. B. Lan, and H. Z. Liu, Additive manufacturing frontier: 3D printing electronics. Opto-Electronic Adv. **1**, 1 (2018).

[83] S. Lohrasbi, R. Hammer, W. Essl, G. Reiss, S. Defregger, and W. Sanz, A comprehensive review on the core thermal management improvement concepts in power electronics. IEEE Access **8**, 166880 (2020).

[84] D. José Horst and R. De Almeida Vieira, Additive Manufacturing at Industry 4.0: a Review. Artic. Int. J. Eng. Tech. Res. **0869**, 3 (2018).

[85] O. Abdulhameed, A. Al-Ahmari, W. Ameen, and S. H. Mian, Additive manufacturing: Challenges, trends, and applications. Adv. Mech. Eng. **11**, 1 (2019).

[86] Q. Ge, Z. Li, Z. Wang, K. Kowsari, W. Zhang, X. He, J. Zhou, and N. X. Fang, Projection micro stereolithography based 3D printing and its applications. Int. J. Extrem. Manuf. **2**, (2020).

[87] J. Huang, Q. Qin, and J. Wang, A review of stereolithography: Processes and systems. Processes **8**, (2020).

[88] P. J. Bartolo and J. Gaspar, Metal filled resin for stereolithography metal part. CIRP Ann. - Manuf. Technol. **57**, 235 (2008).

[89] M. Baechle-Clayton, E. Loos, M. Taheri, and H. Taheri, Failures and Flaws in Fused Deposition Modeling (FDM) Additively Manufactured Polymers and Composites. J. Compos. Sci. **6**, (2022).

[90] D. Syrlybayev, B. Zharylkassyn, A. Seisekulova, M. Akhmetov, A. Perveen,

and D. Talamona, Optimisation of Strength Properties of FDM Printed Parts — A. Polymers (Basel). **13**, 1 (2021).

[91] H. Ramazani and A. Kami, Metal FDM, a new extrusion-based additive manufacturing technology for manufacturing of metallic parts: a review. Prog. Addit. Manuf. **7**, 609 (2022).

[92] A. Jabbari and K. Abrinia, A metal additive manufacturing method: semi-solid metal extrusion and deposition. Int. J. Adv. Manuf. Technol. **94**, 3819 (2018).

[93] X. Zhang, C. J. Yocom, B. Mao, and Y. Liao, Microstructure evolution during selective laser melting of metallic materials: A review. J. Laser Appl. **31**, (2019).

[94] E. L. Papazoglou, N. E. Karkalos, P. Karmiris-Obratański, and A. P. Markopoulos, On the Modeling and Simulation of SLM and SLS for Metal and Polymer Powders: A Review. *On the Modeling and Simulation of SLM and SLS for Metal and Polymer Powders: A Review*, Vol. 29 (Springer Netherlands, 2022).

[95] Y. Yang, O. Ragnvaldsen, Y. Bai, M. Yi, and B. X. Xu, 3D non-isothermal phase-field simulation of microstructure evolution during selective laser sintering. Npj Comput. Mater. **5**, (2019).

[96] Y. Yang, D. Gu, D. Dai, and C. Ma, Laser energy absorption behavior of powder particles using ray tracing method during selective laser melting additive manufacturing of aluminum alloy. Mater. Des. **143**, 12 (2018).

[97] P. K. Gokuldoss, S. Kolla, and J. Eckert, Additive manufacturing processes: Selective laser melting, electron beam melting and binder jetting-selection guidelines. Materials (Basel). **10**, (2017).

[98] L. C. Zhang, Y. Liu, S. Li, and Y. Hao, Additive Manufacturing of Titanium Alloys by Electron Beam Melting: A Review. Adv. Eng. Mater. **20**, 1 (2018).

[99] M. Li, W. Du, A. Elwany, Z. Pei, and C. Ma, Metal binder jetting additive manufacturing: A literature review. J. Manuf. Sci. Eng. Trans. ASME **142**, 1 (2020).

[100] M. Ziaee and N. B. Crane, Binder jetting: A review of process, materials, and methods. Addit. Manuf. **28**, 781 (2019).

[101] A. C. H. Tsang, J. Zhang, K. N. Hui, K. S. Hui, and H. Huang, Recent Development and Applications of Advanced Materials via Direct Ink Writing. Adv. Mater. Technol. **7**, 1 (2022).

[102] S. Lamnini, H. Elsayed, Y. Lakhdar, F. Baino, F. Smeacetto, and E. Bernardo, Robocasting of advanced ceramics: ink optimization and protocol to predict the printing parameters - A review. Heliyon **8**, e10651 (2022).

[103] V. G. Rocha, E. Saiz, I. S. Tirichenko, and E. García-Tuñón, Direct ink writing advances in multi-material structures for a sustainable future. J. Mater. Chem. A **8**, 15646 (2020).

[104] C. Xu, B. Quinn, L. L. Lebel, D. Therriault, and G. L'espérance, Multi-Material Direct Ink Writing (DIW) for Complex 3D Metallic Structures with

Removable Supports. ACS Appl. Mater. Interfaces **11**, 8499 (2019).

[105] M. V. Johnson, K. Garanger, J. O. Hardin, J. D. Berrigan, E. Feron, and S. R. Kalidindi, A generalizable artificial intelligence tool for identification and correction of self-supporting structures in additive manufacturing processes. Addit. Manuf. **46**, 102191 (2021).

[106] B. T. Gibson, P. Mhatre, M. C. Borish, J. L. West, E. D. Betters, S. S. Smith, B. S. Richardson, L. J. Love, T. W. Sundermann, J. T. Potter, E. J. Vetland, W. C. Henry, and C. P. Allison, Accelerating large-format metal additive manufacturing: How controls R&D is driving speed, scale, and efficiency. ASME Int. Mech. Eng. Congr. Expo. Proc. **2**A-**2020**, 1 (2020).

[107] C. G. Moura, O. Carvalho, V. H. Magalhães, R. S. F. Pereira, M. F. Cerqueira, L. M. V. Gonçalves, R. M. Nascimento, and F. S. Silva, Laser printing of micro-electronic communication systems for smart implants applications. Opt. Laser Technol. **128**, 106211 (2020).

[108] B. Nagarajan, Z. Hu, X. Song, W. Zhai, and J. Wei, Development of Micro Selective Laser Melting: The State of the Art and Future Perspectives. Engineering **5**, 702 (2019).

[109] N. K. Roy, D. Behera, O. G. Dibua, C. S. Foong, and M. A. Cullinan, A novel microscale selective laser sintering (μ-SLS) process for the fabrication of microelectronic parts. Microsystems Nanoeng. **5**, (2019).

[110] G. Yang, G. Xu, Q. Li, Y. Zeng, Y. Zhang, M. Hao, and C. Cui, Understanding

the sintering and heat dissipation behaviours of Cu nanoparticles during low-temperature selective laser sintering process on flexible substrates. J. Phys. D. Appl. Phys. **54**, (2021).

[111] L. Mo, Z. Guo, L. Yang, Q. Zhang, Y. Fang, Z. Xin, Z. Chen, K. Hu, L. Han, and L. Li, Silver nanoparticles based ink with moderate sintering in flexible and printed electronics. Int. J. Mol. Sci. **20**, (2019).

[112] J. McKenzie, S. Parupelli, D. Martin, and S. Desai, Additive manufacturing of multiphase materials for electronics. 67th Annu. Conf. Expo Inst. Ind. Eng. 2017 1133 (2017).

[113] S. M. Mirramazani, S. Javadinejad, S. Eslamian, F. Jafary, V. P. Singh, and K. Ostad-Ali-Askari, A Feasibility Study of Urban Green Space Design in the Form of Smart Arid Landscaping with Rainwater Harvesting. Am. J. Eng. Appl. Sci. Orig. Res. Pap. (2018).

[114] N. Divakaran, J. P. Das, A. K. P V, S. Mohanty, A. Ramadoss, and S. K. Nayak, Comprehensive review on various additive manufacturing techniques and its implementation in electronic devices. J. Manuf. Syst. **62**, 477 (2022).

[115] C. Neff, E. Elston, and A. Schrand, Interconnections for additively manufactured hybridized printed electronics in harsh environments. Designs **4**, 1 (2020).

[116] A. Syed-Khaja, D. Schwarz, and J. Franke, Advanced substrate and packaging concepts for compact system integration with additive manufacturing

technologies for high temperature applications. IEEE CPMT Symp. Japan 2015 Packag. Is Everywhere, ICSJ 2015 156 (2015).

[117] T. Islam and A. Sharif, Transient liquid phase bonding. in *Harsh Environment Electronics: Interconnect Materials and Performance Assessment* (2019), pp. 263–292.

[118] O. Olaye and O. A. Ojo, Leapfrog/Dufort-Frankel explicit scheme for diffusion-controlled moving interphase boundary problems with variable diffusion coefficient and solute conservation. Model. Simul. Mater. Sci. Eng. **28**, (2020).

[119] T. C. Illingworth, I. O. Golosnoy, and T. W. Clyne, Modelling of transient liquid phase bonding in binary systems-A new parametric study. Mater. Sci. Eng. A **445**–**446**, 493 (2007).

[120] J. F. Li, P. A. Agyakwa, and C. M. Johnson, A fixed-grid numerical modelling of transient liquid phase bonding and other diffusion-controlled phase changes. J. Mater. Sci. **45**, 2340 (2010).

[121] I. Tuah-Poku, M. Dollar, and T. B. Massalski, A study of the transient liquid phase bonding process applied to a Ag/Cu/Ag sandwich joint. Metall. Trans. A **19**, 675 (1988).

[122] M. Mödlinger and P. Piccardo, Corrosion on prehistoric Cu-Sn-alloys: The influence of artificial environment and storage. Appl. Phys. A Mater. Sci. Process. **113**, 1069 (2013).

[123] C. Paul and R. Sellamuthu, The effect of Sn content on the properties of surface refined Cu-Sn bronze alloys. Procedia Eng. **97**, 1341 (2014).

[124] S. Cheng, C. M. Huang, and M. Pecht, A review of lead-free solders for electronics applications. Microelectron. Reliab. **75**, 77 (2017).

[125] C. Sanabria, A new understanding of the heat treatment of Nb-Sn superconducting wires. A New Understanding of the Heat Treatment of Nb-Sn Superconducting Wires, Florida State University, 2017.

[126] M. K. Pal and V. Bajaj, Nucleation and location of Kirkendall voids at the Tin-based solder/copper joint: a review. Adv. Eng. Mater. (2023).

[127] K. N. Tu and Y. Liu, Recent advances on kinetic analysis of solder joint reactions in 3D IC packaging technology. Mater. Sci. Eng. R Reports **136**, 1 (2019).

[128] Y. Yuan, Y. Guan, D. Li, and N. Moelans, Investigation of diffusion behavior in Cu-Sn solid state diffusion couples. J. Alloys Compd. **661**, 282 (2016).

[129] N. R. Abdul Razak, X. F. Tan, F. Somidin, H. Yasuda, S. D. McDonald, and K. Nogita, In-situ observation of high-temperature Pb-free electric interconnections by synchrotron microradiography. Mater. Lett. **291**, 129520 (2021).

[130] H. Greve and F. P. McCluskey, Thermal conductivity of Cu-Sn transient liquid phase sintered interconnects for high power density modules. 2017 IEEE Int. Work. Integr. Power Packag. IWIPP 2017 (2017).

[131] C. P. Muzzillo and T. Anderson, Thermodynamic assessment of Ag–Cu–In. J. Mater. Sci. **53**, 6893 (2018).

[132] B. Predel, Ag-In (Silver-Indium) Phase diagram Crystal structure. in *Landolt-Börnstein* (1991), pp. 1–6.

[133] T. Dobrovolska, G. Beck, I. Krastev, and A. Zielonka, Phase composition of electrodeposited silver-indium alloys. J. Solid State Electrochem. **12**, 1461 (2008).

[134] Z. Moser, W. Gasior, J. Pstrus, W. Zakulski, and I. Ohnuma, Studies of the Ag-In Phase Diagram and Surface Tension Measurements. J. Electron. Mater. **30**, 1120 (2001).

[135] Y. Y. Wu, W. P. Lin, and C. C. Lee, A study of chemical reactions of silver and indium at 180 °c. J. Mater. Sci. Mater. Electron. **23**, 2235 (2012).

[136] H. Okamoto, Ag-In (silver-indium). J. Phase Equilibria Diffus. **27**, 536 (2006).

[137] Y. M. Liu and T. H. Chuang, Interfacial Reactions between Liquid Indium and Silver Substrates. J. Electron. Mater. **29**, 405 (2000).

[138] P. J. Rossi, N. Zotov, and E. J. Mittemeijer, Kinetics of intermetallic compound formation in thermally evaporated Ag-In bilayers. J. Appl. Phys. **120**, 0 (2016).

[139] C. F. Yu, H. C. Cheng, and W. H. Chen, Structural, mechanical, thermodynamic and electronic properties of AgIn2 and Ag3In intermetallic compounds: Ab initio investigation. RSC Adv. **5**, 70609 (2015).

[140] Y. Huo and C. C. Lee, The growth and stress vs. strain characterization of the silver solid solution phase with indium. J. Alloys Compd. **661**, 372 (2016).

[141] C. H. Tsai, W. C. Huang, L. M. Chew, W. Schmitt, J. Li, H. Nishikawa, and C. R. Kao, Low-pressure micro-silver sintering with the addition of indium for high-temperature power chips attachment. J. Mater. Res. Technol. **15**, 4541 (2021).

[142] Y. Huo, S. W. Fu, Y. L. Chen, and C. C. Lee, A reaction study of sulfur vapor with silver and silver–indium solid solution as a tarnishing test method. J. Mater. Sci. Mater. Electron. **27**, 10382 (2016).

[143] C. H. Tsai, W. C. Huang, and C. R. Kao, Development of Ag–In Alloy Pastes by Mechanical Alloying for Die Attachment of High-Power Semiconductor Devices. Materials (Basel). **15**, 1 (2022).

[144] P. J. Rossi, N. Zotov, E. Bischoff, and E. J. Mittemeijer, Dependence of intermetallic compound formation on the sublayer stacking sequence in Ag-Sn bilayer thin films. Acta Mater. **103**, 174 (2016).

[145] R. Mahayri, M. A. Bousnina, S. Mercone, K. L. Tan, J. M. Morelle, F. Schoenstein, and N. Jouini, The Polyol Process and the Synthesis of ζ Intermetallic Compound Ag5Sn0.9. Materials (Basel). **15**, 1 (2022).

[146] H. Sun, Z. Gao, C. Dong, J. Cao, C. Wang, Q. Gu, Y. Wang, and H. Ma, Influence of Sn crystal preferred orientation on the reflective and environmental stability of electroplated Sn/Ag films. Mater. Chem. Phys. **265**,

124522 (2021).

[147] C. Hang, J. He, Z. Zhang, H. Chen, and M. Li, Low Temperature Bonding by Infiltrating Sn3.5Ag Solder into Porous Ag Sheet for High Temperature Die Attachment in Power Device Packaging. Sci. Rep. **8**, 2 (2018).

[148] R. Mahayri, S. Mercone, F. Giovannelli, K. L. Tan, J. M. Morelle, N. Jouini, and F. Schoenstein, Microstructure effects on thermal and electrical conductivities in the intermetallic compound Ag 3 Sn-based materials, sintered by SPS in view of die-attachment applications. Eur. Phys. J. Spec. Top. **231**, 4173 (2022).

[149] B. Rheingans, L. P. H. Jeurgens, and J. Janczak-Rusch, Fast and Reliable Ag–Sn Transient Liquid Phase Bonding by Combining Rapid Heating with Low-Power Ultrasound. Metall. Mater. Trans. A Phys. Metall. Mater. Sci. **53**, 2195 (2022).

[150] C. Ehrhardt, M. Hutter, H. Oppermann, and K. D. Lang, A lead free joining technology for high temperature interconnects using Transient Liquid Phase Soldering (TLPS). Proc. - Electron. Components Technol. Conf. 1321 (2014).

[151] A. Syed-Khaja, A. Klemm, T. Zerna, and J. Franke, Characterization and Optimization of Sn-Cu TLPS Interconnects for High Temperature Power Electronics through In-Situ-X-Ray Investigations. Proc. - Electron. Components Technol. Conf. **2016**-**Augus**, 1228 (2016).

[152] H. Greve, Assessment of Properties of Transient Liquid Phase Sintered (TLPS)

Interconnects by Simulation and Experiments. Assessment of Properties of Transient Liquid Phase Sintered (TLPS) Interconnects by Simulation and Experiments, 2017.

[153] R. N. Lumley and G. B. Schaffer, The effect of additive particle size on the mechanical properties of sintered aluminium-copper alloys. Scr. Mater. **39**, 1089 (1998).

[154] K. H. Jung, K. D. Min, C. J. Lee, and S. B. Jung, Pressureless die attach by transient liquid phase sintering of Cu nanoparticles and Sn-58Bi particles assisted by polyvinylpyrrolidone dispersant. J. Alloys Compd. **781**, 657 (2019).

[155] G. Lu, J. N. Calata, Z. Zhang, and J. G. Bai, A lead-free, low-temperature sintering die-attach technique for high-performance and high-temperature packaging. in *Proceedings of the Sixth IEEE CPMT Conference on High Density Microsystem Design and Packaging and Component Failure Analysis (HDP '04)* (Shangahi, 2004), pp. 42–46.

[156] C. Binet, K. L. Lencoski, D. F. Heaney, and R. M. German, Modeling of distortion after densification during liquid-phase sintering. Metall. Mater. Trans. A Phys. Metall. Mater. Sci. **35 A**, 3833 (2004).

[157] S. A. Moeini, Seyed Ali Moeini Dissertation. Seyed Ali Moeini Dissertation, 2017.

[158] K. N. Subramanian, Lead-Free Electronic Solders. *Lead-Free Electronic Solders* (2007).

[159] S. Wakeel, A. S. M. A. Haseeb, M. A. Afifi, S. Bingol, and K. L. Hoon, Constituents and performance of no-clean flux for electronic solder. Microelectron. Reliab. **123**, 114177 (2021).

[160] G.-M. Choi, J. Ki-Seok, C. Kwang-Seong, J. Joo, H.-G. Yun, C. Lee, and E. Yong-Sung, Thermochemical Mechanism of the Epoxy-Glutamic Acid Reaction with Sn-3.0 Ag-0.5 Cu Solder Powder for Electrical Joining. Polymers (Basel). **13**, (2021).

[161] I. Miccoli, F. Edler, H. Pfnür, and C. Tegenkamp, The 100th anniversary of the four-point probe technique: The role of probe geometries in isotropic and anisotropic systems. J. Phys. Condens. Matter **27**, (2015).

[162] M. Schneider, J. Maurath, S. B. Fischer, M. Weiß, N. Willenbacher, and E. Koos, Suppressing Crack Formation in Particulate Systems by Utilizing Capillary Forces. ACS Appl. Mater. Interfaces **9**, 11095 (2017).

[163] D. Bušek, K. Dušek, D. Růžička, M. Plaček, P. MacH, J. Urbánek, and J. Starý, Flux effect on void quantity and size in soldered joints. Microelectron. Reliab. **60**, 135 (2016).

[164] A. Syed-Khaja and J. Franke, Investigations on advanced soldering mechanisms for transient liquid phase soldering (TLPS) in power electronics. Proc. 5th Electron. Syst. Technol. Conf. ESTC 2014 1 (2014).

[165] H. Schoeller, K. Jongman, P. Seungbae, and C. Junghyun, Thermodynamics and kinetics of oxidation of pure indium solders. Thermodynamics and

Kinetics of Oxidation of Pure Indium Solders, 2007.

[166] A. Di Renzo, G. Picarelli, and F. P. Di Maio, Numerical Investigation of Funicular Liquid Bridge Interactions Between Spherical Particles. Chem. Eng. Technol. **43**, 830 (2020).

[167] E. Koos and N. Willenbacher, Capillary forces in suspension rheology. Science (80-.). **331**, 897 (2011).

[168] J. P. Wang, E. Gallo, B. François, F. Gabrieli, and P. Lambert, Capillary force and rupture of funicular liquid bridges between three spherical bodies. Powder Technol. **305**, 89 (2017).

[169] S. Wang, F. Liu, J. Cui, M. Miao, and C. Pu, Experimental Study on the Rupture Behavior of the Liquid Bridge between Three Rigid Spheres. Langmuir **38**, 13857 (2022).

[170] J. P. Wang, Force transmission modes of non-cohesive and cohesive materials at the critical state. Materials (Basel). **10**, (2017).

[171] C. F. Zhao, N. P. Kruyt, and O. Millet, Capillary bridges between unequal-sized spherical particles: Rupture distances and capillary forces. Powder Technol. **346**, 462 (2019).

[172] H. N. G. Nguyen, O. Millet, and G. Gagneux, Exact calculation of axisymmetric capillary bridge properties between two unequal-sized spherical particles. Math. Mech. Solids **24**, 2767 (2019).

[173] D. Wu, P. Zhou, G. Wang, B. Zhao, T. Howes, and W. Chen, Modeling of

capillary force between particles with unequal contact angle. Powder Technol. **376**, 390 (2020).

[174] J. G. Bai, T. G. Lei, J. N. Calata, and G. Q. Lu, Control of nanosilver sintering attained through organic binder burnout. J. Mater. Res. **22**, 3494 (2007).

[175] M. A. Galler, D. P. Bentz, and J. A. Lewis, Computer Simulations of Binder Removal From 2-D and 3-D Model Particulate Bodies. J. Am. Ceram. Soc. **79**, 1377 (1996).

[176] W. Xu, M. Jia, and Z. Gong, Thermal conductivity and tortuosity of porous composites considering percolation of porous network: From spherical to polyhedral pores. Compos. Sci. Technol. **167**, 134 (2018).

[177] A. Ukshe, A. Glukhov, and Y. Dobrovolsky, Percolation model for conductivity of composites with segregation of small conductive particles on the grain boundaries. J. Mater. Sci. **55**, 6581 (2020).

[178] P. J. Brigandi, Electrically Conductive Multiphase Polymer Blend Carbon-Based Composites. Electrically Conductive Multiphase Polymer Blend Carbon-Based Composites, Lehigh University, 2017.

[179] W. Villanueva, Diffuse-interface simulations of capillary phenomena. Diffuse-Interface Simulations of Capillary Phenomena, Royal Institute of Technology in Stockholm, Sweden, 2007.

[180] Zhigang Zak Fang, Sintering of Advanced Materials - Fundamentals and Processes. *Sintering of Advanced Materials - Fundamentals and Processes*

(Woodhead Publishing, 2010).

[181] Z. Fu and A. Roosen, Shrinkage of tape cast products during binder burnout. J. Am. Ceram. Soc. **98**, 20 (2015).

[182] S.-J. L. Kang, Sintering - Densification, Grain Growth, and Microstructure. *Sintering - Densification, Grain Growth, and Microstructure* (Elsevier, 2005).

[183] M. Hori and S. Nemat-Nasser, On two micromechanics theories for determining micro-macro relations in heterogeneous solids. Mechanics of Materials.

[184] H. A. Moghaddam and P. Mertiny, Stochastic finite element analysis framework for modelling mechanical properties of particulate modified polymer composites. Materials (Basel). **12**, (2019).

[185] S. Nemat-Nasser and M. Hori, Micromechanics: Overall Properties Of Heterogeneous Materials. *Micromechanics: Overall Properties Of Heterogeneous Materials*, Second Rev (Elsevier, Lausanne, 1999).

[186] F. Ye and H. Wang, A simple Python code for computing effective properties of 2D and 3D representative volume element under periodic boundary conditions. (2017).

[187] L. GAO, C. WANG, Z. LIU, and Z. ZHUANG, Theoretical aspects of selecting repeated unit cell model in micromechanical analysis using displacement-based finite element method. Chinese J. Aeronaut. (2017).

[188] W. Tian, L. Qi, C. Su, and J. Zhou, Mean-field homogenization based

approach to evaluate macroscopic coefficients of thermal expansion of composite materials. Int. J. Heat Mass Transf. (2016).

[189] W. Tian, L. Qi, X. Chao, J. Liang, and M. Fu, Periodic boundary condition and its numerical implementation algorithm for the evaluation of effective mechanical properties of the composites with complicated micro-structures. Compos. Part B Eng. (2019).

[190] J. F. Zhang, X. X. Zhang, Q. Z. Wang, B. L. Xiao, and Z. Y. Ma, Simulations of deformation and damage processes of SiCp/Al composites during tension. J. Mater. Sci. Technol. **34**, 627 (2018).

[191] D. W. Kim, J. H. Lim, and J. Yu, Efficient prediction of the electrical conductivity and percolation threshold of nanocomposite containing spherical particles with three-dimensional random representative volume elements by random filler removal. Compos. Part B Eng. **168**, 387 (2019).

[192] K. Lewis and T. Matsuura, Calculation of the Meniscus Shape Formed under Gravitational Force by Solving the Young-Laplace Differential Equation Using the Bézier Curve Method. ACS Omega **7**, 36510 (2022).

[193] R. Vargas-Bernal, G. Herrera-Pérez, M. E. Calixto-Olalde, and M. Tecpoyotl-Torres, Analysis of DC electrical conductivity models of carbon nanotube-polymer composites with potential application to nanometric electronic devices. J. Electr. Comput. Eng. **2013**, (2013).

[194] D. S. McLachlan, M. Blaszkiewicz, and R. E. Newnham, Electrical Resistivity

of Composites. J. Am. Ceram. Soc. **73**, 2187 (1990).